Investigation of the Dipole Response of Nickel Isotopes in the Presence of a High-Frequency Electromagnetic Field

Dissertation
zur Erlangung des Grades
"Doktor der Naturwissenschaften"
im Promotionsfach Chemie

am Fachbereich Chemie, Pharmazie und Geowissenschaften
der Johannes Gutenberg-Universität Mainz

Dominic M. Rossi

geboren in Stanford, CA, USA

Mainz, 2009

Dekan:

1. Berichterstatter:
2. Berichterstatter:

Tag der mündlichen Prüfung: 25.01.2010

D77

Labor omnia vicit improbus

Virgil, Georgica I (v. 145-146)

Abstract

The electric dipole response of neutron-rich nickel isotopes has been investigated using the LAND setup at GSI in Darmstadt (Germany). Relativistic secondary beams of $^{56-57}$Ni and $^{67-72}$Ni at approximately 500 AMeV have been generated using projectile fragmentation of stable ions on a 4 g/cm^2 Be target and subsequent separation in the magnetic dipole fields of the FRagment Separator (FRS). After reaching the LAND setup in Cave C, the radioactive ions were excited electromagnetically in the electric field of a Pb target. The decay products have been measured in inverse kinematics using various detectors. Neutron-rich $^{67-69}$Ni isotopes decay by the emission of neutrons, which are detected in the LAND detector. The present analysis concentrates on the (γ,n) and (γ,2n) channels in these nuclei, since the proton and three-neutron thresholds are unlikely to be reached considering the virtual photon spectrum for nickel ions at 500 AMeV. A measurement of the stable ^{58}Ni isotope is used as a benchmark to check the accuracy of the present results with previously published data. The measured (γ,n) and (γ,np) channels are compared with an inclusive photoneutron measurement by Fultz and coworkers, which are consistent within the respective errors.

The measured excitation energy distributions of $^{67-69}$Ni contain a large portion of the Giant Dipole Resonance (GDR) strength predicted by the Thomas-Reiche-Kuhn energy-weighted sum rule, as well as a significant amount of low-lying E1 strength, that cannot be attributed to the GDR alone. The GDR distribution parameters are calculated using well-established semi-empirical systematic models, providing the peak energies and widths. The GDR strength is extracted from the χ^2 minimization of the model GDR to the measured data of the (γ,2n) channel, thereby excluding any influence of eventual low-lying strength. The subtraction of the obtained GDR distribution from the total measured E1 strength provides the low-lying E1 strength distribution, which is attributed to the Pygmy Dipole Resonance (PDR). The extraction of the peak energy, width and strength is performed using a Gaussian function. The minimization of trial Gaussian distributions to the data does not converge towards a sharp minimum. Therefore, the results are presented by a χ^2 distribution as a function of all three Gaussian parameters. Various predictions of PDR distributions exist, as well as a recent measurement of the ^{68}Ni pygmy dipole-resonance obtained by virtual photon scattering, to which the present pygmy dipole-resonance distribution is also compared.

Zusammenfassung

Die elektrische Dipolstärkeverteilung neutronenreicher Nickelisotope wurde am LAND-Experimentaufbau bei der GSI in Darmstadt untersucht. Relativistische Sekundärstrahlen, die $^{56-57}$Ni und $^{67-72}$Ni enthielten, wurden mit ungefähr 500 AMeV mittels Projektilfragmentierung an einem 4 g/cm^2 Be-Target erzeugt. Die dabei entstandenen Fragmente wurden anschliessend im Dipolmagnetfeld des Fragmentseparators (FRS) aufgetrennt und nach Cave C gelenkt, wo sie im elektrischen Feld eines massiven Bleitargets elektromagnetisch angeregt wurden. Die Zerfallsprodukte wurden mit verschiedenen Detektoren in inverser Kinematik nachgewiesen. Die neutronenreichen $^{67-69}$Ni-Isotope zerfallen mittels Neutronenemission, die im LAND-Detektor gemessen werden. Die vorliegende Datenanalyse befasst sich mit den (γ,n)- und (γ,2n)-Kanälen, da unter Beachtung des virtuellen Photonenspektrums für Nickelionen bei 500 AMeV die Proton- und 3n-Schwellen kaum erreicht werden können. Die Messung am stabilen ^{58}Ni dient durch die Vergleichsmöglichkeit mit einer früheren Messung als Bezugspunkt für sämtliche gemessenen Werte dieses Experiments. Die gemessenen (γ,n)- und (γ,np)-Kanäle werden dabei mit der inklusiven Photoneutronenverteilung von Fultz *et al.* verglichen, die mit den gegenwärtigen Ergebnissen im Rahmen der entsprechenden Fehler übereinstimmen.

In den gemessenen Anregungsfunktionen von $^{67-69}$Ni wurde sowohl ein grosser Anteil der Stärke der Dipol-Riesenresonanz (GDR), die durch die Thomas-Reiche-Kuhn Summenregel vorhergesagt wird, als auch eine signifikante niedrig-liegende E1-Stärke beobachtet, die nicht allein der GDR zugeordnet werden kann. Die Lage und Breite der GDR wird mittels semi-empirischer systematischer Modelle berechnet, während die Stärke durch χ^2-Minimierung der Modellverteilung an den gemessenen (γ,2n)-Daten erhalten wird, da der Einfluss durch niedrig-liegender Stärke in diesem Bereich ausgeschlossen werden kann. Die Verteilung niedrig-liegender E1 Stärke nach Abzug der GDR von der gemessenen Stärkeverteilung wird durch eine Gaussverteilung beschrieben und der Pygmy-Dipolresonanz (PDR) zugeordnet. Die Minimierung der Gauss-Modellfunktion an die PDR-Verteilung liefert kein scharfes Minimum im Parameterraum. Deshalb werden die Ergebnisse als χ^2-Verteilung als Funktion aller drei Gaussparameter dargestellt, die sich in der Umgebung der möglichen Parameter-Minima befinden. Eine alternative Messung der PDR mittels Streuung virtueller Photonen in ^{68}Ni wurde vor kurzer Zeit veröffentlicht. Die hier gemessene PDR Stärkeverteilung wird sowohl mit diesen Daten als auch mit theoretischen Vorhersagen verglichen.

Contents

List of Figures

List of Tables

Chapter 1

Introduction

The interaction of electromagnetic radiation with matter can be considered as one of the most fundamental processes of nature. It is one of the main mechanisms required to sustain life on earth, due to the conversion of luminous energy into a chemically stored energy form *via* photosynthesis. It defines the way we perceive our world, due to the stimulation of photoreceptor cells by photons in the retina. When used as a tool, it provides insight into the structure and functionality of macromolecules such as proteins, using, *e.g.*, x-ray diffraction or nuclear magnetic resonance techniques, as well as into the electronic structure and dynamics of molecules and atoms with, *e.g.*, absorption methods in the infrared, visible, and ultraviolet domains of the electromagnetic spectrum. The dynamical properties of atomic nuclei can be studied in a similar way, with the main experimental difference being the energy range of the electromagnetic probes. The energy of the photons must be adjusted to the forces under investigation, since the energy transferred by the interaction must be considered as a perturbation with respect to the total energy involved. Therefore, visible and ultraviolet photons are used to excite valence electrons in the atomic shell, where they are bound by energies in the eV range. In the case of the nucleus, where strong and electromagnetic forces dominate, photon energies in the keV and MeV range are required.

When a photon interacts with an atomic nucleus, several scenarios are possible, depending on the conveyed energy. For relatively low energies, single nucleons can be promoted to excited states, which decay back to the ground state *via* a gamma cascade, revealing a portion of the nuclear shell structure, or, in the case of deformed nuclei, rotational modes can be excited. At higher energies, a larger number of nucleons can participate in the excitation, enabling vibrational and compressional modes. Giant resonances are a class of such vibrations, in which a large fraction of the nucleons is involved [1]. These are collective modes in which the nucleons oscillate in phase, in so-called isoscalar modes, or in which the protons and neutrons are out of phase, in the isovector modes. More complex modes exist also, where, *e.g.*, nucleons of opposite spin

oscillate against each other, or combinations of several basic modes. In the present work, the attention was focused on the electric dipole mode, due to the excitation mechanism used in the experiment.

The isovector giant dipole resonance has been studied intensively in the past, however, mainly in stable nuclei [2]. While systematical trends have been established using this data, it is not clear if they are valid for exotic nuclei as well. Theoretical calculations show the fragmentation of the electric dipole strength in neutron-proton asymmetric nuclei [3]. A previous LAND* experiment on neutron-rich oxygen isotopes showed this fragmentation of dipole strength, which, based on theoretical grounds, originates from single neutron particle-hole excitations [4]. In heavier nuclei, the degree of collectivity increases to form a so-called soft dipole mode or pygmy dipole resonance, first predicted by Lane [5]. A systematic investigation of neutron-rich tin isotopes using the LAND setup provided evidence for the existence of this low-lying strength [6, 7]. Recent results from an experiment performed by the RISING† collaboration at GSI‡ on neutron-rich nickel isotopes [8] shows the presence of low-lying dipole strength in ^{68}Ni, which is also supported by various RPA calculations [9–11]. One of the objectives of the experiment described in this thesis is the extraction of the electric dipole strength in a series of neutron-rich nickel isotopes, with an emphasis on the pygmy dipole resonance.

This work concentrates on the results of an experiment performed in 2005 with the LAND setup at GSI. The electric dipole response of various nickel nuclei was measured using relativistic radioactive beams at approximately 500 AMeV. Primary heavy-ion beams of ^{58}Ni and ^{86}Kr have been accelerated in the UNILAC§ and in the SIS¶ 18 synchrotron before being directed onto a thick Be target, where a large amount of lighter fragments is produced. These are thereafter separated in the magnetic dipole field of the FRS‖, extracting only a selected mass-over-charge ratio. The ions are excited in the electric field of Pb target nuclei through a process described by the Weizsäcker-Williams approach. The neutron-rich nuclei then decay mainly by emission of neutrons, which are detected in LAND. The excitation energy is reconstructed on an event-by-event basis using the measured invariant mass of all participating species. The power of the LAND setup lies in the detection of all components involved in the reaction, providing exclusive measurements. Only the excitation-energy distribution above the particle emission threshold can be measured in LAND experiments. Information below the particle threshold must be gained through complementary methods, such as virtual

*Large Area Neutron Detector

†Rare Isotope Spectroscopic INvestigations at GSI.

‡Gesellschaft für Schwerionenforschung in Darmstadt, Germany. The new official name is GSI Helmholtzzentrum für Schwerionenforschung GmbH.

§UNIversal Linear ACcelerator

¶SchwerIonenSynchrotron

‖FRagment Separator

photon scattering, performed, *e.g.*, at NSCL** for the neutron-rich oxygen isotopes [12], or by the RISING collaboration in the case of ^{68}Ni.

* * *

This thesis is divided into six main chapters. Chapter two describes the basic theoretical principles commonly used in the study of giant resonances, as well as the Weizsäcker-Williams approach of equivalent photons. Several examples of dipole strength measured previously in various nuclei are also depicted. Chapter three introduces the experimental setup used to obtain the present data. The fourth chapter evokes briefly several calibration issues which enable the access to the physically relevant data using analysis tools described in chapter five. Chapter six exposes the obtained results for two mass regions in the nickel isotopic chain, namely ^{58}Ni and $^{67-69}$Ni. After the discussion of these results, chapter seven will state the main conclusions of the analyzed experiment.

**National Superconducting Cyclotron Laboratory, located at Michigan State University in East Lansing.

Chapter 2

Theoretical Principles and Phenomenological Issues

Coulomb excitation of atomic nuclei can be achieved by their exposure to an electromagnetic field varying in time. If the excitation function shall be measured, as is one of the goals of the present experiment, it is essential to precisely know the energy transmitted to the nucleus on an event-by-event basis. When performing photoabsorption measurements with real photons, their energy may be measured directly (*e.g.*, when using tagged photons) and thus provides the excitation energy of the nucleus. In heavy-ion-induced electromagnetic excitation, such a measurement is impossible when using an external target. If the photon interaction is considered as an interaction with an electromagnetic field varying with time, a Fourier analysis of this field will provide exactly the photon energy. The energy transmitted by any electromagnetic field to the nucleus may be analyzed in a similar manner. If the field varies with time, the Fourier transform will provide the excitation energy spectrum conveyed by the field, which is a continuous distribution. The invariant mass must therefore be reconstructed separately for each event, based on the momenta of all species participating in the excitation reaction, which eventually leads to the excitation energy.

The evaluation of the excitation of atomic nuclei relies on several concepts that will be presented in the first part of this chapter. The first question that will be addressed is how nuclei respond to electromagnetic excitation, which will then be followed by the description of giant resonances, as well as various features appearing in exotic nuclei. Finally the question of how electromagnetic excitation occurs when mediated by the interaction between heavy ions will be treated. The idea will first be presented in the classical case, before being adapted to the relativistically correct form required by the reaction investigated in the experiment.

2.1 Response of Nuclei to Electromagnetic Excitation

When a microscopic system is exposed to a time-varying electromagnetic field, its behavior may be described by a transition operator depending on the type of the electromagnetic field. While real fields can be quite complex, one can express them as a linear combination of multipole fields. Such electromagnetic fields are characterized by angular momentum λ and magnetic μ quantum numbers, and are divided into electric $E\lambda$ and magnetic $M\lambda$ components, according to the associated parity of $(-1)^{\lambda}$ and $(-1)^{\lambda+1}$, respectively. Since the magnetic moments are usually two orders of magnitude smaller than their electric counterparts, only the electric multipole moments will be discussed from here on. In the long-wavelength limit, the electric multipole moment $\mathcal{M}(E\lambda,\mu)$ is given by Harakeh and van der Woude [1]:

$$\mathcal{M}(E\lambda,\mu) = \int \rho(\vec{r})\, r^{\lambda} Y_{\lambda\mu}(\Omega)\, d^3r \tag{2.1}$$

where $\rho(\vec{r})$ is the charge density, $\vec{r}$ is the position vector, r its length, λ is the angular momentum quantum number, $Y_{\lambda\mu}$ is the spherical harmonic associated to the quantum numbers $(\lambda\mu)$, and Ω is the solid angle. The long-wavelength limit is reached when $kr \ll 1$, where k is the wave vector associated with the energy transfer of the interaction. If the protons and neutrons are considered as point-like entities, the charge density can be expressed as the following sum over A nucleons:

$$\rho(\vec{r}) = \sum_{k=1}^{A} e\left(\frac{1}{2} - t_{zk}\right)\delta(\vec{r} - \vec{r_k}) \tag{2.2}$$

where e is the unit charge and $t_z = +\frac{1}{2}$ and $t_z = -\frac{1}{2}$ are the isospin values for neutrons and protons, respectively. When combining expressions (2.1) and (2.2), the electric multipole transition operator is obtained:

$$\mathcal{M}(E\lambda,\mu) = \frac{1}{2}e\sum_{k=1}^{A} r_k^{\lambda} Y_{\lambda\mu}(\Omega_k) - e\sum_{k=1}^{A} t_{zk} r_k^{\lambda} Y_{\lambda\mu}(\Omega_k) \tag{2.3}$$

The transition operator is split into two terms, leading to two types of electric excitations for a given λ. The first term on the right-hand side of equation (2.3) does not depend on isospin and leads to isoscalar ($\Delta T = 0$) excitations. The second term depends on isospin, and therefore leads to isovector ($\Delta T = 1$) excitations.

Up to now, only information on the transition itself has been obtained. The entire process of electromagnetic excitation also depends on the initial and final states of the system. The so-called reduced transition rates $B(E\lambda, J_i \to J_f)$ express the transition strength based on the states J_iM_i and J_fM_f of the system and on the transition operator $\mathcal{M}(E\lambda,\mu)$ [13]:

$$B(E\lambda, J_i \to J_f) = \sum_{\mu M_f} \left|\langle J_f M_f \left|\mathcal{M}(E\lambda,\mu)\right| J_i M_i\rangle\right|^2 \tag{2.4}$$

where the sum runs over the magnetic quantum numbers μ of the transition operator and over the polarization M_f of the final state. Using the Wigner-Eckart theorem, stating that the dependence of the matrix element on the magnetic quantum numbers is given by the Clebsch-Gordan coefficients [13, 14], expression (2.4) reduces to:

$$B\left(E\lambda, J_i \rightarrow J_f\right) = \frac{1}{2J_i + 1} \left|\left\langle J_f \left\| \mathcal{M}\left(E\lambda\right) \right\| J_i \right\rangle\right|^2 \tag{2.5}$$

The reduced transition matrix element $M(E\lambda)$ can be extracted from the previous expression and is defined as follows:

$$M\left(E\lambda, J_i \rightarrow J_f\right) = \left\langle J_f \left\| \mathcal{M}\left(E\lambda\right) \right\| J_i \right\rangle \tag{2.6}$$

The strength of the response of a given system can now be evaluated with equation (2.5), which can also be measured directly. However, if knowledge of the degree of collectivity of the excitation is requested, the use of sum rules is necessary, which will be described in the following section.

The reduced electromagnetic transition rate $B(E\lambda)$ and the degree of deformation of the nucleus can be linked together with the concept of so-called deformation lengths. Considering a spherical projectile-target pair, the radii R_i can be described by the following equation [15]:

$$R_i\left(\vartheta_i, \varphi_i\right) = R_{0i}\left(1 + \sum_{\lambda\mu} \beta_{\lambda\mu} Y_{\lambda\mu}\left(\vartheta_i, \varphi_i\right)\right) \tag{2.7}$$

where $i = 1, 2$ labels the projectile and target, respectively. The angles ϑ_i and φ_i are defined in a body-fixed coordinate system. The radius R_{0i} is defined for the ground state and is modified due to the excitation to a given vibrational mode of the nucleus, which can be described by a set of basic spherically harmonic vibrations. Each basic mode is defined by the amplitude $\beta_{\lambda\mu}$ and by the normalized spherical harmonic function $Y_{\lambda\mu}\left(\vartheta_i, \varphi_i\right)$. In the following discussion, only one harmonic mode will be considered, such that the $\lambda\mu$ label will be dropped. Also, only the target will be considered, thus defining $i = 2$. Using a similar formalism as in the analysis of elastic scattering, a first-order optical-model potential U_β will be defined for the deformed vibrational state:

$$U_\beta\left(r, \vartheta_2, \varphi_2\right) = U_0\left(r - R_U\right) - R_{U2}\beta_{U2}\frac{dU_0\left(r - R_U\right)}{dr} Y\left(\vartheta_2, \varphi_2\right) \tag{2.8}$$

where r is the distance between the centers of the target and of the projectile, R_U is the sum of the potential-radii of the target and of the projectile, and R_{U2} is the potential radius of the target. This allows the vibration to be treated as a perturbation. The first term of the right-hand side of equation (2.8) is responsible for elastic scattering, while the second term is responsible for inelastic scattering. It should be noted that the second term of the right-hand side (without the spherical harmonic function) is the

deformation energy. The nuclear potential U_0 is complex for heavy-ion scattering, and can be defined as:

$$U_0\left(r - R_U\right) \longrightarrow -V f\left(r - R_V\right) - iW g\left(r - R_W\right) \tag{2.9}$$

where the radius parameters R_V and R_W are the radii attributed to the two potential components V and W. The functions $f\left(r - R_V\right)$ and $g\left(r - R_W\right)$ define the behavior of the potential with respect to the distance between the surfaces of the target and of the projectile. The Coulomb potential term V_C must be added to expression (2.9) for the complete description of the scattering process. Taking the complex potential of expression (2.9) into account, the optical potential in equation (2.8) can be re-written as:

$$U_\beta - U_0 = \left(\beta_{C2}\frac{\partial V_C}{\partial \beta_{C2}} + \left(R_{V2}\beta_{V2}\right) V \frac{df}{dr} + i\left(R_{W2}\beta_{W2}\right) W \frac{dg}{dr}\right) Y\left(\vartheta_2, \varphi_2\right) \tag{2.10}$$

where the partial derivative of the Coulomb potential with respect to the nuclear deformation is given by:

$$\frac{\partial V_C}{\partial \beta_{C2}} = \frac{3R_{C2}^{\lambda}}{2\lambda + 1}\frac{Z_1 Z_2 e^2}{r^{\lambda+1}} \tag{2.11}$$

with $r \geq R_{C1} + R_{C2}$, the multipole order λ of the excitation, the charge numbers of the projectile Z_1 and target Z_2, and the unit charge e. The obtained optical potential can be used in various theoretical models describing inelastic scattering of heavy ions, such as the distorted wave Born approximation (DWBA) or various coupled channels (CC) methods. Using the DWBA method, the differential cross section can be calculated, involving the use of reduced electromagnetic transition rates for the Coulomb term. A comparison with equation (2.10) provides a link between the value of $B(E\lambda)$ and the mean deformation length $\left\langle R_{C2}^{\lambda}\beta_{C2}\right\rangle$:

$$\sqrt{B\left(E\lambda\right)} = \frac{3}{4\pi} Z_2 e \left\langle R_{C2}^{\lambda}\beta_{C2}\right\rangle \tag{2.12}$$

Another important feature of the optical potential of expression (2.10) is the possible interference between the first (Coulomb) and second (nuclear) terms of the right-hand side of this equation. This introduces the concept of Coulomb-nuclear interference when the cross section is calculated using, for instance, a coupled channels calculation. The integral cross sections of Coulomb dissociation reactions can then be expressed by the following equation [16]:

$$\sigma_{CN} = \sigma_C + \sigma_N + \sigma_I \tag{2.13}$$

with the combined Coulomb and nuclear cross section σ_{CN}, the pure Coulomb cross section σ_C, the pure nuclear cross section σ_N, and the interference term σ_I, which can be positive or negative for constructive and destructive interference, respectively. Only calculations can predict the sign and amplitude of the interference term.

2.2 Sum Rules

The theoretical formulation of the transition operator has been described in section 2.1. However, the obtained expressions cannot be used directly to describe cross sections measured experimentally. The oscillator sum rules provide the link between theory and experiment. They depend on the potential energy term of the Hamiltonian H, and neglect velocity- and charge-dependent effects of the nucleon-nucleon force. The oscillator strength is defined as the transition probability multiplied by the transition energy $E_a - E_0$, where E_a is the energy of state a and E_0 is the ground state energy [17]. Based on this definition, the sum of oscillator strengths is given by:

$$S(\mathcal{M}) \equiv \sum_a (E_a - E_0) \left|\langle a \left|\mathcal{M}\right| 0\rangle\right|^2 = \frac{1}{2} \left\langle 0 \left|[\mathcal{M}, [H, \mathcal{M}]]\right| 0\right\rangle \tag{2.14}$$

where the sum runs over all states a accessible with the operator $\mathcal{M}$ from the ground state. Equation (2.14) is also known as the energy-weighted sum rule. Considering equation (2.4), an alternate expression for expression (2.14) using the reduced transition probability can be obtained. When in presence of a multipole field, *e.g.*, as given by expression (2.1), equation (2.14) can be written as:

$$S(E\lambda) = \frac{2\lambda+1}{4\pi} \frac{\hbar^2}{2M} A \left\langle \left(\frac{df(r)}{dr}\right)^2 + \lambda(\lambda+1) \left(\frac{f(r)}{r}\right)^2 \right\rangle \tag{2.15}$$

with M the mass of the nucleus, A the number of particles of the system and $f(r)$ the radial part of the multipole field of angular quantum number λ. For the case of an E1 transition, the transition operator is given by equation (2.3): the radial component is $f(r) = \rho(\vec{r})\, r$. According to definition (2.2), the electromagnetic interaction only affects the protons of the nucleus, which introduces center-of-mass effects in equation (2.1). An effective charge of $\frac{N}{A} \cdot e$ and $-\frac{Z}{A} \cdot e$ is therefore attributed to the Z protons and N neutrons of the nucleus of mass number A, respectively. When combining the parameter A of equation (2.15) with the e^2 term of the radial term, the effective-charge term of the nucleus is:

$$Ae_{eff}^2 = \left(Z\left(\frac{N}{A}\right)^2 + N\left(\frac{Z}{A}\right)^2\right) e^2 = \frac{NZ}{A}\, e^2 \tag{2.16}$$

Expression (2.15) then reduces to:

$$S(E1) = \frac{9}{4\pi} \frac{\hbar^2}{2M} \frac{NZ}{A}\, e^2 = 14.8\, \frac{NZ}{A}\, e^2 \text{ MeV fm}^2 \tag{2.17}$$

which can finally be used to calculate the integral photoabsorption cross section:

$$\int_0^\infty \sigma dE = \frac{16\pi^3}{9\hbar c} S(E1) \text{ MeV fm}^2 \tag{2.18}$$

Equation (2.18) is also known as the Thomas-Reiche-Kuhn (TRK) sum rule (or energy-weighted sum rule for the isovector E1 resonance). Combining equations (2.17) and

(2.18) leads to a different expression for the TRK sum rule for A particles with charge e_{eff} [1, 2]:

$$\int_0^\infty \sigma(E)\, dE = \frac{2\pi^2 \hbar A e_{eff}^2}{mc} \cong 60 \frac{NZ}{A} \text{ MeV mb} \tag{2.19}$$

2.3 Giant Resonances

2.3.1 General Properties

Giant resonances are collective modes in atomic nuclei with relatively large cross sections, involving usually a large fraction of the nucleons. They occur as damped harmonic oscillations of the density or shape of the nucleus. The first experimental observation of a giant resonance took place in 1937 by Bothe and Gentner [18], although the exact nature of the resonance was not understood. The phenomenon was described in 1944 as being an oscillation of the protons against the neutrons in the nucleus, *i.e.*, the isovector giant dipole resonance [19]. Later, other resonance modes have been observed, contributing to a systematic view of the giant resonances. The current classification relies on the multipolarity L of the resonance, on the isospin T and on the spin S quantum numbers. The multipolarity defines the number of nodal planes of the resonance, and therefore sets the shape of the oscillation, *e.g.*, $\Delta L = 0$ leads to monopole, $\Delta L = 1$ to dipole and $\Delta L = 2$ to quadrupole modes. From a macroscopic and hydrodynamic point of view, a giant resonance can be considered as a damped oscillation of the nucleons. The nucleons can either oscillate in-phase or out-of-phase, according to the spin and isospin quantum numbers. A $\{\Delta L = 1,\ \Delta T = 1,\ \Delta S = 0\}$ resonance, called the isovector giant dipole resonance, is represented by a proton fluid oscillating against a neutron fluid, whereas a $\{\Delta L = 1,\ \Delta T = 0,\ \Delta S = 1\}$ resonance can be visualized by a fluid of protons and neutrons with spin $\uparrow$ oscillating against a similar fluid with spin $\downarrow$. The change of spin quantum number therefore defines the electric ($\Delta S = 0$) or magnetic ($\Delta S = 1$) nature of the resonance.

Figure 2.1 shows various giant resonance modes based on the multipolarity, isospin, and spin quantum numbers. The isoscalar giant dipole resonance (ISGDR) is missing in the previous figure, since in a first-level approximation, the in-phase movement of all nucleons implies also that the center-of-mass follows this movement, which is then observed as a simple displacement of the entire nucleus. However, higher-order terms in the ISGDR transition operator predict a 'squeezing' mode, being an oscillation of the nucleon density, where the center-of-mass remains immobile. Generally speaking, the study of giant resonances provides access to various properties of the nucleus, which leads to properties of pure nuclear matter through extrapolation.

Giant resonances can be considered as damped harmonic oscillations. If such a system is coupled to an external field, *e.g.*, an electromagnetic field, the resonance is described by

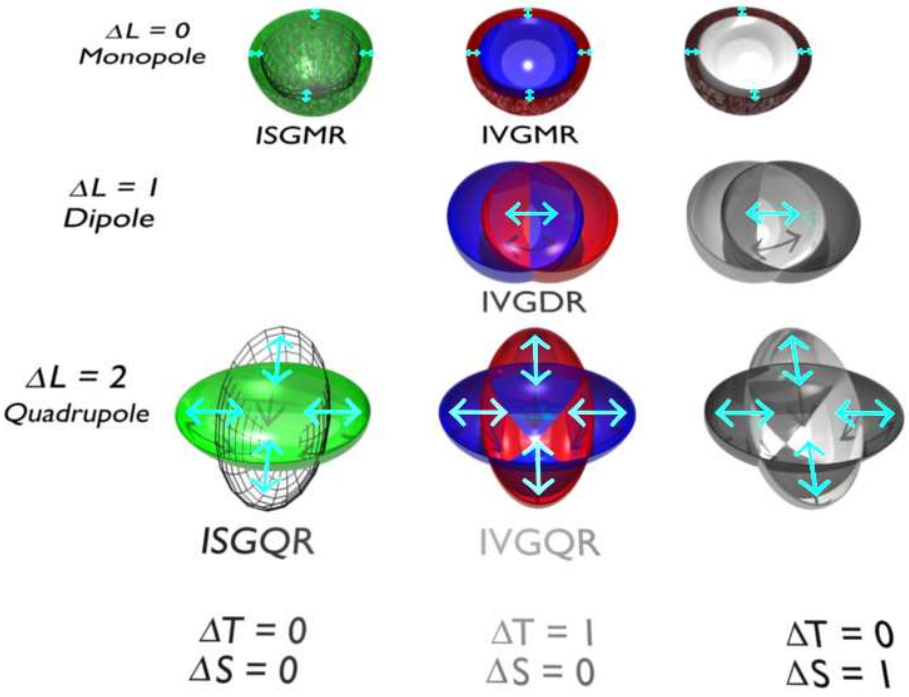

Figure 2.1: Overview of the main giant resonance modes. The following color code has been used: all nucleons (green), protons (red), neutrons (blue), nucleons with spin ↑ (light gray), nucleons with spin ↓ (dark gray).

a Lorentzian function [20]. Mathematically speaking, Lorentzian functions are symmetric and extend from $-\infty$ to $+\infty$, meaning that the value of such a function is always non-zero at the origin. This is not realistic from a physical point of view, since the excitation to a giant resonance will not take place without an energy transfer to the system. Giant resonances are therefore better described by Breit-Wigner distributions [2]:

$$\sigma_\gamma(E) = \frac{\sigma_m}{1 + \left(\frac{E^2 - E_m^2}{E\Gamma}\right)^2} \tag{2.20}$$

where E_m is the resonance energy of the peak of the distribution, Γ the width and σ_m the cross section at E_m. These three quantities have been measured systematically over a wide range of stable nuclei and present a systematic trend, which can be used to evaluate the resonances of nuclei for which experimental data is not available. As can

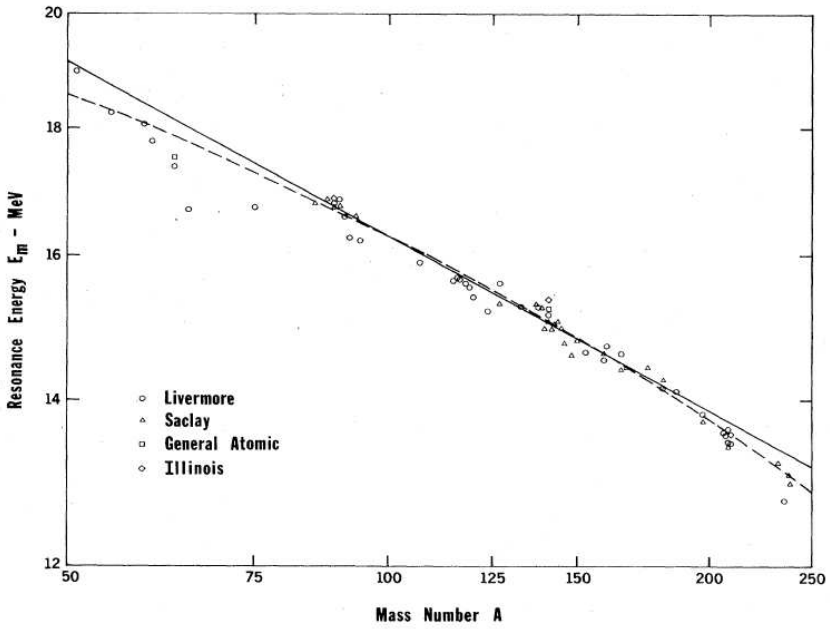

Figure 2.2: Evolution of E_m of GDR as a function of mass number A. See text for explanation of solid and dashed lines. Figure from Berman and Fultz [21].

be seen in figure 2.2, the GDR peak energy E_m varies rather smoothly as a function of the mass number A. This feature is expressed by several semi-empirical expressions for E_m, allowing the calculation of the peak energy for any nucleus of mass number A in the validity range of the model. The solid line represented in figure 2.2 is a fit function for the peak energies E_m:

$$E_m = c_1 A^{-1/c_2} \tag{2.21}$$

where A is the mass number. The fit parameters take the values $c_1 = 47.9$ MeV and $c_2 = 4.27$. The fit function represented by the dashed line in the same figure is expressed

by:

$$E_m = c_5 A^{-1/3}\left(1 - e^{-A/A_0}\right) + c_6 A^{-1/6} e^{-A/A_0} \tag{2.22}$$

with the fit parameters $c_5 = 77.9$ MeV, $c_6 = 34.5$ MeV and $A_0 = 238$.

The following function for the GDR peak energy is based on the Jensen-Steinwedel and Goldhaber-Teller models, based on a hydrodynamical view of the giant resonance [1, 21]:

$$E_m = 31.2A^{-1/3} + 20.6A^{-1/6} \text{ MeV} \tag{2.23}$$

The function described above does not take into account the proton-neutron asymmetry nor the eventual deformation of the nucleus, which requires a more sophisticated systematical model.

The resonance width can also be described by a semi-empirical function based on the hydrodynamical modeling of the nucleus. Auerbach and Yeverechyahu considered two compressible and viscous nuclear fluids, and propose the following resonance width based on the viscosity terms [22]:

$$\Gamma = 2.3 + 14A^{-2/3} + 21A^{-1/2} \text{ MeV} \tag{2.24}$$

While the GDR width is parameterized according to the mass number in the previous expression, it can also be calculated as a function of the peak energy [1]:

$$\Gamma\left(E_m\right) = (0.026 \pm 0.005) \cdot E_m^{1.9\pm0.1} \text{ MeV} \tag{2.25}$$

Junghans *et al.* propose a different parametrization of the GDR peak energy and width for nuclei with $A > 80$, based on the Finite Range Droplet Model (FRDM) [23–27]. Since the deformation of the nucleus is taken into account, the GDR may split into up to three components for triaxial nuclei. The peak energies are calculated in two steps. First the so-called centroid energy is calculated, which does not contain any deformation parameters:

$$\begin{aligned} E_0 &= \frac{\hbar c}{R_0}\sqrt{\frac{8J}{m^*}\cdot\frac{A^2}{4NZ}}\left(1 + u - \epsilon\cdot\frac{1+\epsilon+3u}{1+\epsilon+u}\right)^{-1/2}, \\ u &= (1-\epsilon)\,A^{-1/3}\cdot\frac{3J}{Q} \end{aligned} \tag{2.26}$$

with $R_0 = 1.16A^{1/3}$ fm, the symmetry energy constant $J = 32.7$ MeV, the surface stiffness constant $Q = 29.2$ MeV and $\epsilon = 0.0768$. The effective nucleon mass $m^* = 874$ MeV$/c^2$ has been obtained by optimizing the calculated values to measured data of heavy nuclei. Then, the three peak energies are calculated according to the degree of deformation. The peak energy being inversely proportional to the semi-axis length R_k, the energy values are given by:

$$E_k = E_0\frac{R_0}{R_k} = \frac{E_0}{\exp\left[\sqrt{\frac{5}{4\pi}}\cdot\beta\cos\left(\gamma - \frac{2}{3}k\pi\right)\right]} \tag{2.27}$$

where β and γ are the Hill-Wheeler parameters for ellipsoidal shapes [17,28]. The index k of equation (2.27) can run up to $k = 3$ for triaxial nuclei. An individual resonance width is also attributed to each peak energy:

$$\Gamma_k\left(E_k\right) = \Gamma_0\left(E_0\right) \cdot \left(\frac{E_k}{E_0}\right)^{\delta} = 1.99 \text{ MeV} \cdot \left(\frac{E_k}{10 \text{ MeV}}\right)^{\delta} \tag{2.28}$$

with $\delta = 1.6$.

The third parameter describing a giant resonance is its integral, or strength. The numerical values are given by the appropriate energy-weighted sum rules, which depend on the transition operator. Each type of giant resonance has therefore a different sum rule attributed to it. For the isovector GDR, the corresponding sum rule is the Thomas-Reiche-Kuhn (TRK) sum rule, given by equation (2.19). The GDR distribution can be described completely with the parametrization provided by Junghans *et al.* [24] by considering equations (2.27), (2.28) and (2.19):

$$\sigma_\gamma\left(E\right) = \frac{1.02 \cdot 11.9 \cdot NZ}{3\pi A} \sum_{k=1}^{3} \frac{E^2\Gamma_k}{\left(E_k^2 - E^2\right)^2 + E^2\Gamma_k^2} \text{ fm}^2 \tag{2.29}$$

Since the distribution used in this equation is a Lorentzian, the constant 1.02 is the conversion factor between the integrals of Lorentz and Breit-Wigner distributions. The σ_m parameter of the Breit-Wigner distribution given by equation (2.20) can be expressed in terms of the TRK sum rule in a similar way [2]:

$$\sigma_m = \frac{60 \cdot 2}{\pi\Gamma} \cdot \frac{NZ}{A} \text{ mb} \tag{2.30}$$

which is equivalent to the sum pre-factor of equation (2.29) after unit conversion.

2.3.2 Statistical Decay of Giant Resonances

Giant dipole resonances are usually located above a particle threshold (neutron and/or proton) of the nucleus. They can therefore decay *via* several reaction channels, *e.g.*, pure gamma decay, semi-direct decay and compound nucleus decay. The latter decay channel is most often the dominant one, and will therefore be described here.

The decay of a compound nucleus is well described by statistical models, such as the Fermi-gas model. Starting from the Weisskopf-Ewing formula [29], the emission spectrum is given by the following equation:

$$N\left(E_{kin}\right) dE_{kin} = C \cdot E_{kin}\sigma_c\left(E_{kin}\right) \rho\left(O, U\right) dE_{kin} \tag{2.31}$$

where C contains all constant values of the Weisskopf-Ewing formula, σ_c is the capture cross section for the inverse process, and $\rho\left(O, U\right)$ is the level density of an $I = 0$ daughter nucleus with an internal excitation energy of U MeV. Assuming that all nucleons are in

a thermal equilibrium in the compound nucleus, the level density can be described using the Boltzmann entropy formula:

$$\rho\left(O,U\right) \propto \exp\left[S\left(U\right)\right] \tag{2.32}$$

If the remaining excitation energy U is small, the entropy can be expressed as the first term of a Taylor series:

$$S\left(U\right) = \frac{\partial S}{\partial U}\, U + \ldots \ , \quad \text{with} \left(\frac{\partial S}{\partial U}\right) = \frac{1}{T} = \text{const.} \tag{2.33}$$

where T is the nuclear temperature. Also, if $U = E^* - S_n - E_{kin}$ for the emission of neutrons can be approximated by $U = -E_{kin}$, leading to the constant-temperature model, equation (2.31) can be reduced to:

$$N\left(E_{kin}\right) dE_{kin} = C \cdot E_{kin} \sigma_c\left(E_{kin}\right) \exp\left[\frac{-E_{kin}}{T}\right] dE_{kin} \tag{2.34}$$

which is equivalent to the frequently used Maxwell distribution formula [13, 29, 30]. The nuclear temperature is analogous to the thermodynamic temperature, for which one sets the Boltzmann constant to $k = 1$, such that the temperature is expressed in energy units (MeV for the case of equation (2.34)). The temperature can be calculated with the following expression:

$$T = \sqrt{\frac{U}{a}} \tag{2.35}$$

where a is the level density parameter of the nucleus. The calculation of the level density parameter is not a trivial task, since precise knowledge of the nuclear structure is required. Often, the following approximation is used:

$$a = \frac{A}{C_A}\ \text{MeV}^{-1} \tag{2.36}$$

with the mass number A and the proportionality constant C_A. The value of C_A is not well defined, and takes the value 7.5 [29], 10 [13] or 8 [31]. The value of a is particularly small for closed-shell nuclei: since nickel nuclei ($Z = 28$ closed shell) have been measured in the present experiment, considerable deviations from equation (2.36) can be expected.

While describing the properties of statistical decay, Weisskopf states [30] that equation (2.34) is only valid if one particle is emitted. Le Couteur *et al.* [31] argue that if more than one particle is emitted by the nucleus, the following equation must be used instead of expression (2.34):

$$N\left(U_0, E_{kin}\right) dE_{kin} \propto \sigma_c \frac{E_{kin}^{l-1}}{T_*^l} \exp\left[\frac{-E_{kin}}{T_*}\right] dE_{kin} \tag{2.37}$$

If $U = aT^2$ (*cf.* equation (2.35)), l and T_* take the following values [31]:

$$l \approx \frac{16}{11}, \quad T_* \approx \frac{11}{12} T \tag{2.38}$$

where T is the updated nuclear temperature of the daughter nucleus, depending on the number, kinetic energies and binding energies of the emitted particles. Comparing the shapes of the kinetic energy distributions described by equations (2.34) and (2.37) (considering the values from expression (2.38)), the main difference lies in the kinetic-energy-dependent exponential pre-factor: for a single evaporated particle, this factor is E_{kin}, while it changes to approximately $\sqrt{E_{kin}}$ for more than one particle.

2.4 Special Features of Exotic Nuclei

In most, if not all, scientific fields of study, one tries to rationalize observations into simple rules for a better understanding of complex phenomena, or to extrapolate various properties to still unobserved systems. In nuclear physics, such rules (*e.g.*, magic numbers) and systematical trends (*e.g.*, semi-empirical GDR systematics) are built on the observations of stable and long-lived unstable nuclei, since they are accessible since several decades. In the more recent years, the ability to produce nuclei always farther from the valley of β-stability has been achieved. These exotic nuclei exhibit interesting new features, that are not foreseen by the existing systematical rules. For instance, light neutron-rich nuclei can present a neutron halo formed by the valence neutrons. Heavier nuclei with a neutron excess exhibit an outer layer of increased neutron density, the so-called neutron skin [3]. The dynamical behavior of neutron-rich nuclei also presents several new effects, such as the fragmentation of IVGDR strength due to different effective potentials of the core and valence neutrons [10]. The large neutron excess also induces an accumulation of E1 strength well below the GDR. This new collective mode, known as the Pygmy Dipole Resonance (PDR), can be described as an out-of-phase oscillation of a neutron-enriched surface layer against the core nucleons [3].

Pygmy resonances, or giant resonances in general, can be calculated by several theoretical models, most of which are based on the Random Phase Approximation (RPA). RPA is a useful tool to investigate collective oscillations of small amplitude, where the precise knowledge of the wave functions is not necessary. To simulate an oscillation, a mean field theory can be applied to the nuclear system in order to describe the stationary states. The RPA resides in the extension of the mean field model to time-dependent states, making the system dynamic [20]. Figure 2.3 shows a model calculation performed by Paar *et al.* for the pygmy dipole resonances in the nickel isotopic chain using the Relativistic Hartree-Bogoliubov (RHB) self-consistent mean-field model, along with the Relativistic Quasiparticle RPA (RQRPA) [3]. Another calculation carried out by Liang *et al.* is based on the relativistic random-phase approximation, also showing low-lying dipole strength in figure 2.4. Non-linear isoscalar-isovector coupling *via* the coupling constant Λ_v has also been included. The shown results have been obtained by using the NL3 parameter set as effective force for the relativistic mean-field calculations. A

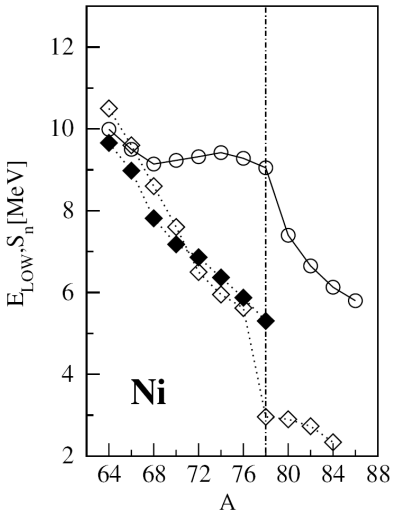

Figure 2.3: RHB+RQRPA calculation for the PDR in nickel isotopes. Open circles: Pygmy Dipole Resonance centroid energies of nickel isotopes as a function of mass number A. Open diamonds: calculated Ni 1n thresholds. Full diamonds: measured Ni 1n thresholds. From Paar *et al.* [3].

third RPA calculation is shown in figure 2.5, where the RQRPA has been implemented with the relativistic quasiparticle time-blocking approximation. The individual peaks have been artificially smeared with a width of 20 keV and 200 keV in the left and right panels, respectively. Although all three cited calculations are slightly different, they all predict a clear dipole-resonance mode well below the GDR.

The degree of collectivity is a recurring question in the investigation of the PDR. Besides being a collective resonance, the PDR could be seen as non-collective dipole strength, located at lower energies due to the less bound outer neutron orbitals [3]. Sum rules measure the collective character of a resonance: either the TRK sum rule [6] or cluster sum rules ([6] and references therein) can be used. Typical pygmy dipole resonances exhibit only a few percent of the TRK sum rule strength, which indicates that most of the nucleons do not participate in the collective mode, which in turn is consistent with the hydrodynamical picture of an oscillation of the neutron skin against the core nucleons.

The knowledge of the PDR strength distribution does not only contribute to a better understanding of the dynamics of the nucleus, but also to the basic properties of nuclear matter and to astrophysical issues. By investigating systematically the PDR over an isotopic chain, information on the equation-of-state of neutron matter can be obtained [7], such as the symmetry energy of pure neutron matter, which is an important quantity for the realistic modeling of neutron stars. For the case of neutron-rich tin isotopes, the symmetry energy of pure neutron matter was obtained from an RPA

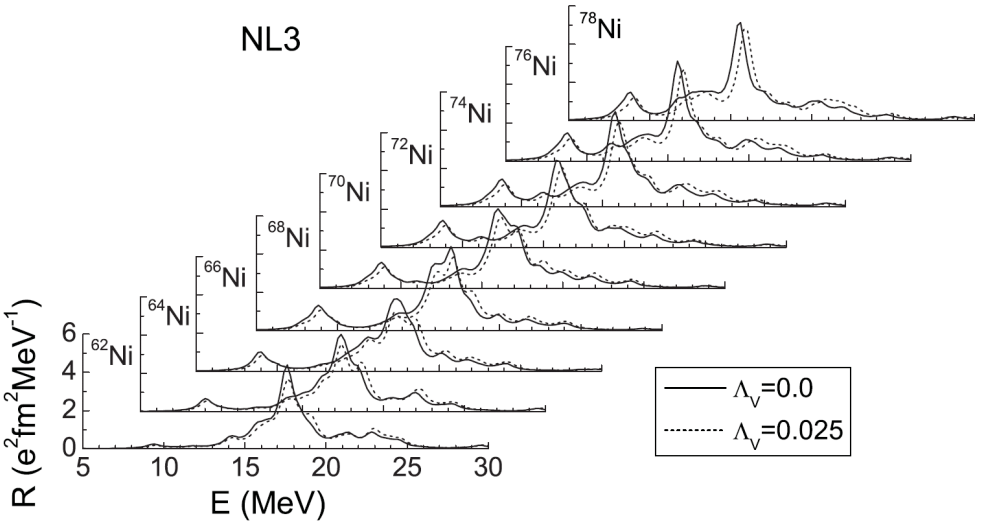

Figure 2.4: Dipole strength distributions for even-mass neutron-rich nickel isotopes. The relativistic random-phase approximation (RRPA) was used, including also non-linear isoscalar-isovector coupling *via* the coupling constant Λ_v. From Liang *et al.* [32].

calculation and from the measured PDR strength relative to the GDR strength. In turn, this energy value can be used to extract the neutron-skin thickness. Although the PDR strength is small compared to the GDR, it plays an important role in the modeling of nucleosynthesis by modifying the (n,γ) and (γ,n) cross sections [33,34]. Figure 2.6 shows the r-process abundances for two different temperature, neutron density and irradiation time conditions. The smaller neutron density in the left panel reveals the impact of low-lying strength on the abundance, shifting the mass distribution to higher values. This is explained by the lack of (n,γ)$\Leftrightarrow$(γ,n) equilibrium, since the individual reaction rates are comparable to the β-decay rates [33]. In the right panel, where the equilibrium conditions are met, the PDR does not play a major role for the abundance distribution. The result is, however, independent of the nature of the low-lying strength, since only the total level density plays a role [34].

Low-lying dipole strength has been observed previously in several nuclei, starting with neutron-rich oxygen isotopes and reaching up to ^{208}Pb. Since the presence of the PDR is linked to the proton-neutron asymmetry, it can only be studied with stable nuclei in the high-mass region [35]. The access to short-lived nuclei using radioactive beam facilities allows the investigation of this collective mode in much lighter systems. A measurement with neutron-rich oxygen isotopes [4] has shown the presence of an accumulation of E1 strength well below the GDR region. Analyzing the measured cross section, up to 12% of the Thomas-Reiche-Kuhn sum rule is exhausted by the resonances in this region. Later, another experiment with neutron-rich Sn isotopes has been

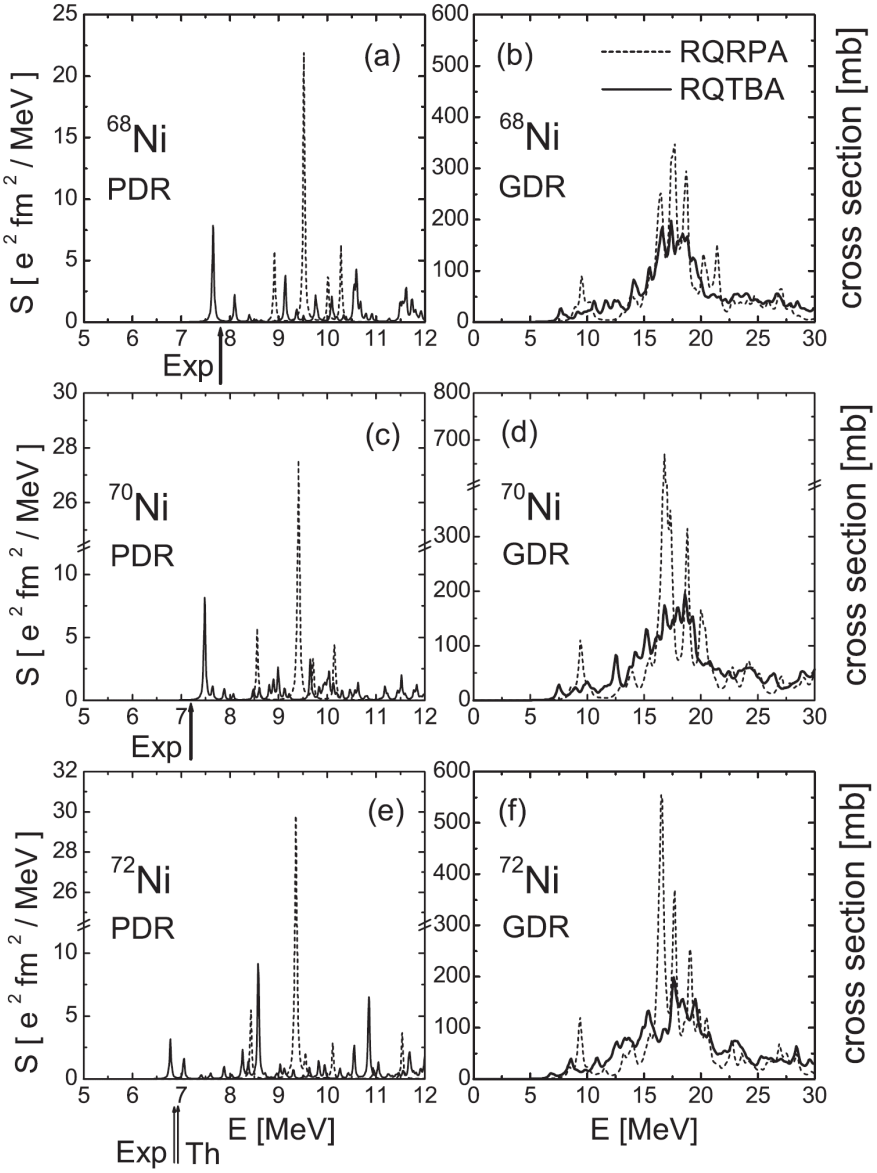

Figure 2.5: RQRPA and RQTBA dipole response calculation for Ni isotopes. The right panels show the energy range for the PDR and the GDR, while the left panels show only the PDR region. From Litvinova *et al.* [9].

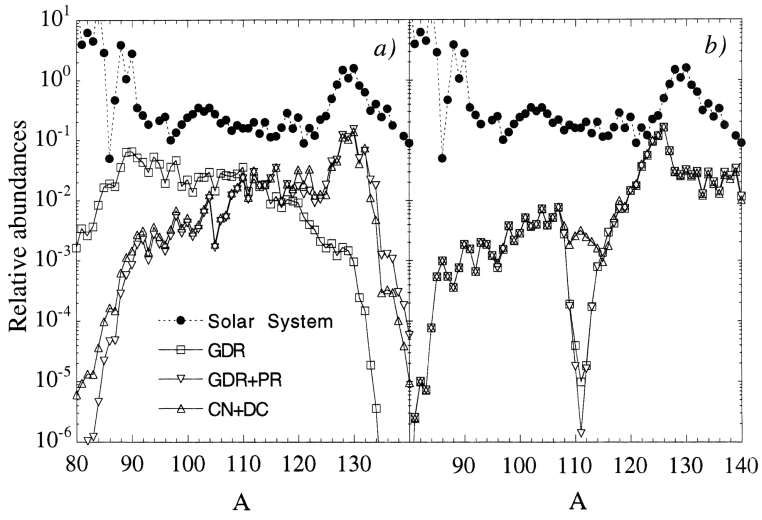

Figure 2.6: Calculated r-process abundances compared to the solar system abundances. Left panel (a): abundance distributions for $T = 10^9$ K, a neutron density of 10^{20} cm^{-3} and an irradiation time of 2.4 seconds. Right panel (b): same distributions for $T = 1.5 \cdot 10^9$ K, a neutron density of 10^{28} cm^{-3} and an irradiation time of 0.3 seconds [33].

carried out [6]. Here again, PDR strength has been observed, as shown in figure 2.7. The measured neutron-rich isotopes are compared to the photoabsorption measurement on the stable ^{124}Sn nucleus, of which the GDR is well described by a Lorentzian function. The unstable isotopes present an excess of E1 strength below the GDR region, which is attributed to the PDR, exhausting 7(3) and 4(3)% TRK sum-rule strength for ^{130}Sn and ^{132}Sn, respectively [6]. These results lead to values for the symmetry energy of pure neutron matter by interpolation on a RQRPA calculation [7]. An average value of 32.0 ± 1.8 MeV was obtained from the ^{130,132}Sn analysis. Using this value, a neutron skin thickness of 0.23 ± 0.04 fm and 0.24 ± 0.04 fm has been obtained for ^{130}Sn and ^{132}Sn, respectively, using a similar interpolation procedure. Recently, the E1 strength of ^{68}Ni has been measured by virtual photon scattering [8], which shows an accumulation of cross section near 11 MeV which cannot be described by the GDR alone, as shown in figure 2.8. The upper limit of the width of this PDR is 1 MeV, while exhausting approximately 5% of the TRK sum-rule strength assuming a total gamma-branching ratio of approximately 0.4% and 4% for the GDR and PDR regions, respectively. This result is of great interest for the present experiment, since it provides a comparison with data obtained with a different experimental setup.

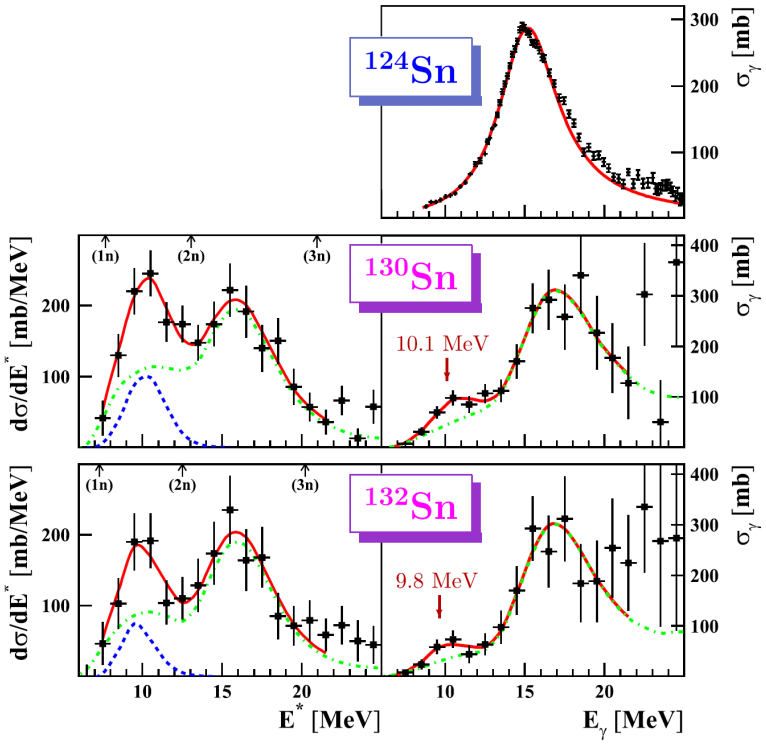

Figure 2.7: Pygmy dipole strength in ^{130,132}Sn. Left panels: energy-differential electromagnetic excitation cross sections. Right panels: photoabsorption cross sections. From Adrich *et al.* [6].

2.5 Heavy-ion-induced Electromagnetic Excitation

2.5.1 Preliminary Issues

Giant resonances are excited by the interaction of the nucleus with a probe *via* the strong or the electromagnetic interaction. The different GR modes described in section 2.3 often overlap in energy, such that they cannot be distinguished based on the choice of excitation energy alone. One therefore tries to choose a selective probe, in order to excite only a restricted class of resonances. Inelastic scattering of hadronic probes is often used. For non-spin-flip isoscalar modes, (α,α') is a common tool, since the α-particle is a $S = 0$ and $T = 0$ probe, as well as scattering of ^{12}C and ^{16}O, although the latter probes can mix hadronic and electromagnetic interactions, depending on the energy of the projectile [1]. Protons, deuterons, and in general hadronic probes with non-zero spin and isospin can also excite $\Delta S = 1$ and/or $\Delta T = 1$ GR modes. Giant resonances can also be studied by purely electromagnetic probes, such as electrons and photons. Inelastic electron scattering is a powerful tool for the measurement of transition densities and for the disentangling of the various multipole modes of the GR, by studying the form factor. However, electrons excite isovector as well as isoscalar modes and create

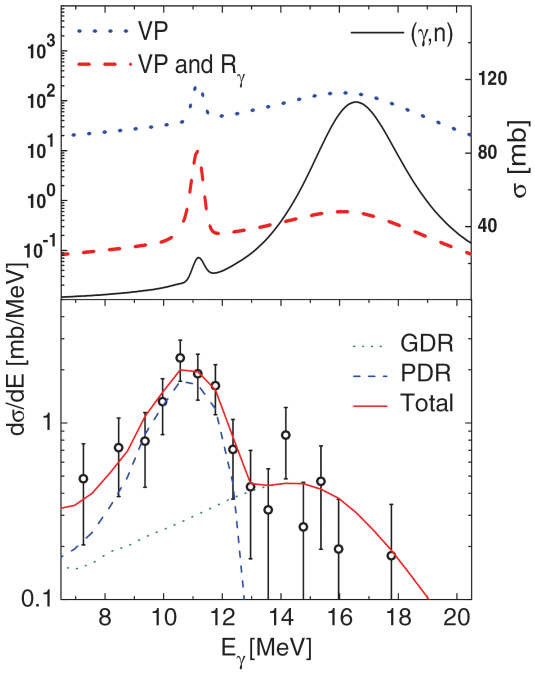

Figure 2.8: Dipole strength of ^{68}Ni measured by virtual photon scattering. Top panel: photoabsorption and electromagnetic excitation cross section distributions. The blue dotted line only takes the virtual photon spectrum into account, while the red dashed line also includes the gamma branching ratio. Bottom panel: measured electromagnetic excitation cross section, with GDR and PDR distributions folded with the detector response. From Wieland *et al.* [8].

an unwanted continuum in the spectra due to the large elastic scattering cross section in inclusive measurements. Photons, on the other hand, are very selective for $\Delta T = 1$ transitions [1], making photon scattering (γ,γ') and photoabsorption (γ,xn+yp) very powerful tools for the investigation of isovector giant resonances. While photoabsorption with real photons is straightforward, it does not enable the study of short-lived nuclei, since massive targets are required. The target and projectile roles must therefore be exchanged, leaving the excitation in intense electromagnetic fields as the only realistic method.

The treatment of heavy-ion-induced electromagnetic excitation relies on the evaluation of the electric (and/or magnetic) field as a function of time and position. Even though the field can be calculated for any given trajectory of an ion through the electromagnetic field, the assumption of a rectilinear trajectory greatly simplifies the procedure. It should therefore be verified if the assumption of a linear trajectory is acceptable. When considering pure Coulomb interactions, the trajectory of an impinging (light) nucleus on a stationary heavy target is well described by Rutherford scattering, providing a hyper-

bolic trajectory. The scattering angle may be derived from the Rutherford formula given in SI units [36]:

$$\vartheta = 2 \arctan \left[\frac{Z_T Z_P q_e^2}{4\pi\epsilon_0 b \mu \beta^2 c^2 \gamma} \right] \tag{2.39}$$

where Z is the nuclear charge, q_e is the unit charge, ϵ_0 is the electric permittivity in vacuum, b is the impact parameter, μ is the reduced mass, βc is the velocity of the projectile, and γ is the associated Lorentz parameter. The largest scattering angle is given when expression (2.39) is evaluated for the smallest possible impact parameter where only the Coulomb interaction takes place.

The minimum impact parameter is an important quantity, which is used not only to evaluate expression (2.39), but also in the calculation of the equivalent photon spectrum. A simple assumption for the minimum impact parameter would be to use the sum of the radii of both interacting nuclei. The resulting values, however, do not describe experimental data well. Benesh, Cook and Vary [37] propose a parametrization partially based on the nuclear radii of heavy ions interacting at relativistic velocities:

$$b_{min}^{BCV} \approx r_0 \left(A^{1/3} + B^{1/3} - x \left(A^{-1/3} + B^{-1/3} \right) \right) \tag{2.40}$$

where A and B are the mass numbers of the two interacting nuclei. The parameters $r_0 = 1.34$ fm and $x = 0.75$ have been obtained from a fit on experimental nucleon-nucleus and nucleus-nucleus interaction data.

Using $b_{min}^{BCV} = 12.7$ fm for a ^{58}Ni nucleus impinging with 500 AMeV on a Pb target, the maximum deflection angle is of the order of 14 mrad, allowing the assumption that the trajectory of the nickel nucleus through the electric field of the lead nucleus is linear, simplifying greatly the subsequent analysis.

2.5.2 Fermi Approach

Fermi described the process of electromagnetic excitation due to a moving charge in 1924 with a non-relativistic approach [38], as shown in figure 2.9. The target nucleus, with charge $Z_T e$, is at rest, while the projectile moves along a linear trajectory, with a non-relativistic velocity $\vec{v}$. The geometry of the process can be reduced to two dimensions, onto a plane defined by the trajectory of the projectile and by the center of the target. The origin of the time scale is located at the turning point of the projectile, *i.e.*, when the projectile is at the distance of closet approach b, or impact parameter, with respect to the center of the target. The electric field $\vec{E}$ generated by the target nucleus can be described by the following identity (in natural units):

$$\vec{E}\left(\vec{r}\right) = \frac{Z_T e}{\left\|\vec{r}\right\|^2} \vec{u}_r = \frac{Z_T e}{\left\|\vec{r}\right\|^3} \vec{r} \tag{2.41}$$

where Z_T is the charge number of the target nucleus, e is the unit charge, and $\vec{u}_r$ is the unit vector of $\vec{r}$. According to the inverse kinematics geometry of figure 2.9, the position

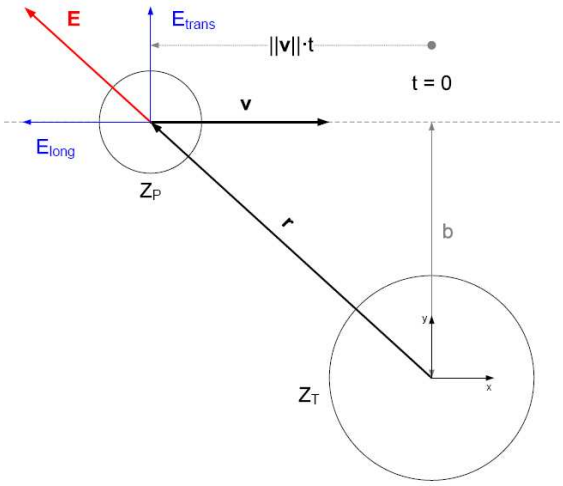

Figure 2.9: Schematic view of the geometry of heavy-ion-induced electromagnetic excitation.

vector $\vec{r}$ can be parameterized in the following way:

$$\vec{r} = \begin{pmatrix} vt \\ b \end{pmatrix}, \quad \|\vec{r}\| = \sqrt{b^2 + v^2 t^2} \tag{2.42}$$

The longitudinal and radial electric fields can be described using equations (2.41) and (2.42):

$$E_{\parallel}(t) = \frac{Z_T e v t}{\left(b^2 + v^2 t^2\right)^{3/2}}, \quad E_{\perp}(t) = \frac{Z_T e b}{\left(b^2 + v^2 t^2\right)^{3/2}} \tag{2.43}$$

Since the goal of this approach is to attribute an energy distribution to a given interaction with the parameter set $\{Z_T, v, b\}$, the electric fields in equation (2.43) must first be transformed from the time to the frequency domain *via* a Fourier transformation. The following Fourier series will describe the electric fields in expression (2.43):

$$E_{\parallel}(t) = \sum_n a_n \sin\left[\frac{2\pi n}{T} t\right], \quad E_{\perp}(t) = \sum_n b_n \cos\left[\frac{2\pi n}{T} t\right] \tag{2.44}$$

where T is the period of the function. The Fourier coefficients can be calculated with:

$$\begin{aligned} a_n &= \frac{2}{T} \int_{-T/2}^{T/2} E_{\parallel}(t) \sin\left[\frac{2\pi n}{T} t\right] dt = \frac{2 Z_T e v}{T} \int_{-T/2}^{T/2} \frac{t \sin\left[\frac{2\pi n}{T} t\right]}{\left(b^2 + v^2 t^2\right)^{3/2}} \, dt \\ b_n &= \frac{2}{T} \int_{-T/2}^{T/2} E_{\perp}(t) \cos\left[\frac{2\pi n}{T} t\right] dt = \frac{2 Z_T e b}{T} \int_{-T/2}^{T/2} \frac{\cos\left[\frac{2\pi n}{T} t\right]}{\left(b^2 + v^2 t^2\right)^{3/2}} \, dt \end{aligned} \tag{2.45}$$

Using these expressions, expression (2.44) represents the electric fields of light waves, which can be described by the corresponding frequency spectrum [36]:

$$\frac{dI(\nu, b)}{d\nu} = \frac{c}{2\pi} |E(\nu, b)|^2 \tag{2.46}$$

By defining the frequency as $\nu = n/T$ in equations (2.45) and by expanding the period of the function to $\pm\infty$, the spectrum of the combined longitudinal and transverse electric fields is described by:

$$\frac{dI(\nu,b)}{d\nu} = \frac{cZ_T^2e^2}{2\pi}\left(b^2\left(\int_{-\infty}^{\infty}\frac{\cos[2\pi\nu t]\,dt}{(b^2+v^2t^2)^{3/2}}\right)^2 + v^2\left(\int_{-\infty}^{\infty}\frac{t\sin[2\pi\nu t]\,dt}{(b^2+v^2t^2)^{3/2}}\right)^2\right) \quad (2.47)$$

The solutions of the two integrals in equation (2.47) are modified Bessel functions of the second kind, simplifying the intensity expression to:

$$\frac{dI(\nu,b)}{d\nu} = \frac{8\pi cZ_T^2e^2\nu^2}{v^2}\left(K_0^2\left(\frac{2\pi\nu b}{v}\right) + K_1^2\left(\frac{2\pi\nu b}{v}\right)\right) \quad (2.48)$$

where K_0 and K_1 are modified Bessel functions of the second kind of order zero and one, respectively. The approach described by Fermi shows the derivation of the frequency (or energy) spectrum based on a time-varying electric field. Although the results presented in this subsection cannot be used directly for the interpretation of the present experiment, it shows in a reasonably simple manner the underlying concepts of the various descriptions of heavy-ion-induced electromagnetic excitation.

2.5.3 Weizsäcker-Williams Approach

The following equivalent photon approach was developed in 1934 independently by Weizsäcker and Williams, and describes the process of electromagnetic excitation while taking relativistic effects into account. While still in inverse kinematics (*cf.* figure 2.9), the electric fields of equation (2.43) must be modified [1, 36, 39]:

$$E_\parallel(t) = \frac{Z_Te\gamma vt}{(b^2+\gamma^2v^2t^2)^{3/2}}\ ,\quad E_\perp(t) = \frac{Z_Te\gamma b}{(b^2+\gamma^2v^2t^2)^{3/2}} \quad (2.49)$$

For completeness, the magnetic fields generated by the motion of the charge are:

$$B_\parallel(t) = 0\ ,\quad B_\perp(t) = \beta E_\perp(t) \quad (2.50)$$

The left panel of figure 2.10 shows the electric fields of equations (2.49) for a Pb target nucleus and a projectile with a velocity of $\beta = 0.75$ and an impact parameter $b = 12.7$ fm, corresponding to the minimum impact parameter for a ^{58}Ni nucleus. The right panel of the same figure illustrates the distortion of the electric field seen by a projectile due to its relativistic velocity. Qualitatively, if the velocity of the projectile increases, the transversal electric field will become narrower due to the reduced interaction time. Since a narrow time distribution produces a wide frequency distribution after a Fourier transformation, the frequency spectrum will therefore reach out to higher values for the higher projectile velocity. As the frequency distribution decreases asymptotically on

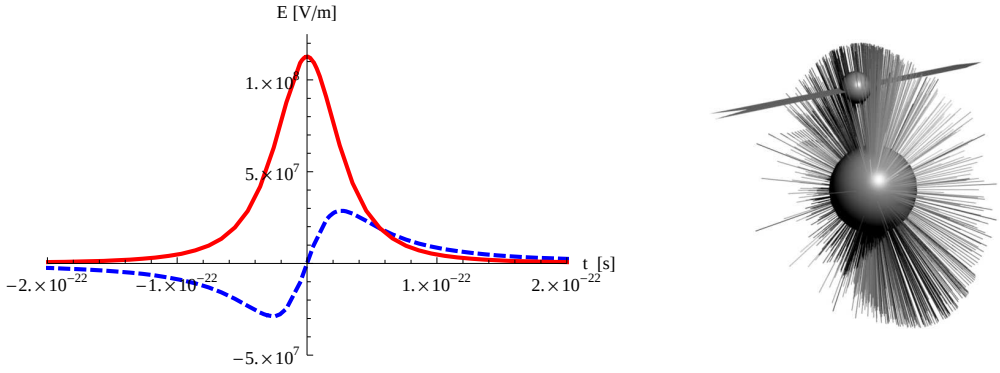

Figure 2.10: Left panel: longitudinal (dashed blue line) and transversal (solid red line) electric fields as a function of time. Values for a $Z = 82$ nucleus with $\beta = 0.75$ and $b = 12.7$ fm. Right panel: view of relativistic distortion of electric field.

the high-frequency side, a maximum excitation energy cannot be defined. The so-called adiabaticity parameter ξ is defined as the ratio of the collision time to the excitation time. The parameter must be smaller than unity in order for an excitation to take place. Otherwise, the duration of the collision is too long, and the interaction will be adiabatic, *i.e.*, without any energy transfer. The adiabaticity parameter is defined as:

$$\xi = \frac{\epsilon b}{\hbar \gamma \beta c} \tag{2.51}$$

where ϵ is the excitation energy and b is the impact parameter. Based on this definition, the maximum excitation energy can be estimated if $\xi = 1$ and if $b = b_{min}$:

$$\epsilon_{max} = \frac{\hbar \gamma \beta c}{b_{min}} \tag{2.52}$$

Taking again the example of a ^{58}Ni nucleus traveling with $\beta = 0.75$ onto a Pb target ($b_{min} = 12.7$ fm), the maximum excitation energy according to equation (2.52) is 17.6 MeV. For the quantitative understanding of the frequency spectrum, a Fourier transformation similar to expression (2.44) is applied on equation (2.49) to generate a frequency spectrum of the two perpendicular electric fields according to equation (2.46) [36]:

$$\begin{aligned} \frac{dI_{\parallel}(\omega, b)}{d\omega} &= \frac{1}{\pi^2} \frac{Z_T^2 e^2}{c} \left(\frac{c}{v}\right)^2 \frac{1}{b^2} \xi_b^2 K_1^2(\xi_b) \\ \frac{dI_{\perp}(\omega, b)}{d\omega} &= \frac{1}{\pi^2} \frac{Z_T^2 e^2}{c} \left(\frac{c}{v}\right)^2 \frac{1}{b^2} \frac{1}{\gamma^2} \xi_b^2 K_0^2(\xi_b) \end{aligned} \tag{2.53}$$

with $\omega = 2\pi\nu$ and $\xi_b = \frac{\omega b}{\gamma v}$. Both intensity components of equation (2.53) must be added together in order to describe the interaction felt by the projectile nucleus. Each value of b will generate a different spectrum. Since the impact parameter cannot be measured,

the spectrum will be integrated over all possible impact parameter values [36, 37]:

$$\begin{aligned}\frac{dI(\omega)}{d\omega} &= 2\pi \int_{b_{min}}^{\infty} \left(\frac{dI_{\parallel}}{d\omega}(\omega, b) + \frac{dI_{\perp}}{d\omega}(\omega, b) \right) b \; db \\ &= \frac{2}{\pi} \frac{Z_T^2 e^2}{c} \left(\frac{c}{v} \right)^2 \left(\xi K_0(\xi) K_1(\xi) - \frac{v^2}{2c^2} \xi^2 \left[K_1^2(\xi) - K_0^2(\xi) \right] \right)\end{aligned} \tag{2.54}$$

with the adiabaticity parameter $\xi = \frac{\omega b_{min}}{\gamma v}$. Based on equation (2.54), the so-called number of virtual quanta $N(\hbar\omega)$ can be calculated:

$$\frac{dI(\omega)}{d\omega} d\omega = \hbar\omega N(\hbar\omega) \; d(\hbar\omega) \tag{2.55}$$

One of the most important features of the Weizsäcker-Williams method is the link between the virtual photon spectrum and the electromagnetic excitation cross section *via* equation (2.55):

$$\begin{aligned}\sigma_C &= \int N(\hbar\omega) \sigma_{\gamma}(\hbar\omega) \; d(\hbar\omega) \\ &= \int \frac{1}{\hbar\omega} \frac{dI(\omega)}{d\omega} \sigma_{\gamma}(\omega) \; d\omega\end{aligned} \tag{2.56}$$

where σ_C is the electromagnetic excitation (or Coulomb) cross section and σ_{γ} is the photoabsorption cross section.

Although the approach presented above provides the description of the virtual photon field for the set of electric fields in expression (2.49), it cannot be used directly for the understanding of the various giant-resonance modes. The reduced transition rates for electromagnetic processes $B(\sigma\lambda, I_i \rightarrow I_f)$, as shown in subsection 2.1, provide the strength of a transition based on the transition operator. The sum rules of subsection 2.2 indicate the integral cross section that can be expected for a given transition, but do not contain any information of the photoabsorption strength distribution, which is crucial for the conversion to the electromagnetic excitation strength distribution, as shown by equation (2.56). The calculation of the photoabsorption cross section from the reduced transition rate for a given giant resonance $(\pi\lambda)$-mode is given by the following expression [40, 41]:

$$\sigma_{\gamma}^{\pi\lambda}(\epsilon) = \frac{(2\pi)^3 (\lambda + 1)}{\lambda \left[(2\lambda + 1)!! \right]^2} \sum_f \rho_f(\epsilon) \kappa^{2\lambda - 1} B(\pi\lambda, I_i \rightarrow I_f) \tag{2.57}$$

where ϵ is the excitation energy, $\rho(\epsilon)$ the density of final states as a function of excitation energy, and $\kappa = \omega/c$. The total photoabsorption cross section is then simply the sum of all $(\pi\lambda)$-modes:

$$\sigma_{\gamma}(\epsilon) = \sum_{\pi\lambda} \sigma_{\gamma}^{\pi\lambda}(\epsilon) \tag{2.58}$$

In order to obtain the Coulomb excitation cross section according to equation (2.56), the total number of virtual quanta $N_{\pi\lambda}(\epsilon)$ for each $(\pi\lambda)$-mode must be calculated.

This is achieved by using a Liénard-Wiechert potential to describe the electromagnetic fields [39, 41–43], which is thereafter expanded by a Taylor series around the center of the projectile nucleus. The first and second terms of the series give rise to the E1 and M1 contributions, as well as a portion of the E2 contribution. For the full E2 excitation amplitude, the third term of the Taylor series is also required. The electromagnetic fields are expanded into multipole components using spherical harmonics, and then converted into multipole potentials. The excitation amplitudes are then calculated *via* first-order perturbation theory, using the multipole potential as the perturbation. This generates a result comparable to the Fourier-transformed electric fields of equation (2.53), with the main difference that this approach yields separate amplitudes for the various $\pi\lambda$ modes. After removal of the dependence on the impact parameter by integration, total virtual photon numbers for the major modes (E1, E2 and M1) are obtained:

$$\begin{aligned}
N_{E1}(\epsilon) &= \frac{2}{\pi} Z_T^2 e^2 \alpha \left(\frac{c}{v}\right)^2 \left(\xi K_0(\xi) K_1(\xi) - \frac{v^2 \xi^2}{2c^2}\left[K_1^2(\xi) - K_0^2(\xi)\right]\right) \\
N_{E2}(\epsilon) &= \frac{2}{\pi} Z_T^2 e^2 \alpha \left(\frac{c}{v}\right)^4 \left(2\left[1 - \frac{v^2}{c^2}\right] K_1^2(\xi) + \xi \left[1 - \frac{v^2}{c^2}\right]^2 K_0(\xi) K_1(\xi)\right. \\
&\quad \left. + \frac{\xi^2 v^4}{2c^4}\left[K_1^2(\xi) - K_0^2(\xi)\right] + \xi^2 \left[2 - \frac{v^2}{c^2}\right]^2 K_1^2(\xi)\right) \\
N_{M1}(\epsilon) &= \frac{2}{\pi} Z_T^2 e^2 \alpha \left(\xi K_0(\xi) K_1(\xi) - \frac{\xi^2}{2}\left[K_1^2(\xi) - K_0^2(\xi)\right]\right)
\end{aligned} \tag{2.59}$$

with the adiabaticity parameter $\xi = \epsilon b_{min}/\hbar\gamma v$ and the fine-structure constant α. Using these total virtual photon numbers, the electromagnetic excitation cross section can be calculated with:

$$\sigma_C = \sum_{\pi\lambda} \sigma_C^{\pi\lambda} = \sum_{\pi\lambda} \int \frac{d\epsilon}{\epsilon} N_{\pi\lambda}(\epsilon)\, \sigma_\gamma^{\pi\lambda}(\epsilon) \tag{2.60}$$

which is equivalent to expression (2.56). Figure 2.11 shows a series of E1, M1 and E2 total virtual photon numbers for a ^{58}Ni beam impinging on a Pb target (Z=82) with 500 AMeV. For comparison, the adiabatic cut-off energy is 18 MeV for this energy. It should be noted that at high virtual photon numbers, multiple excitation can occur. This effect can be safely neglected at low energies, but can modify substantially the shape of the virtual photon field at high energies. The beam energies of the present experiment are located around 500 AMeV, where the probability of multiple excitation is still relatively small [44], which is therefore neglected in the data analysis.

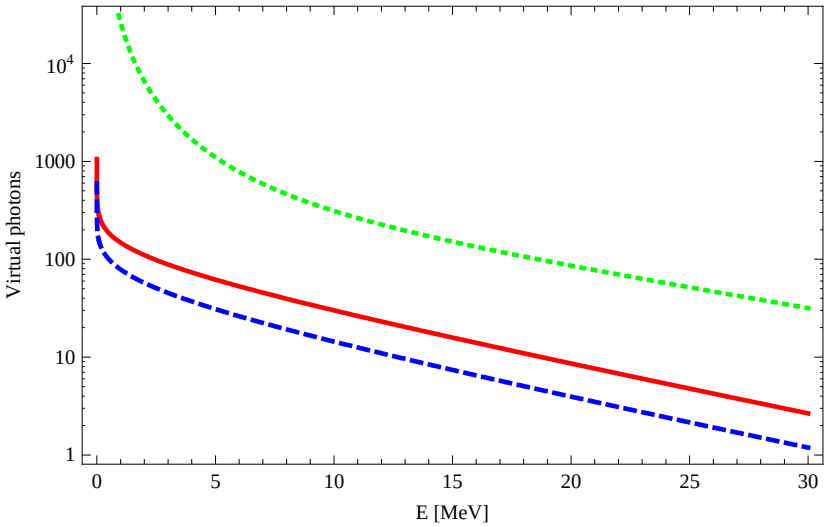

Figure 2.11: Total virtual photon numbers for ^{58}Ni impinging on a Pb (Z=82) target with 500 AMeV. The E1 (solid red line), M1 (dashed blue line) and E2 (dotted green line) photon fields are shown.

Chapter 3

Experimental Setup

The experimental details of the nickel experiment are presented in this chapter. Starting with a general description of the GSI accelerator complex as well as of the FRagment Separator (FRS), the main attention will be drawn to the setup of the detectors in Cave C. After passing in review the major detector systems, a glimpse at the future FAIR* facility will be given. The overall R^3B† setup concept will be shortly discussed before drawing attention to NeuLAND, the successor of the existing LAND detector. Since its development has already begun, first test results will be presented, which constitute one of the first steps towards the new detector system for fast neutrons.

3.1 GSI Accelerator Layout

The schematic layout in figure 3.1 depicts the existing GSI complex (in blue), as well as the planned FAIR facility (in red, to the east of the existing GSI accelerators). The present experiment took place in Cave C at GSI, which is located at the southern end of the experimental hall. The primary ion beam is generated by the ion sources located at the west end of the facility before being injected into the UNIversal Linear ACcelerator (UNILAC), which accelerates the ions up to an energy of 11.4 AMeV [45]. The beam is then passed to the SIS 18 synchrotron (SchwerIonenSynchrotron), which accelerates the ions to the desired energy. The versatility of the UNILAC and SIS accelerators gives access to ion beams of all possible stable and long-lived unstable primary beams, ranging from protons to ^{238}U with maximum energies of 4.5 GeV and 1 AGeV, respectively [46]. For the present experiment, two primary beams were used: ^{58}Ni for the neutron-deficient nickel runs and ^{86}Kr for the neutron-rich nickel runs. After the final acceleration in the SIS, the primary beams are directed towards the FRS, which will be described in the following section.

*Facility for Antiproton and Ion Research

†Reactions with Relativistic Radioactive Beams

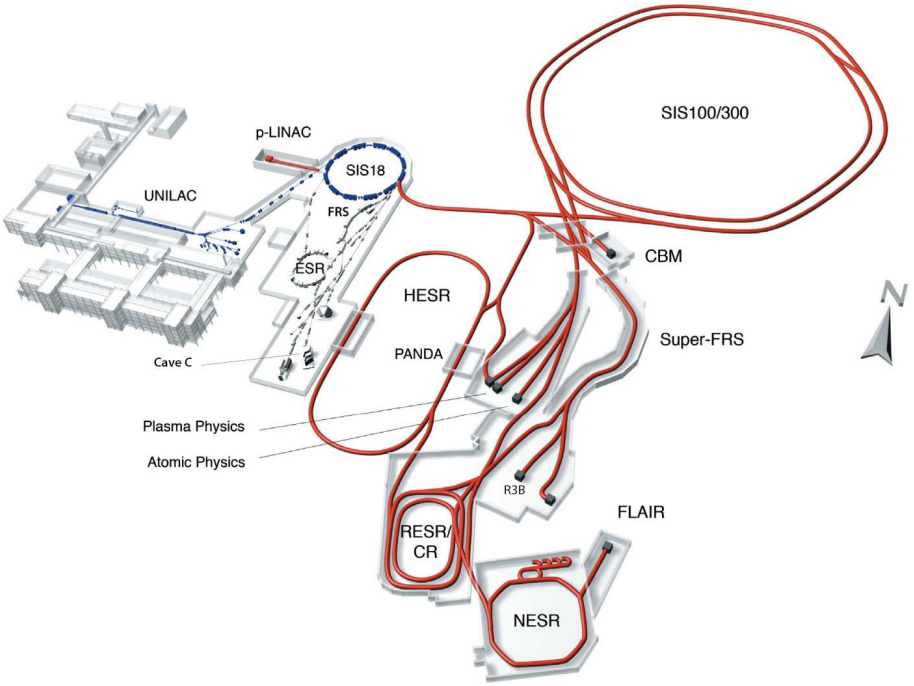

Figure 3.1: GSI accelerator complex with future FAIR facility. The existing GSI accelerators are depicted in blue and those of FAIR in red.

3.2 Fragment Separator FRS

The production of secondary ion beams is achieved with the FRS [46–48], located at the exit of the SIS 18 synchrotron. In order to produce radioactive beams, the high energy primary beam interacts with a 4.19 g/cm^2 Be production target, as seen in figure 3.2. A broad distribution of nuclei is produced *via* nuclear fragmentation due to the relativistic energy of the projectiles. The unreacted beam and the fragments enter the first two FRS dipole magnets, which filter out all species except those with a specific A/Z ratio, according to the setting of the magnetic field. The passage of a charged particle through a magnetic field is described by:

$$B\rho = \frac{p}{Q} \propto \frac{A}{Z}\beta\gamma \tag{3.1}$$

where B is the strength of the magnetic field, ρ is the curvature radius of the trajectory, p and Q are the momentum and charge of the particle, respectively, A and Z are the mass and charge numbers, respectively, of the particle, β is its velocity, and γ is the associated Lorentz factor. It should be noted that expression (3.1) does not take the mass defect into account. While A and Z are defined by the ion of interest and ρ is fixed by the geometry of the FRS, the value of B must be adjusted for a given ion. The velocity of the ions is related to their production mechanism. The width of the velocity

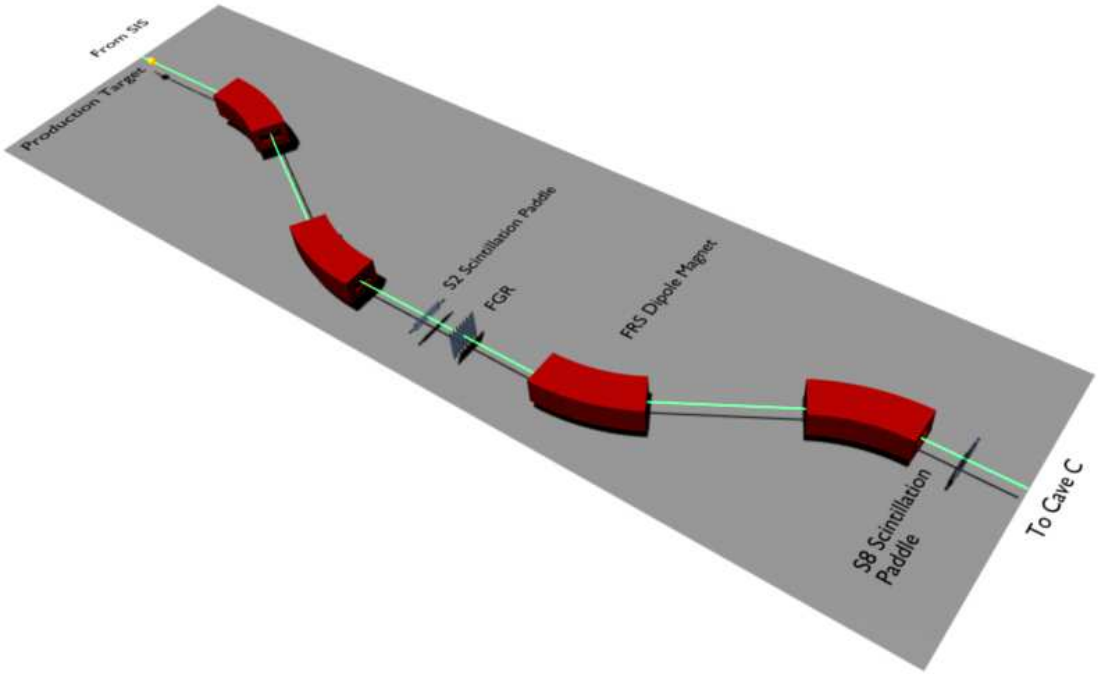

Figure 3.2: Schematic drawing of the Fragment Separator (FRS). The three scintillator detectors used in the analysis are also shown.

distribution must be narrow in order to prevent losses due to the limited acceptance of the magnets, forcing the velocity variation between the primary and secondary ion beams to be small.

With a FRS momentum resolution of $\Delta p/p = 2\%$ [46], the secondary ion beam still includes multiple species at the F2 focal plane (after the first two dipole magnets). If a pure beam is requested, a degrader can be inserted into the beam path at this location. Since the energy loss is proportional to Z^2 (*cf.* the Bethe-Bloch formula (5.21)), the magnetic rigidity of the various charges will be different in the second $B\rho$ separation stage in the third and fourth dipole magnets, which allows the isolation of a pure secondary beam. In the present case, however, the FRS was set to produce a so-called cocktail beam, containing several species with similar intensities, allowing a simultaneous measurement of various nuclei, since each ion is tracked and identified on an event-by-event basis.

The FRS is fully equipped with detectors for the tracking of the ions. Three plastic scintillator detectors are of special interest, since their data is required by the analysis, and are therefore shown in figure 3.2. Two plastic-scintillator paddles, each of which is

read out by two photomultipliers, are placed at the F2 (in the middle of the FRS) and F8 (at the end of the FRS) focal planes, respectively. The S2 and S8 scintillators can provide the velocity measurement of the incoming ions. Since the trajectory between S2 and S8 is not rectilinear, the distance between both detectors is not well defined, since it depends on the effective beam trajectory. The actual velocity measurement will be performed with the S8 scintillator and the POS detector in Cave C, which will be presented in the following section. The third important FRS detector is the FGR – or finger – detector, which mainly provides the lateral distance of the ions with respect to the optical axis of the FRS at the F2 focal plane. The position in the dispersive plane enters the calculation of the $B\rho$ value of each ion as a correction, which enhances the A/Z resolution. The FGR detector is drawn schematically in figure 3.3. Each photomultiplier

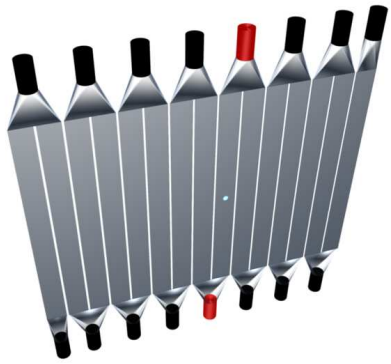

Figure 3.3: Finger detector at the F2 focal plane of the FRS. When a signal is measured in coincidence in two photomultiplier tubes (drawn in red), the lateral position is given by the position of the common paddle.

tube reads out two neighboring scintillator paddles. A hit in a given paddle triggers two PM tubes in coincidence (drawn in red in the figure), which allows the lateral position measurement. This type of detector is automatically calibrated, which is one of the main advantages of this type of readout. In order to measure the vertical position or the mean time of the hit, the PM tubes would have to be synchronized in time and energy with respect to each other. The high rates at F2, however, prevent each ion of being detected, since the probability of a given ion being shadowed by a slightly earlier one is relatively high. If the first ion does not reach Cave C, but the second one does, the precise $B\rho$ value cannot be calculated, which contributes to a loss of mass resolution. Also, the mass distribution of the fragments produced in the FRS usually peak near the valley of β-stability, meaning that less exotic fragments are more abundant. Since the masses are somewhat geometrically separated (but not resolved) in the dispersive focal plane F2, the detection probability decreases for the masses on the stable side of the distribution.

3.3 LAND Setup in Cave C

3.3.1 Setup Presentation

After the production and separation of the secondary beam in the FRS, the exotic ions enter the LAND setup in Cave C, shown in figure 3.4. The incoming beam is tracked in time by the POS scintillation detector (along with information from the S8 scintillator paddle) as well as in position by two position-sensitive pin diodes (PSP). These also provide an energy-loss measurement allowing the identification of the charge of the ion. The beam then reaches the reaction target at the front opening of the CsI gamma-detector barrel. A third PSP is placed behind the gamma detector and serves the tracking of the heavy fragments, which are then deflected in the magnetic field of the ALADIN magnet (A Large Acceptance DIpole magNet) towards the heavy fragment branch at 13.3° with respect to the incoming beam. A large vacuum chamber (not shown in fig. 3.4) was inserted into the ALADIN aperture and reached up to the beginning of the beam pipe shown in the setup drawing. The ions therefore were in vacuum since their production and up to the very end of this branch.

Unaffected by the magnetic field, the evaporation neutrons remain on their trajectory close to 0° until they reach the LAND detector (Large Area Neutron Detector). A plastic-scintillator Veto wall (not shown in fig. 3.4) is placed in front of LAND in order to distinguish protons from neutrons, since only the former produce a signal in the Veto wall. Such protons do not find their origin in the target, and therefore contribute to the background. In the fragment branch, the ions pass through three GFI fiber detectors, providing horizontal positions, which are used for tracking. A small plastic-scintillator wall, the NTF (New Time-of-Flight wall), was placed behind the third GFI. This detector was used for testing purpose only. A similar but larger detector, the TFW (Time-of-Flight Wall), provides position, time and energy-loss information of the heavy fragments and unaffected beam particles.

The following subsections will shortly describe the properties of the individual detectors of the setup. A more detailed description can be found in the thesis of Stefanos Paschalis [49].

3.3.2 Beam Tracking Detectors

When the beam reaches Cave C, the A/Z ratio is determined by the FRS, but the charge, velocity and angles of the trajectory must still be determined. The velocity is obtained by measuring the flight time of the individual ions between the S8 scintillator, placed after the fourth FRS dipole magnet, and the POS detector, a thin plastic-scintillator detector ($5\times5\times0.02$ cm^3), read out by four photomultipliers, as can be seen in figure 3.5. The time measured by POS is also the reference time of all detectors of the setup. This

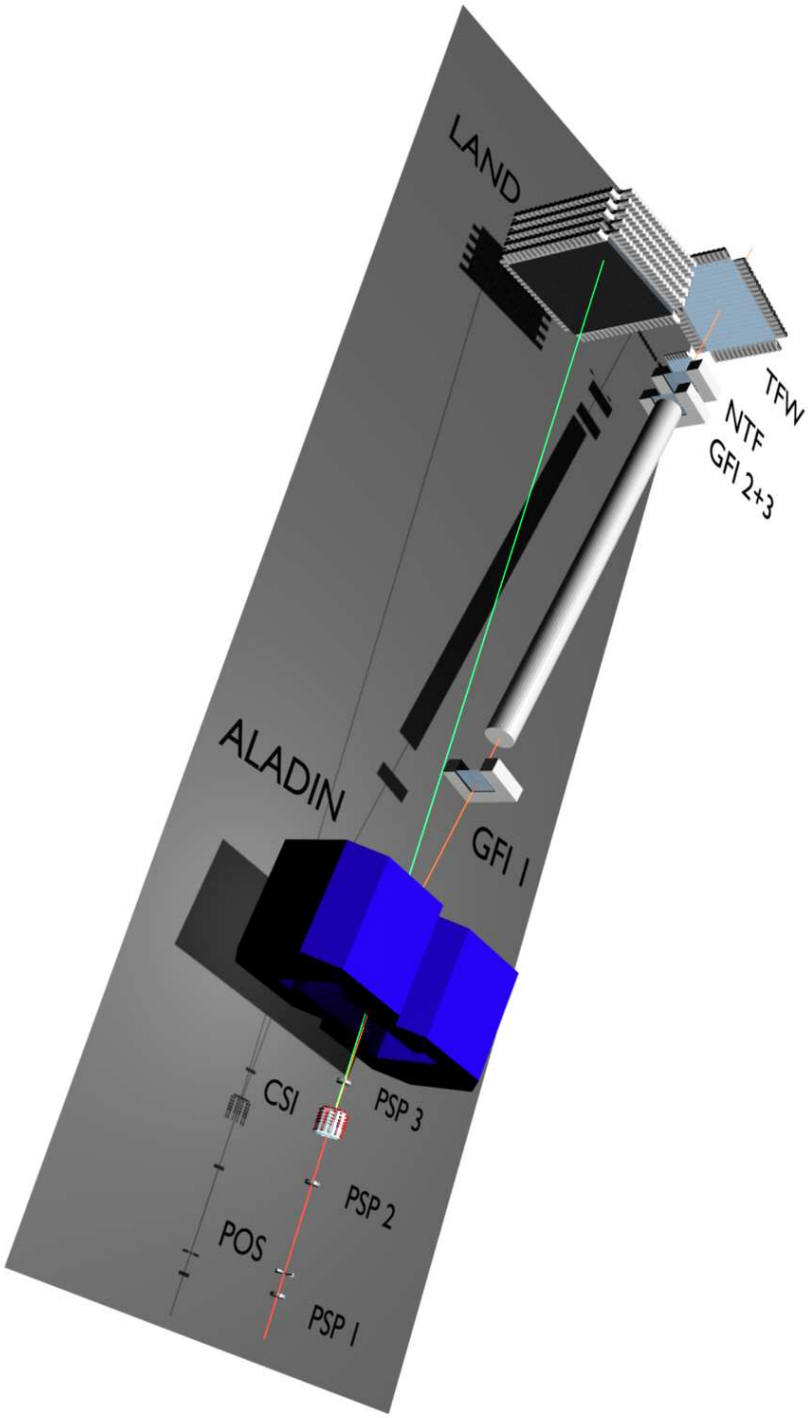

Figure 3.4: LAND setup in Cave C. The Veto wall in front of LAND and the ALADIN vacuum chamber are not shown.

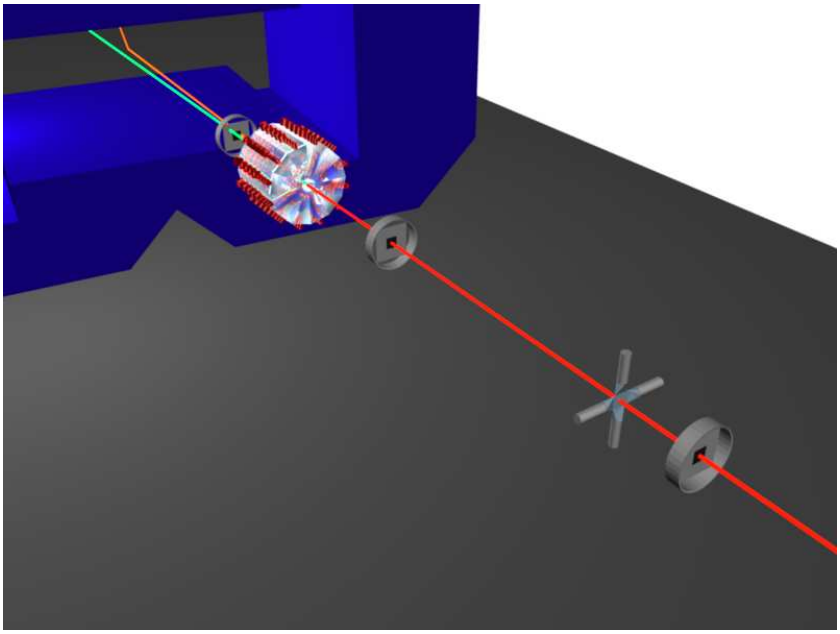

Figure 3.5: Beam tracking detectors in front of ALADIN. From right to left (beam direction): PSP1, POS, PSP2, CsI (with target) and PSP3.

detector can also provide energy-loss and position information, but these quantities are measured with a higher resolution with the position-sensitive pin diode (PSP) detectors ($4.5\times4.5\times0.03$ cm^3). Using the positions on the first two PSP detectors, the position of the reaction vertex in the target is extrapolated. The absolute time at which the ion reaches the vertex is also extrapolated using the measured velocity. In both cases, the precision of the extrapolated quantities depends strongly on the geometrical knowledge of the setup.

Two detectors are not shown in figure 3.5: the ROLU and pixel detectors. The ROLU is a set of four plastic scintillators, each of which is read out by one PM tube. The acronym ROLU stands for Rechts Oben Links Unten (right top left bottom), and indicates the position of the subunits with respect to the beam axis. Each scintillator can be driven into the beam line with a small motor, creating a rectangular variable aperture for the ions. The ROLU is usually used to collimate the beam by acting on the beam trigger in an anti-coincidence mode. In the present experiment, the ROLU was most often set to a square aperture of 2×2 cm^2.

The pixel detector is exclusively used for the position calibration of the PSP detectors. This detector is mounted on a retractable structure, allowing its removal from the beam path whenever it is not required for calibration. It consists of a clear plastic mask with 21×21 0.5×0.5 mm^2 square scintillator pixels with a pitch of 2 mm. The scintillation light is collected by the mask and detected by a photomultiplier tube. A coincidence

measurement of the PSP and of its pixel detector provides a projection of the pixel layout on the PSP, which is distorted before calibration. A map can then be established using a cluster-finding algorithm, in order to make the positions of the pixels match.

3.3.3 The CsI Gamma Detector

The gamma detector used in the present experiment is composed of 144 CsI(Na) crystals arranged in a barrel geometry, as seen in figure 3.6. There are 12 azimuthal segments with 12 crystals each, segmented according to the polar angle. Since not only electromagnetic excitation was performed during the nickel experiment, but also quasifree scattering, a plastic-scintillator detector was introduced between the beam pipe and the CsI crystals in order to detect protons. This detector is an assembly of 12 scintillator strips running through the entire length of the CsI, with the strip width matching the width of the azimuthal segments of the gamma detector. When only gammas should be detected in the CsI detector, the plastic scintillator detector is used as a veto detector to discriminate gammas from charged particles. If a neutron is, however, knocked out of the nucleus in a quasifree reaction, the plastic detector will not register it, but the CsI detector will record a high-energy entry. In order to exclude such neutron hits, the high-energy values are identified on an event-by-event basis and ignored by the present analysis.

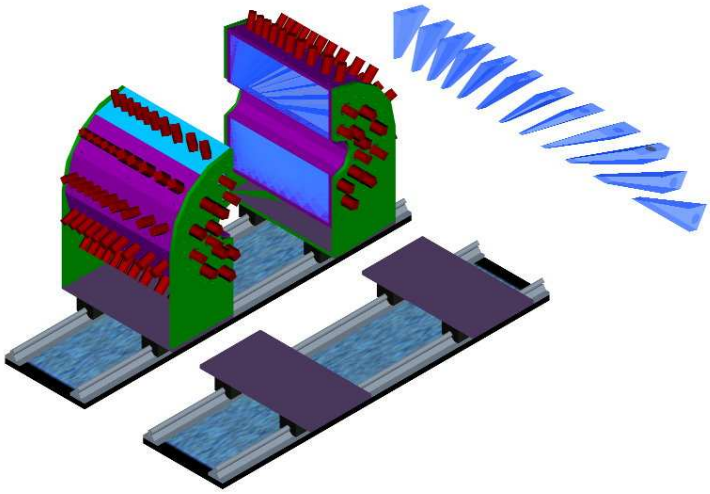

Figure 3.6: View of the opened CsI gamma detector [50].

3.3.4 The Large Area Neutron Detector LAND

The Large Area Neutron Detector (LAND) is a high-efficiency neutron time-of-flight detector designed for neutrons with energies ranging from 100 to 1000 MeV [51]. LAND is placed at approximately 14.6 m behind the target at an angle of 0° and is composed of

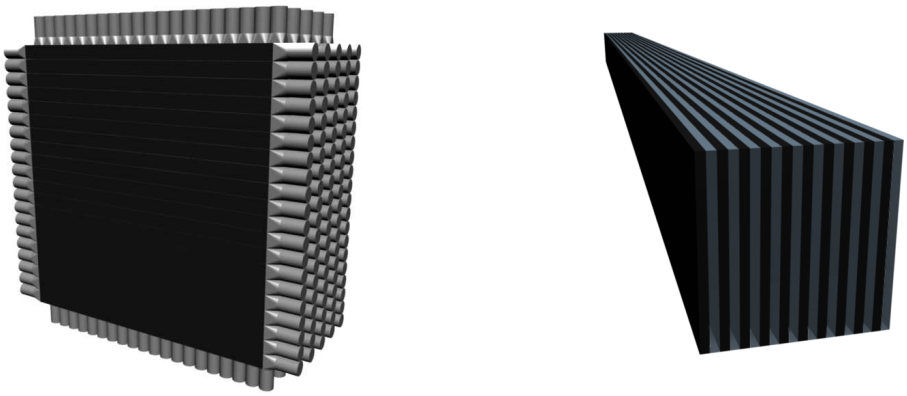

Figure 3.7: Left: view of the Large Area Neutron Detector LAND. Right: LAND scintillator paddle. Each sheet of 5 mm thick plastic scintillator is preceded by a 5 mm thick sheet of iron converter.

200 so-called paddles with a section of 10×10 cm^2 and 2 m long. Each paddle is a stack of 10×5 mm thick iron sheets, each of which is followed by a 5 mm thick plastic-scintillator sheet. The iron layers convert the high-energy neutrons to charged particles, which can be detected subsequently in the following scintillator. Each paddle is read out by two photomultiplier tubes placed at the ends of the paddles. Twenty paddles are assembled into a 2×2 m^2 plane perpendicular to the beam axis. Ten such planes are then stacked to provide a 1 m deep detector. The planes alternate vertical and horizontal paddles in order to increase the position resolution of the detector. When a paddle is hit, the position along the paddle is provided by the time difference of the signals measured by the two PM tubes, while the other two positions are defined by the absolute position of the paddle in the detector.

Since each neutron usually generates several hits in LAND, all 400 channels must be synchronized in time and energy, such that the hits in various paddles can be compared with each other. The optimally working LAND presents a time resolution of $\sigma_t \approx 250$ ps. If more than one neutron interacts with LAND, the hits of the different neutrons must be separated: a special algorithm attributes the various hits to the different neutrons by using time, position and angular arguments. The calibration of all 400 channels will be discussed in more detail in chapter 4.

3.3.5 The Large-area Scintillating Fiber Detector GFI

The large-area scintillating fiber (GFI) detectors [52, 53] provide horizontal position measurements with a high precision. Each detector consists of 475 scintillation fibers with a length of 50 cm and 1 mm wide. One end of the fibers is coupled to a position-sensitive photomultiplier tube, while the other is read out by a conventional PM tube for

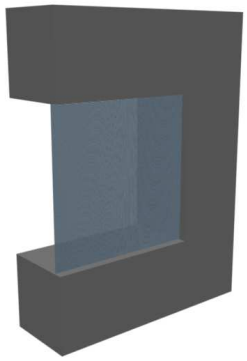

Figure 3.8: The scintillating fiber detector GFI.

timing and energy measurements. In the nickel experiment, only the position information was used. As long as the position resolution of the position-sensitive photomultiplier is better than the fiber width, which is fulfilled for heavy ions in the mass region of the present experiment, the position resolution of the GFI detector corresponds to the fiber pitch of 1 mm.

The GFI calibration relies on a similar algorithm as the PSP detectors. Each fiber is attached to a mask coupled to the position-sensitive PM tube. The horizontal position is then obtained *via* a coordinate system transformation. This requires the calibration of the PM tube using a so-called sweep run, during which the ion beam is swept over the various detectors of the fragment branch by varying the magnetic field of ALADIN. The position of each fiber can then be determined with a cluster-finding algorithm in order to establish the complete mapping of the fiber mask, which is used for the coordinate transformation.

3.3.6 The Time-of-Flight Wall TFW

The last detector of the fragment branch is the time-of-flight wall (TFW), shown in figure 3.9. The modular design comprises 18 horizontal and 14 vertical plastic scintillating paddles, both 10 cm wide and 0.5 cm thick, and read out by photomultiplier tubes at both ends. The position of the ions along the paddles is again provided by the time difference measured by the PM tubes. However, the position resolution is inferior to that of the GFI detectors, and therefore cannot contribute to the fragment tracking. The main purpose of this detector is to provide time and energy-loss measurements. The energy loss is used for the charge identification of the fragments, allowing charge correlations to be established using also information from the third PSP detector, which will be described in chapter 5.

The calibration of the TFW is closely related to that of LAND: all channels must be

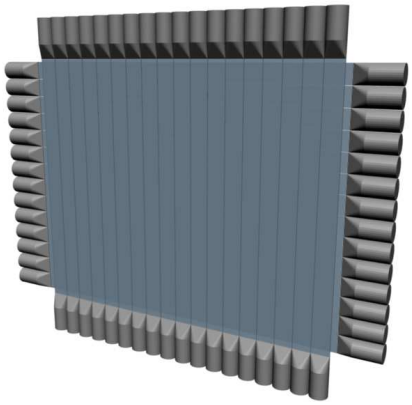

Figure 3.9: The time-of-flight wall TFW.

synchronized in time and energy before use. This can be achieved by using the sweep run, as in the case of the GFI detectors (subsection 3.3.5). The sweep run, however, is performed without any reaction target, and therefore the beam is constrained to a narrow vertical range. The synchronization of the channels far from the center of the detector is more reliable if a run with a thick reaction target is used, due to the angular straggling. The general calibration procedure will be described in chapter 4 along with the LAND calibration.

3.4 R^3B Setup at the Future FAIR Facility

3.4.1 General Properties of the R^3B Setup

The R^3B setup (Reactions with Relativistic Radioactive Beams) at the future FAIR facility can be considered as an upgrade of the existing LAND setup at Cave C. The planned FAIR accelerator layout can be seen in figure 3.1, where all future facilities are drawn in red. The current GSI accelerators will be upgraded to handle higher beam intensities in order to be used as injectors for FAIR. One of the main new features will be the SIS 100/300, a double heavy-ion synchrotron capable of accelerating, *e.g.*, $^{238}U^{92+}$ up to 34 AGeV [54]. When U^{28+} ions are accelerated instead of U^{92+} ions, the maximum intensity that can be obtained due to the space-charge limit is increased by approximately one order of magnitude, which, however, requires the use of stronger magnetic fields. The production of secondary beams does not require such high energies, but the higher intensities will be beneficial for the investigation of even more exotic nuclei. The Super-FRS will produce the exotic beams with magnetic rigidities of up to 20 Tm [55], providing beam energies up to 1 GeV per nucleon [54], which can be directed into the R^3B setup, besides various other experiments and storage rings.

Figure 3.10 presents the schematic layout of the R^3B setup. As for the present LAND

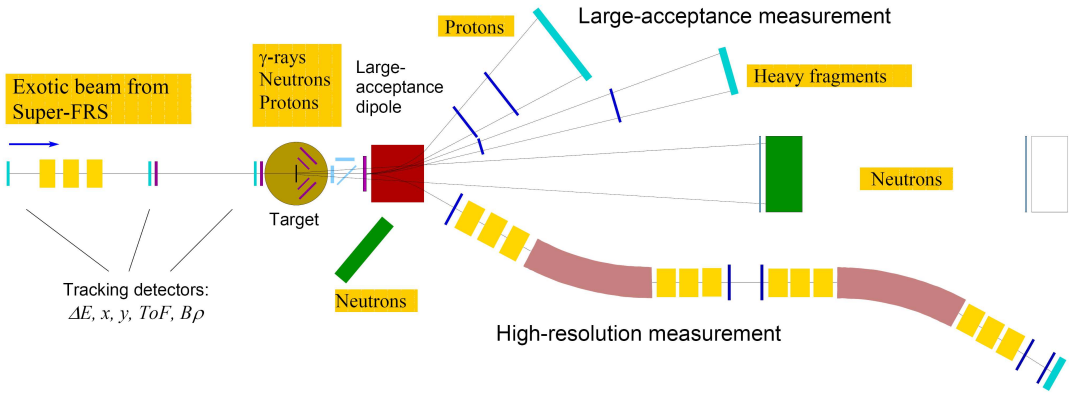

Figure 3.10: The R^{3}B setup at FAIR. Figure from the R^{3}B technical proposal [55].

setup, the incoming beam will be tracked up to the target, which will be surrounded by a 4π gamma calorimeter. A new superconducting dipole magnet, capable of handling the high beam energies, will be used to deviate the charged fragments into two branches: the heavy fragment and the proton branches. The fragment branch will be implemented with a new TOF wall based on Resistive Plate Chambers (RPC), a detector category which will be described in more detail in the following subsections. The proton branch will track protons with gas-filled drift chambers, which are already in use at Cave C for the more recent LAND experiments. For the neutron detection, a new detector - NeuLAND - will be built. Instead of using scintillator material, RPCs will be used here also. A second neutron detector for slower neutrons will be installed at an angle close to 45° with respect to the incoming beam for the investigation of, *e.g.*, charge-exchange reactions. One of the major implementations with respect to the existing LAND setup is the high-resolution magnetic spectrometer intended for precision mass measurements, used for instance for knock-out and quasi-free scattering reactions.

In the following subsections, the NeuLAND detector will be presented in more detail, as well as results of one of the first test experiments.

3.4.2 NeuLAND

The design goals of NeuLAND have been chosen to match the momentum resolution of the charged fragments of $\Delta p/p \approx 10^{-3}$ [55]. This constrains the time and position resolutions of the new detector to $\sigma_t < 100$ ps and $\sigma_{x,y,z} \approx 1$ cm, which is approximately one third of the respective quantities of the existing LAND detector. The active area seen by the neutrons will remain at 2×2 m^2, since this will match the ±80 mrad of the aperture of the dipole magnet if NeuLAND is placed at a distance of 12.5 m from the target. The depth of the detector will also remain approximately the same, since

it is mainly determined by the neutron interaction length of the converter material. These detector variables will allow an invariant-mass resolution of 10 keV at 200 keV above the neutron threshold for a medium-mass nucleus with an incoming energy of 500 AMeV, when the detector is located the farthest from the target (approximately 35 m). NeuLAND should also be capable of detecting up to 5 neutrons per event and reconstruct their momenta correctly [55].

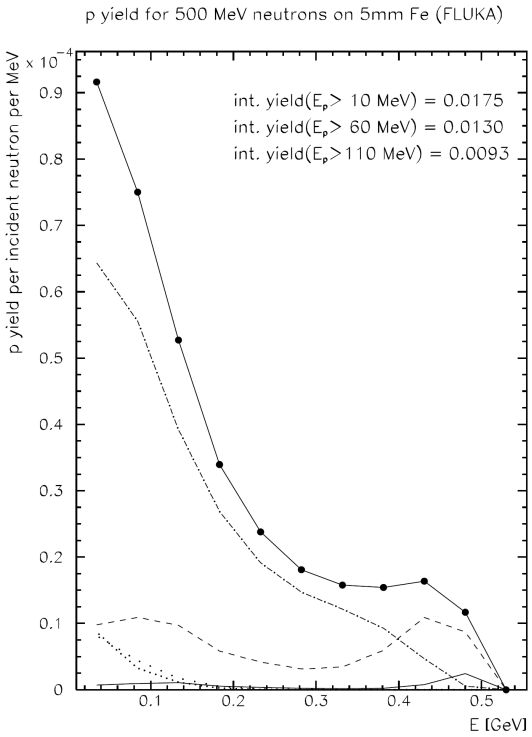

Figure 3.11: Proton yield per incident 500 MeV neutron on 5 mm Fe. Solid line with dots: total proton yield. Other lines: proton yield for the 0-5° (solid line), 5-20° (dashed line), 20-80° (dashed-dotted line), 80-120° (dotted line) and 120-180° (densely dotted line) angular ranges. Figure from the R^3B technical proposal [55].

The design of the new detector relies on the properties of the neutron conversion. As in LAND, iron will be chosen as passive converter material for NeuLAND, since it offers an attractive density-to-cost ratio. A FLUKA calculation shows in figure 3.11 the energy distribution of the generated protons for an impinging neutron at 500 MeV [55]. As the distribution peaks at low energies, the new detector will primarily be required to present good time and position resolutions in this region. Also, the 20-80° range dominates the distribution, which also must be taken into account, since large angles can ruin the position resolution in thick detectors.

There are two major detector concepts for NeuLAND, based on scintillation material or on Resistive Plate Chambers (RPC). The high granularity of NeuLAND requires a

large number of read-out channels: the cost for fast photomultiplier tubes is one of the main drawbacks for the scintillator solution. The RPC concept is very attractive from the cost point of view, since this type of detector is based on common materials, lowering the cost per channel. These detectors are used for the detection of charged particles, most often minimum ionizing, meaning that a serious effort in R&D is required in order to detect high-energy neutrons. In the following subsections, the RPC detector principle is described, as well as a first test experiment, in which existing RPC detectors have been tested with a proton beam in the low-energy range of figure 3.11.

3.4.3 Resistive Plate Chamber Detectors

Resistive Plate Chambers (RPC) are gas-filled detectors usually used for the detection of charged particles. The RPC has been introduced in 1981 by Santonico and Cardarelli [56] and proposed as a less complex variant of the Pestov counter [57]. The initial concept was simple: the RPC consists of two parallel electrode plates with counter gas flowing at atmospheric pressure between them. At least one of the electrodes must be made of a material with a high bulk resistivity. In this early RPC design, two Bakelite electrodes were used, with a bulk resistivity of 10^{10}-10^{11} Ω cm. The counter gas was a 1:1 (v/v) mixture of argon and butane. Argon is an inexpensive gas often used in proportional counters due to its low electron affinity [58], which is of high importance in electron avalanche detectors. The butane acts as quench gas responsible of absorbing UV photons generated by the relaxation of Ar atoms. Ultraviolet photons can produce ionization of the gas far from the initial interaction vertex, which causes a loss in position resolution and proportionality. Copper foil was placed on one of the Bakelite plates (on the side not facing the gas volume) and was connected to ground. High voltage was applied to the other plate *via* a thin sheet of conducting paper. Copper strips were apposed above the HV electrode to extract a usable electric signal. The high surface resistivity of the HV electrode makes it transparent to electric pulses generated by the electrode avalanche in the gas gap [59, 60]. This allows the signal to be efficiently decoupled from the HV. Also, since the HV in the gas gap is carried electrostatically by the Bakelite plates, the amount of current flowing in the gap is small and therefore does not lead to a voltage break-down of a large portion of the detector. This first RPC showed a time resolution of approximately 1 ns and 97% efficiency at an operating voltage of 10 kV.

Over the years, the RPC design and operation parameters have greatly evolved with the optimization of the detector attributes for various uses. The gas gaps have become smaller, leading to an increased number of gaps in order not to lose efficiency. Also, glass plates are widely used as resistive material instead of Bakelite, which is due to the increased stiffness of glass and its superior surface quality. The gas mixture has evolved as well: the first RPC of Santonico and Cardarelli did not require the use of amplifiers to process the electronic signals, since the detector was operated in the so-

called streamer mode, which involves the discharge of a relatively large region of the detector, generating large signals. Several actual experiments run RPCs in the streamer mode, such as BELLE at KEK[‡] and BABAR at SLAC[§]. The streamer mode simplifies the read-out electronics, but is severely limited by the rate capacity of approximately 1 Hz/cm^2.

In presence of higher rates, the RPC must be operated in the so-called avalanche mode [61], involving smaller currents and therefore a smaller blind zone after a signal has been generated. Since the strength of the electric field cannot simply be reduced to prevent the formation of streamers without destroying the detection efficiency and time resolution, the gas mixture must be modified. Attempts to operate the RPC in the avalanche mode have been carried out with various compositions of halogenated carbon compounds such as CCl_2F_2 (Freon-12) [61], CF_3Br (Freon-13B1) [62], CH_2F_4 (Reclin-134a) [63, 64] or CHF_5 (HFC-125) [65]. A small proportion of SF_6 also suppresses streamers [66] and extends the efficiency plateau on the high-field side. A standard gas mixture of 85% Reclin-134a + 5% isobutane + 10% SF_6 is currently used in most detector systems [64]. Some attempts have been made to change the gas mixture by using CO_2 instead of SF_6 and isobutane, or by removing the isobutane from the mixture, at the expense of time resolution and efficiency [65]. The use of gases with a significant global warming potential, such as SF_6 and Reclin-134a, introduce further constraints on the release of the counter gas to the atmosphere. A possible design of a recycling unit for the RPC gas mixture is discussed in appendix C.

The avalanche-mode RPCs can be furthermore subdivided into two categories: trigger and timing RPCs. The latter have more strict conditions on the mechanical homogeneity than the former, since the time resolution strongly depends on the gas gap size [64]. Small fluctuations in the gap size can generate position-dependent time resolution effects, which ruin the overall resolution. Avalanche-mode trigger RPCs are used in high-energy physics experiments such as ATLAS and CMS at the LHC[¶], while timing RPCs can be found in HARP at CERN[‖] or in ALICE at the LHC, or in FOPI and HADES at GSI. Generally speaking, RPC detectors can only measure time. The charge of an event is usually defined only by the detector properties, mainly by the electric field strength. This is due to the electron avalanche process: when an electron-ion pair is created by the passage of an ionizing particle or by a photon, the electron is accelerated towards the anode. On the way it collides with the various gas species, where more electrons are knocked-out. The amplification continues until the electric field created by the RPC electrodes is screened strongly enough by the electron cloud, which occurs at the

[‡]KEK High Energy Accelerator Research Organization, Tsukuba, Japan

[§]SLAC National Accelerator Laboratory, previously known as Stanford Linear Accelerator Center, Menlo Park, CA, USA

[¶]Large Hadron Collider, CERN, Geneva, Switzerland

[‖]Organisation Européenne de la Recherche Nucléaire, Geneva, Switzerland

so-called space charge limit. This limit is reached relatively quickly at quasi-atmospheric gas pressures.

The design constraints defined for NeuLAND in subsection 3.4.2 require excellent timing properties as well as a high detection efficiency. The detector concept therefore relies on multi-gap timing RPCs, as can be seen in the prototype design in figure 3.12. A 2×4-gap RPC prototype is planned with read-out electrodes of approximately 2.4 cm width. The modules should finally measure 2×0.5 m^2, allowing four such modules to be assembled into one plane. Since the prototype testing is under way, all detector variables are subject to change. In most experiments, the detectors are required to be almost transparent to the particles they measure. For NeuLAND, a massive passive converter is required for the production of a hadronic shower by relativistic neutrons. The inner and outer read-out electrodes are therefore planned with a thickness of 4 and 2 mm, respectively. The glass plates lie on a network of fishing line, defining the width of the gas gap. The outermost glass plates are coated on the side opposite to the gas gaps with a graphite layer onto which the high voltage is applied. This layer is isolated from the read-out electrodes by Kapton film. A differential read-out of the electrodes is planned, in order to improve the signal quality. The cross-talk between neighboring electrodes is an important issue since inactive detector volumes are minimized: the electrode strips are glued together, yielding a spacing of a few hundred microns.

Several RPC modules will be stacked together and inserted into gas-tight envelopes. Since the electronics and supporting structures will need to be located at the short edges of the individual modules in order to create a continuous active layer, the gas gap spacers must run along the length of the RPC. The gas quality must be homogeneous throughout the entire detector, indicating that the detector gas must be pumped through the gaps, since diffusion will exchange gas volumes much slower in the center of the detector than near the edges.

RPC prototypes for NeuLAND have already been produced and tested under various conditions, in order to choose a final concept for the detector. The following subsection

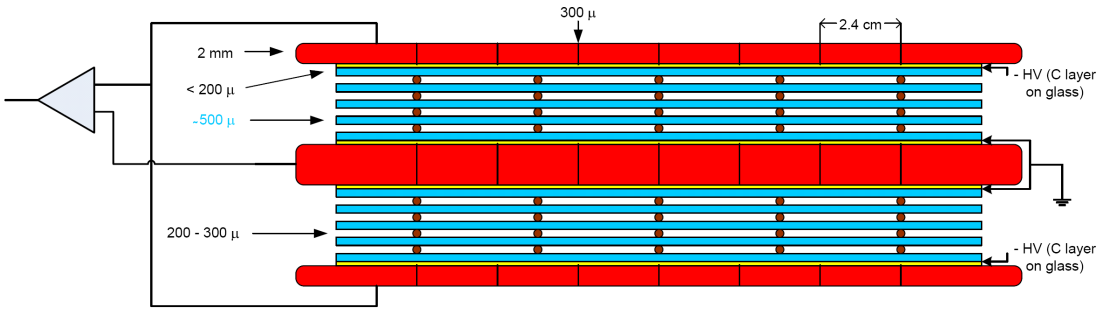

Figure 3.12: One of the investigated RPC concepts for NeuLAND.

will present results from the KVI test experiment, where two RPC prototypes designed for other detector systems have been tested with low-energy proton beams.

3.4.4 RPC Test Experiment at KVI

The previous subsections have shown on one hand that relativistic neutrons produce primarily low-energy protons when interacting with Fe nuclei, and on the other that Resistive Plate Chamber (RPC) detectors have been developed for the detection of minimum ionizing particles. Since NeuLAND shall be based on RPCs, their response to non-minimum-ionizing protons must be proven to provide sufficient time resolution and efficiency. A test experiment with RPC prototypes has been carried out for this reason with proton beams at various energies at the Kernfysisch Versneller Instituut (KVI) at the University of Groningen in the Netherlands.

The first RPC prototype of the test experiment was provided by the FOPI collaboration and is a 900×46 mm^2 RPC of the production series [67, 68]. The design of the detector is shown in figure 3.13, although the production series RPC consists of 2×4 gas gaps of 300 μm width. Copper foils are apposed on the outermost glass plates to supply the high voltage. A typical operating voltage for this RPC was -9.5 kV, although tests with various voltages ranging from -8.6 kV to -9.7 kV have been carried out. A 16-strip read-out anode was placed in the middle of the detector with a pitch of 1.94 mm and a gap width of 0.6 mm. The electronic signals were pre-processed by a specially designed pre-amplifier, which generates an amplified analog signal as well as a logical signal. This information was then sent to the data-acquisition system.

The second RPC tested at KVI is a prototype from LIP in Coimbra, Portugal. Unlike the FOPI RPC, this detector has structureless read-out electrodes [69], as can be seen in figure 3.14. The RPC is 60 cm long, 2 cm wide and 1.12 cm high, with 2×2×300 μm gas gaps. The HV aluminum electrodes are in contact with the gas volume, and the resistivity is carried by only one glass plate placed between them. The central electrode is supplied with a typical positive voltage of 6.25 kV. Here also, the voltage has been varied from 5.5 kV to 6.5 kV for testing purposes. The anode is read out with respect to the outer cathodes (ground) *via* a capacitance. The electronic signals are treated with the FOPI pre-amplifiers before being sent to the data-acquisition system. The results recorded with this RPC are not optimal since the designated front-end electronics were not available.

The test experiment was performed at the irradiation station of the AGOR cyclotron facility at KVI. A picture of the setup is shown in figure 3.15. Proton beams at 190 and 85 MeV were delivered to the cave and passed through a collimator before reaching the detectors. A $\varnothing = 5$ mm collimator was used during most of the test. Protons at 120 MeV and at energies between 26 and 72 MeV were generated in the experimental area by inserting degrader material into the 190 and 85 MeV beams, respectively. In

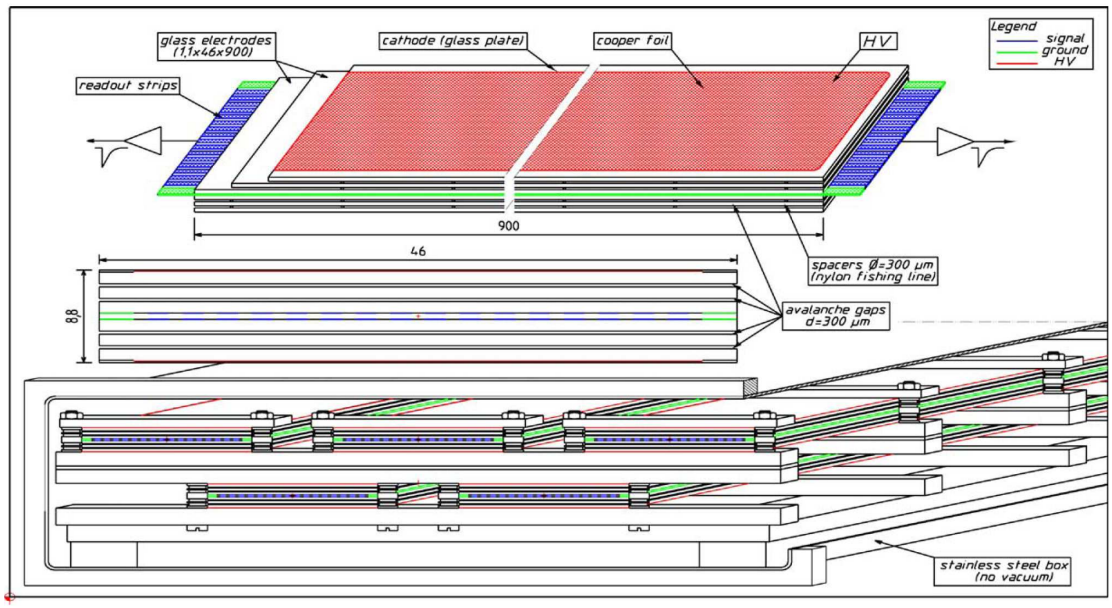

Figure 3.13: Schematic drawing of the FOPI RPC. The bottom inlay shows the assembly of FOPI RPC subunits in the gas box. From A. Schüttauf [67].

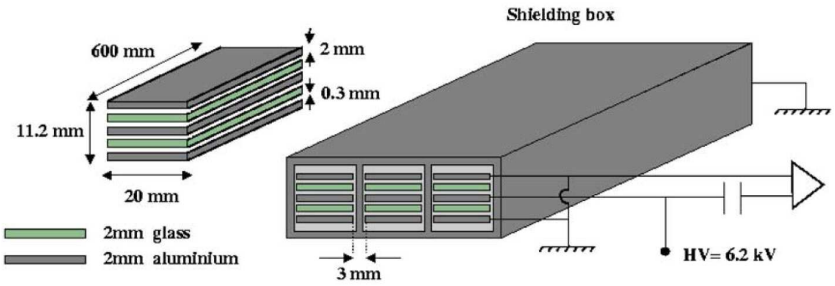

Figure 3.14: Schematic drawing of the LIP Coimbra RPC. From Alvarez-Pol *et al.* [69].

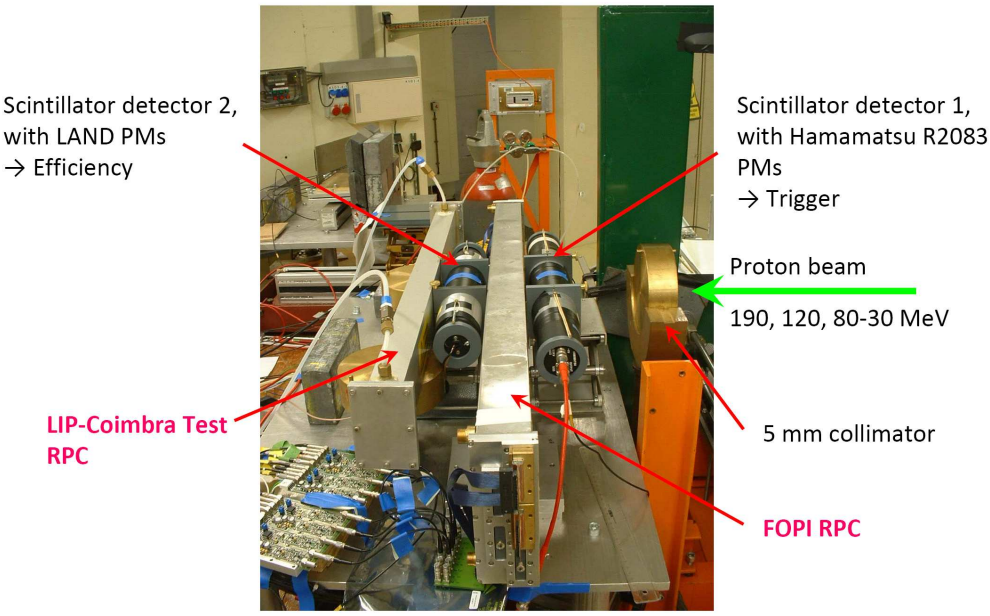

Figure 3.15: Picture of the RPC test-experiment setup at KVI.

most measurements, the proton rate varied from 100 to 200 counts per second. With the 5 mm beam collimator, this leads to a unit-surface rate of approximately 500 to 1000 Hz/cm^2, which is three orders of magnitude higher than expected for NeuLAND.

Figure 3.15 shows the standard configuration of the test: the beam first passes through a plastic scintillator viewed by two Hamamatsu R2083 photomultiplier tubes, which generate the trigger. The protons then pass through the FOPI RPC before entering a second scintillation detector, equipped with two Photonis XP2262 PM tubes for efficiency measurements. The LIP RPC was usually placed behind the other detectors, in order to profit from the beam time. For timing measurements with LIP detector, however, the positions of the two RPCs were exchanged. The RPCs were both supplied in series with the standard gas mixture of 85/10/5 Reclin-134a/SF_6/i-Butane.

The analysis details of the KVI test experiment are discussed in appendix B. The time resolution of the RPCs is measured by considering the time-of-flight between the S1 scintillator and the RPC. The mean time has been used for the individual detectors, since this removes the position dependence of the time signal. The resulting time distribution is then fit by a Gaussian function which directly provides the σ time resolution. If the observed time resolution is obtained from the flight time of the protons between the S1 scintillator and the RPC, the total time resolution is the quadratic sum of all time resolution values of the various detectors:

$$\sigma^2_{TOF} = \sigma^2_{S1,L} + \sigma^2_{S1,R} + \sigma^2_{RPC,L} + \sigma^2_{RPC,R} \tag{3.2}$$

RPC	E_p [MeV]	σ_t^{S1} [ch]	σ_t^{S1RPC} [ch]	σ_t^{RPC} [ch]	σ_t^{RPC} [ps]
FOPI	120	0.93	1.46	1.13	45.2
FOPI	38	1.04	1.81	1.48	59.2
FOPI	29	1.20	3.60	3.39	136
LIP	120	0.93	2.47	2.29	91.6
LIP	48	1.65	2.26	1.54	61.6

Table 3.1: Time resolution results σ_t for the FOPI and LIP RPCs at various proton energies. The 120 MeV data was recorded with the LIP RPC in the rear position, which affects the time resolution. For the time resolutions given in ps, a TDC gain of 40 ps/channel is used. S1 labels the time resolution of the trigger scintillator detector located in front of the RPCs, while S1RPC labels the combined RPC and S1 time resolution.

where L and R label the time resolution values of the left and right sides of the S1 and RPC detectors, respectively. Since the time resolution of the detector is equal to the quadratically added time resolutions of its basic subunit structure (in this case, an RPC strip) at its best, the subunit time resolutions for the S1 scintillator and for the RPC are defined as:

$$\begin{aligned} \sigma_{S1}^2 &= \sigma_{S1,L}^2 + \sigma_{S1,R}^2 = 2\sigma_{S1,L}^2 \\ \sigma_{RPC}^2 &= \sigma_{RPC,L}^2 + \sigma_{RPC,R}^2 = 2\sigma_{RPC,L}^2 \end{aligned} \tag{3.3}$$

if the time resolutions of both ends of the subunit are equal. Considering the time resolutions in expression (3.3), the RPC time resolution can be extracted from equation (3.2):

$$\sigma_{RPC} = \sqrt{\sigma_{TOF}^2 - \sigma_{S1}^2} \tag{3.4}$$

with the total measured time resolution σ_{TOF} and the time resolution of the first scintillator σ_{S1}.

The efficiency measurement only provides approximate results due to the fact that the experimental setup was not optimal for such measurements. The values for the FOPI RPC are therefore much too small, while the LIP efficiency is located between 90 and 100%, depending on the voltage applied. The number of events observed in a given FOPI RPC strip was compared to the number of protons seen in S2, knowing that in both cases the proton was observed in S1, since this detector generates the trigger. The large size of the S1 and S2 scintillators with respect to the RPC strip width would allow protons to be registered in S1 and S2 without passing through the strip, resulting in a too low efficiency. A valid efficiency measurement would require the reference detectors to be smaller than the strip width, such that a proton registered in both scintillators

would necessarily pass through the RPC. The measurement performed with the LIP RPC fulfills this requirement, therefore providing a more realistic result.

Chapter 4

Detector Calibration

4.1 Data Calibration Levels

The various detectors used in the present experiment generate analog signals that are digitized and stored in an event-wise manner. The collected information is most often a time measurement with respect to the trigger (given by the TDC modules) and a charge or amplitude measurement (from QDC or ADC modules, respectively). The data file consists of a list of events with the corresponding data, which must be extracted for further use. This process, called unpacking, relies on the `land02` software package written by H. Johansson. Not only does the program convert the data into a user-specified format, but it also performs the necessary calibration for the subsequent analysis. The full calibration of a detector is subdivided into several steps, which are described below:

RAW Level

The RAW level provides the access to the data exactly as it has been stored. No calibration is applied, and all values are given in channel units. The unpacker simply links a physical detector, *e.g.*, photomultiplier tube, with the electronic channels of the data-acquisition system. This data level can be used to easily check the status of a given detector.

TCAL Level

The TCAL level converts time information from TDC channel numbers to time units (usually nanoseconds), and subtracts the pedestal value from the measured energy values. The necessary parameters are calculated using the `tcal` and `clock` routines of `land02`, which require data recorded during the experiment using dedicated triggers. The extraction of the parameters will be shortly described in subsections 4.2.2 and 4.2.3.

SYNC Level

Up to now, each electronic channel has been treated individually, ignoring all other information sources of other possible subunits of the same detector. In order to consider such a detector as one entity, all its channels must be synchronized with respect to each other. The calibration method depends strongly on the type of detector, *e.g.*, cosmic rays are used for LAND, heavy ions for the TFW and gamma sources for the CsI array. After the synchronization of the time and energy values, the data of the various subunits can be compared and combined.

DHIT Level

The DHIT level, or detector-hit level, combines the time and energy information from the SYNC level according to the detector geometry. This provides, *e.g.*, the position, mean time and energy loss of a hit in detector-internal coordinates. In detectors such as the PSPs and the GFIs, the DHIT level provides position data in the so-called (u,v) coordinate system, which is defined by the read-out method.

HIT Level

In order to use the data for further analysis, it must be converted to lab frame coordinates. This is achieved using the detector-geometry information when passing from the DHIT to the HIT level. In the case of the PSP and GFI detectors, the HIT-level-position data in the (x,y) coordinate system is obtained by performing a detector-specific transformation on the (u,v) data. Although the data is provided in a common coordinate system in this data level, the geometry of the entire setup must still be defined, which will be carried out in the following level.

TRACK Level

The TRACK level combines information of various detectors, in order to express kinematic event variables. This requires mainly the experimental setup geometry (*e.g.*, distances, angles) as input. A first interpretation of the LAND data is also performed on the TRACK level. Since relativistic neutrons usually generate several hits in LAND, these are analyzed by a specially designed algorithm, which sorts the LAND hits into common neutron hits, for which the angles and velocities are stored. The routine identifies the neutron hits according to various criteria, such as the interaction time and position, the neutron multiplicity, and for multiplicities larger than one, the relative positions of the various neutrons. The algorithm misidentifies a certain percentage of neutron hits and therefore introduces artifacts that will be treated in the investigation of the detector response in section 4.5.

Beyond `land02`

The TRACK-level data provided by the `land02` framework provides the basic variable required for the extraction of the physically relevant data. Based on this level, more advanced and experiment-specific routines will take over. In the present case, the first step beyond `land02` consists in tracking the charged fragments through the magnetic field of ALADIN, in order to identify their mass (*cf.* section 4.4). This information is required to create appropriate conditions on the data set for the extraction of the Coulomb excitation energy distribution (*cf.* chapter 5).

4.2 Scintillator-based Detectors

4.2.1 Basic Principles

Most of the detectors presented in the previous chapter are scintillation detectors read out by one or several photomultiplier (PM) tubes. Each electronic channel is able to provide time and energy information, although both types of information are not always required. If a scintillation detector is read out by more than one PM tube, position information can also be provided by measuring time differences or energy ratios between the tubes. In a detector with several scintillation sub-units, having several PM tubes each, all electronic channels must be synchronized in order for the entire detector to work as a homogeneous entity. Most of the more complex detectors used in the LAND setup are based on scintillation "paddle" sub-units, as shown in figure 4.2.1. Considering the two PM tubes located at the left and right ends of the paddle, the measured times

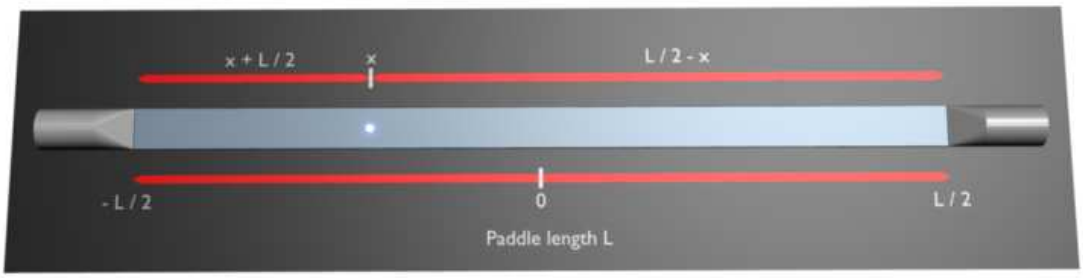

Figure 4.1: Typical scintillator paddle.

and energies are expressed in the following manner [70]:

$$\begin{aligned} t_L &= \frac{1}{v_{eff}}\left(x + \frac{L}{2}\right) + T \\ t_R &= \frac{1}{v_{eff}}\left(\frac{L}{2} - x\right) + T \\ e_L &= E\exp\left[-\frac{\left(x + \frac{L}{2}\right)}{\lambda}\right] \\ e_R &= E\exp\left[-\frac{\left(\frac{L}{2} - x\right)}{\lambda}\right] \end{aligned} \tag{4.1}$$

where v_{eff} is the effective light velocity in the scintillation material, L is the length of the paddle, x is the position of the interaction in the paddle, T is the time of the interaction, E is proportional to the deposited energy at the interaction point, and λ is the light-attenuation length of the scintillator material. A fraction of the deposited energy is withdrawn in the electronics chain, in order to build the timing signal. Since the measured individual times and energies are position-dependent, the time and energy loss values of the interaction are calculated using both measurements:

$$\begin{aligned} T &= \frac{t_L + t_R}{2} - \frac{L}{2v_{eff}} \\ \ln E &= \frac{\ln e_L + \ln e_R}{2} + \frac{L}{2\lambda} \end{aligned} \tag{4.2}$$

Using (4.1), the position of the interaction can be reconstructed from the measured times or energies:

$$\begin{aligned} x &= v_{eff}\left(\frac{t_L - t_R}{2}\right) \\ x &= \lambda\left(\frac{\ln e_R - \ln e_L}{2}\right) \end{aligned} \tag{4.3}$$

The previous expressions for time, deposited energy and position are correct if the individual times and energies were measured directly at the PM tube. Since the analog signals are processed and digitized in order to be acquired by the DAQ*, cable lengths, signal losses and processing times must be accounted for. Also, the DAQ measures times and energies in channel units, usually ranging from 0 to 4095 (12 bit data words). The measured times of the PM tubes of a detector built of several paddles are calculated as follows:

$$\begin{aligned} t_{L,cal} &= t_{L,raw} \cdot a_{L,ch\to ns}\left(+T_{L,cal}\right) + T_{diff} + T_{sync} \\ t_{R,cal} &= t_{R,raw} \cdot a_{R,ch\to ns}\left(+T_{R,cal}\right) - T_{diff} + T_{sync} \end{aligned} \tag{4.4}$$

*Data AcQuisition system

where $t_{L,cal}$ and $t_{R,cal}$ are the calibrated times (in time units), $t_{L,raw}$ and $t_{R,raw}$ are the raw times (in channels), $a_{L,ch\to ns}$ and $a_{R,ch\to ns}$ are the time-calibration-slope parameters, $T_{L,cal}$ and $T_{R,cal}$ are the time-calibration-offset parameters, T_{diff} is the time difference parameter, and T_{sync} is the time-synchronization parameter. The time-calibration parameters are intrinsic to a portion of the electronics chain. The slope parameter reflects the time-to-digital conversion, being simply the conversion factor of TDC channels to time units (usually nanoseconds). The offset takes into account cable lengths and processing times, and can in most cases be ignored (*i.e.*, set to zero). The time-difference offset synchronizes the two PM tubes of a paddle, such that a hit in the middle of the paddle will give a time difference of zero. The time-difference slope is also obtained from the same procedure and provides the effective velocity of light in the scintillation material. Finally, the time-synchronization offset synchronizes all paddles versus each other. This is achieved by considering a large amount of detector hits, where at least two crossing paddles have recorded a hit. The offset is then adjusted in order to equalize the measured mean times of both paddles. The two last parameters are in principle independent of each other. When calculating the mean time using (4.2) and (4.4), the resulting expression does not depend on T_{diff}, whereas if the position is calculated using (4.3) and (4.4), the result does not depend on T_{sync}.

The treatment of the energies measured in the PM tubes is very similar to the approach used for the times. The energies are expressed by the following expressions:

$$\begin{aligned} e_{L,cal} &= (e_{L,raw} - e_{L,pedestal}) \cdot a_{L,ch\to MeV} \cdot \frac{1}{E_{diff}} \cdot E_{sync} \\ e_{R,cal} &= (e_{R,raw} - e_{R,pedestal}) \cdot a_{R,ch\to MeV} \cdot E_{diff} \cdot E_{sync} \end{aligned} \tag{4.5}$$

where $e_{L,cal}$ and $e_{R,cal}$ are the calibrated energies (in energy units), $e_{L,raw}$ and $e_{R,raw}$ are the raw energies (in channels), $e_{L,pedestal}$ and $e_{R,pedestal}$ are the pedestal values (in channels), $a_{L,ch\to MeV}$ and $a_{R,ch\to MeV}$ are the conversion factors from channels to energy units, E_{diff} and E_{sync} are analogous to T_{diff} and T_{sync}. The pedestal value is the QDC entry for a given channel in the absence of a signal, *i.e.*, the zero of the energy scale for this particular channel. The energy difference and energy synchronization parameters are obtained in a similar way as their time counterparts. Often, the calibrated energies are kept in channel units (*i.e.*, setting $a_{ch\to MeV} = 1$), since absolute energy loss values are rarely used.

In the following subsections, the various calibration steps will be presented for the paddle-based detectors. The calibration of the GFI and PSP detectors will not be presented here, since they have been extensively discussed in the thesis of Stefanos Paschalis [49] and by K. Mahata *et al.* [53]. The first step of the calibration of any detector is the determination of the TDC gain and offset (often not used), as well as the QDC pedestal, in order to work later on with time units and effective charge units, respectively.

4.2.2 Calibration of the TDC Gain

The TDC modules used in the present experiment have a nominal gain value, which is in most cases 50 picoseconds per channel. The actual gain value can, however, deviate from the nominal value due to various effects, *e.g.*, temperature of the electronics. In order to guarantee an optimal time resolution for all detectors, the TDC gain must be measured at various moments during the experiment. This is achieved by using a so-called time calibrator module, which simply generates two pulses with known time delay, sending the first one to all electronic channels as input, and the second as trigger to the DAQ, since the electronics worked in common-stop mode. With an appropriate trigger, the DAQ records such events during the entire duration of the experiment, enabling the continuous monitoring of the TDC gain, in order to perform off-line corrections to the time information. The plot at the left of figure 4.2 shows a typical distribution of time-

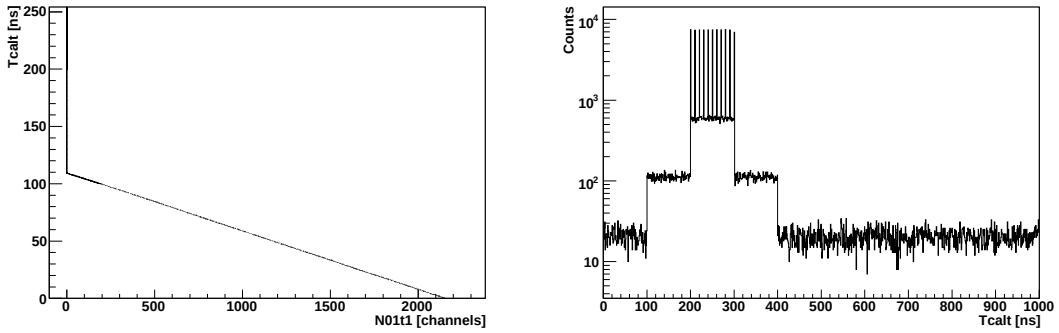

Figure 4.2: Left: typical LAND channel time calibration graph. Right: Time calibrator output distribution.

calibrator data. The time-calibrator data should cover the entire TDC range, in order to extract reliable channel-to-time conversion factors. The plot at the right of figure 4.2 shows the distribution of the output times of the time-calibrator module. It runs in a dual-mode, generating a set of eleven equidistant peaks with high statistics, as well as a continuous distribution over its entire range, with high-, medium-, and low-statistic regions. Using both modes is essential to calibrate all detectors, since they may have very different conversion times. As can be seen in the left plot of figure 4.2, the shown LAND channel receives only a small portion of the medium-statistic region of the time calibrator at the beginning of the TDC range, since all time values beyond 110 ns lie outside of the TDC range and therefore obtain a TDC value of zero.

4.2.3 Calibration of the QDC Pedestal

The goal of the basic calibration of the QDC modules is simply to determine the true origin of the scale, by triggering the electronics with a clock, whenever no signals from the

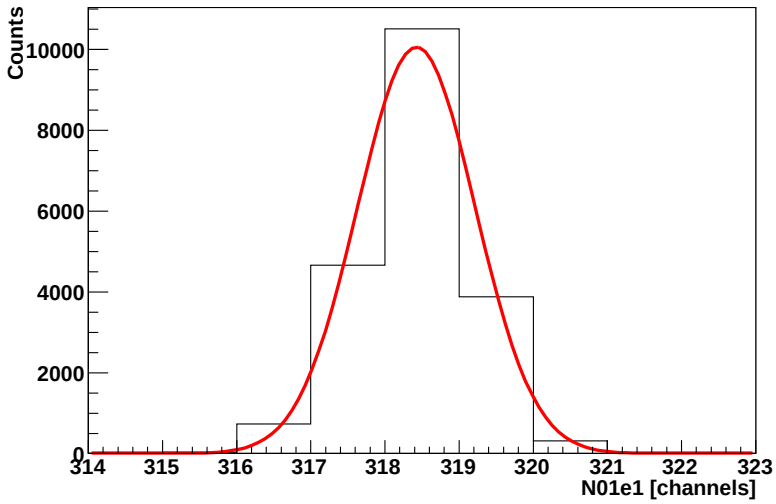

Figure 4.3: Typical LAND pedestal distribution.

detectors are present. The so-called pedestal is a small internal current distributed to all QDC channels ensuring non-negative energy entries. DC-offsets, due to ground loops, can shift the pedestal, while electronic noise increases the width of the distribution. Figure 4.3 shows a typical pedestal distribution for a random LAND channel. In all calibration levels beyond RAW, the mean value of the distribution will systematically be subtracted from the energy entries. The QDC data usually remains in channel units at this point, since energy-loss units require detector input, and depends strongly on the experimental conditions. Therefore, the energy calibration is performed at a later stage, as the subsequent calculation of other calibration parameters (*e.g.*, gain matching) can very well be performed with arbitrary units.

4.2.4 Time and Energy Synchronization

In order to extract quantities such as positions, mean-time and energy-loss values from the data, all channels of a given detector must be synchronized in time and in energy. For detectors based on scintillator paddles, such as LAND, TFW, NTF and the Veto wall, a first synchronization based on the paddle geometry is performed, which only concerns photomultiplier tubes viewing a common paddle. By using the general definition of calibrated times and energies (equations (4.4) and (4.5), respectively), the following expressions will allow the calculation of the T_{diff} and E_{diff} parameters:

$$\begin{aligned} \frac{1}{2}\left(t_{L,cal} - t_{R,cal}\right) &= \frac{1}{2}\left(t_{L,tcal} - t_{R,tcal}\right) + T_{diff} \\ \sqrt{\frac{e_{R,cal}}{e_{L,cal}}} &= \sqrt{\frac{e_{R,tcal}}{e_{L,tcal}}} \cdot E_{diff} \end{aligned} \tag{4.6}$$

with $t_{L/R,tcal} = t_{L/R,raw} \cdot a_{L/R,ch\rightarrow ns} \left(+T_{L/R,cal}\right)$ and $e_{L/R,cal} = \left(e_{L/R,raw} - e_{L/R,pedestal}\right) \cdot a_{L/R,ch\rightarrow MeV}$. The DIFF offset parameter is determined with paddle hits, *e.g.*, cosmic rays for LAND or charged fragments for TFW. For instance, a centrally-hit paddle should provide a value of 0 and 1 on the left-hand side of the time and energy expressions of equation (4.6), respectively, which allows the calculation of the DIFF offset. Figure 4.4

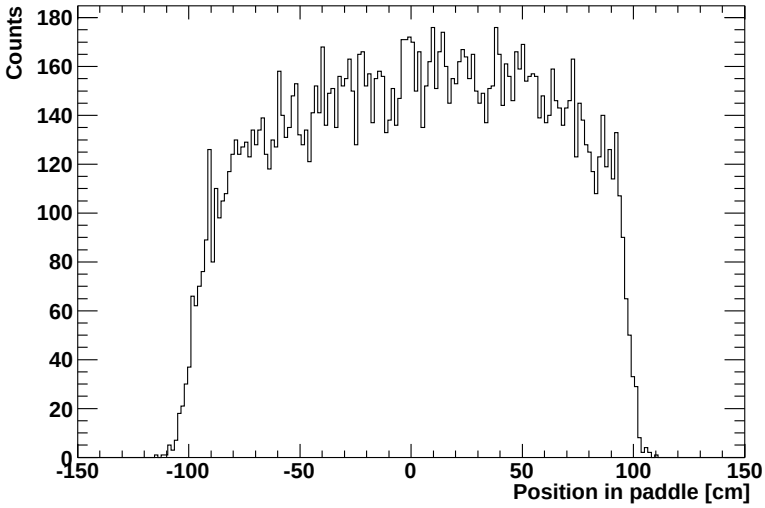

Figure 4.4: LAND cosmic-ray-position distribution.

shows an example of the cosmic-ray-position distribution in a LAND paddle. The T_{diff} parameter has been adjusted such that the center of the position distribution is located at zero. Since the length of the paddles are known, the DIFF values can be obtained by considering the entire distribution, instead of simply shifting the mean value to the expected value. This method also provides the v_{eff} and λ parameters of equation (4.3).

After determining the DIFF calibration parameters, the individual paddles are fully calibrated. The second synchronization step adjusts the times and energies of all paddles of a given detector to a common level. The procedure to extract the SYNC offsets requires hits in crossing paddles, which allows their relative time and energy synchronization. For the T_{sync} offset, the difference of mean times of the two crossing paddles is defined by the distance between the possible interaction vertices in the paddles and by the velocity of the probe (*e.g.*, cosmic rays or heavy ions). In the case of E_{sync}, the energy loss in the crossing paddles is considered to be equal. Based on the general definition of the calibrated times and energies, the following expressions are obtained:

$$\begin{aligned} t^{(1)}_{m,cal} - t^{(2)}_{m,cal} &= t^{(1)}_{m,tcal} - t^{(2)}_{m,tcal} + T^{(1)}_{sync} - T^{(2)}_{sync} = \frac{d}{v} \approx 0 \\ \frac{e^{(1)}_{m,cal}}{e^{(2)}_{m,cal}} &= \frac{e^{(1)}_{m,tcal}}{e^{(2)}_{m,tcal}} \cdot \frac{E^{(1)}_{sync}}{E^{(2)}_{sync}} = 1 \end{aligned} \tag{4.7}$$

where $t_m = \frac{1}{2}(t_L + t_R)$, $e_m = \sqrt{e_L e_R}$, and where $^{(1)}$ and $^{(2)}$ label two crossing paddles. A large amount of data is required to synchronize an entire detector, since all paddle crossings must be analyzed. Each crossing provides an equation similar to (4.7), meaning that the system is massively over-determined. A least-squares minimization will provide a set of optimal SYNC parameters for all paddles of the detector, since they will all be linked. In contrast to the DIFF parameters, the individual SYNC offsets are not unique, since an infinite number of solutions for $T^{(1)}_{sync}$ and $T^{(2)}_{sync}$ exists (also valid for $E^{(1)}_{sync}$ and $E^{(2)}_{sync}$). This allows a common value to be added or subtracted from all SYNC values without modifying the final calibration. This feature is important for the global calibration of all data files of a given experiment, which will be described in subsection 4.2.6.

4.2.5 TRACK-Level Calibrations

Although the detectors are calibrated individually at this point, the physics results depend on measured quantities from different detectors. The time-of-flight of neutrons measured in LAND and of heavy fragments measured in TFW require information on the time of the interaction in the target, which is attributed individually to each incoming ion and is defined by its velocity and by the positions of the various detectors. Since the POS detector defines the start time of all detectors, as well as the T0 (time-on-target), it would be unwise to adjust its time by adding an offset, since this would modify the timing properties of all detectors. Therefore, a global time offset is applied to the entire LAND and to the entire TFW detectors.

The final time calibration of LAND must yield correct velocity values when the time difference between the time in LAND and T0 is measured. The velocity calibration is performed using photons originating from the target. This measurement requires a thick target in order to maximize the interaction probability. Central-collision events are of particular interest, since the number of particles in the outgoing reaction channel is large, accompanied by a large number of photons. The main trigger used to observe photons in LAND is therefore the CsI veto trigger. Each hit in LAND has a mean time and position attributed to it. If the flight time of photons for the effective flight path is subtracted from the measured time-of-flight, a small narrow peak is observed at earlier times than the wide neutron peak, as shown in figure 4.5. The LAND time offset must then be adjusted such that the gamma peak is located at zero. In addition to the global time offset of LAND, the gamma peak can help estimate the time resolution of LAND. In the case depicted in figure 4.5, the gamma peak can be well described by a Gaussian distribution with a width of $\sigma_t = 360$ ps. This value, however, contains a time uncertainty linked to the position of the photon absorption in the paddle, since they are 10 cm thick. The light output of photons in the scintillation material is smaller than in the case of charged particles, which also affects the measured time resolution.

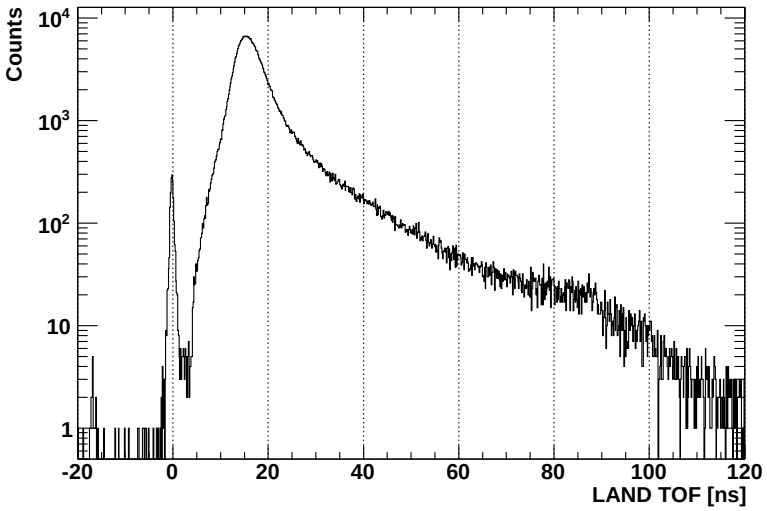

Figure 4.5: TOF spectrum in LAND from a Pb target run, using the CsI veto trigger. The peak at zero nanoseconds is assigned to γ-rays originating from the target.

A similar calibration is performed for the TFW, in order to measure the correct velocity values of the charged fragments. In this case, heavy ions are used instead of photons. The exact velocity is therefore not known, since several layers of material lie between the end of the FRS and the TFW. The time synchronization relies on an energy-loss calculation, performed, *e.g.*, with ATIMA [71]. The time-of-flight between the target and TFW can be calculated by starting at the end of the FRS with the precisely known ion energy and calculating the energy losses in all detectors. This also allows a global energy calibration of various detectors, since ATIMA provides a value in AMeV for each material layer.

4.2.6 Monitoring of Parameter Fluctuations

When data is recorded over long time spans, possible fluctuations of the calibration parameters must be taken into account. These fluctuations can arise through, *e.g.*, electronic noise, temperature variations or detector defects. Just as all channels of a large detector must be synchronized in time and energy in order to treat the detector as one entity, the behavior of the detector must by synchronized over all recorded files of the experiment, in order to compare data of different files. The calibration routines of `land02` link a few files together (in the present experiment, five files were usually linked together) and calculate a set of calibration parameters for this file range. This procedure is repeated for all data files, such that the evolution of the various parameters can be followed in time. Two LAND channels are presented as example in figure 4.6. Most of the channels of a given detector should show a quite stable behavior, such as in LAND

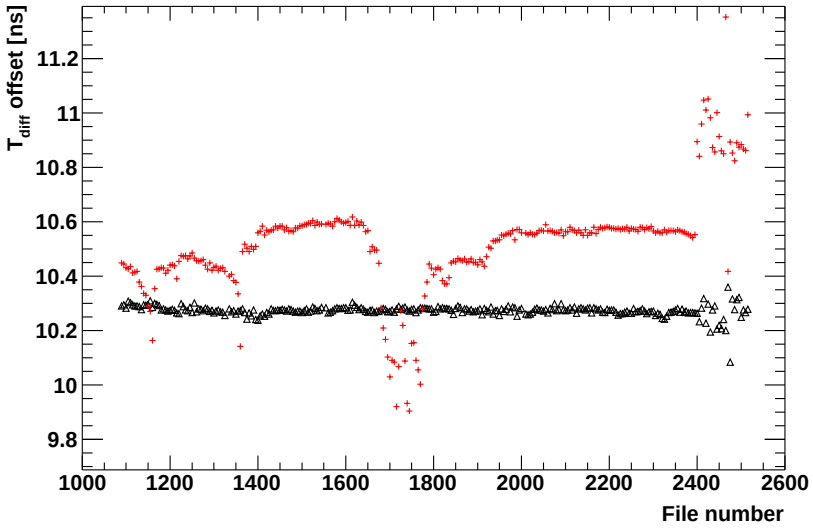

Figure 4.6: Evolution of the LAND T_{diff} offset as a function of data-file number. Data labels: LAND paddle 42 (+), LAND paddle 196 (△). The file-number range of the entire experiment is shown.

paddle 196. The mean value can be used as the global calibration parameter for this channel. For cases where important fluctuations are present, such as in LAND paddle 42, the global parameter will not describe all values properly. Parameter corrections are therefore introduced, which are valid in a given file-number range. The parameter tolerance is an important quantity, since it defines the number of required corrections. Each value is analyzed and compared with the mean value. If the difference is larger than the parameter tolerance, a correction is required. Otherwise, the global parameter value is used. This procedure is applied for all types of calibration parameters.

An additional complication is present in the SYNC offset parameters. As described in subsection 4.2.4, these parameters are not unique, since an arbitrary offset can be added to all the channel values without modifying the synchronization. This arbitrary offset arises from the fact that no particular detector subunit is considered as the reference for all others. The SYNC parameters are therefore bound by the following conditions:

$$\begin{aligned} \sum_{i=1}^{N} T_{sync,i} &= 0 \\ \prod_{i=1}^{N} E_{sync,i} &= 1 \end{aligned} \tag{4.8}$$

where N is the total number of evaluated detector channels. In the present experiment, a reference file was defined, with respect to which all global SYNC shifts will be defined. This fixes the uncertainty on the shift value to a constant value for all files. The global

shift for a file f is therefore calculated with:

$$\begin{aligned} T_{sync}(f) &= T_{sync}(r) + \Delta T_{sync}(f) \\ E_{sync}(f) &= E_{sync}(r) \cdot \Delta E_{sync}(f) \end{aligned} \tag{4.9}$$

where r is the label of the reference file and ΔT_{sync} and ΔE_{sync} are the global shift functions for T_{sync} and E_{sync}, respectively. Figure 4.7 illustrates the procedure for

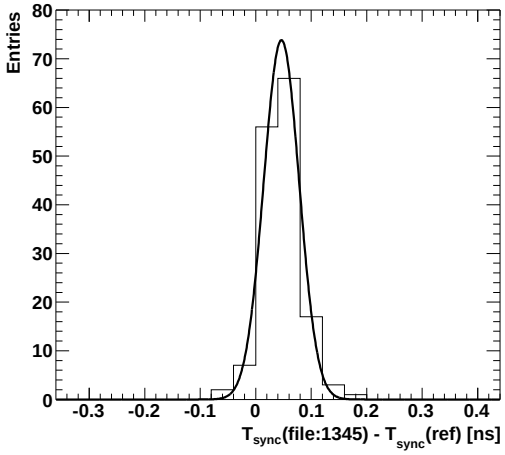

Figure 4.7: Global T_{sync} shift for file 1345 with respect to the reference file.

measuring the global parameter shift for a given file with respect to the reference file. The difference between all SYNC parameters of a given file and the reference file is calculated and inserted into a histogram. The distribution can usually be described by a Gaussian function, of which the mean value defines the common shift. Three LAND paddles have been chosen to illustrate the T_{sync} common-shift subtraction in figure 4.8. The left panel shows the parameters as they are provided by the `cosmic1` calibration routine of the `land02` framework. The right panel shows the same parameter set after the common-shift subtraction. The global T_{sync} parameters of paddles 5 and 6 hardly require corrections, which would not have been the case before the global-shift subtraction. Paddle 42 requires many corrections due to the large-scale fluctuations. The common-shift subtraction has, however, reduced the small fluctuations in the steady regions.

4.2.7 LAND Calibration Issues

During the calibration of LAND, several non-negligible features have appeared. Several photomultiplier tubes did not provide usable signals, since either the tube itself or a channel in the electronics chain was broken. The mean time and position of a neutron hit cannot be determined with sufficient resolution in a half-blind paddle, which directly led

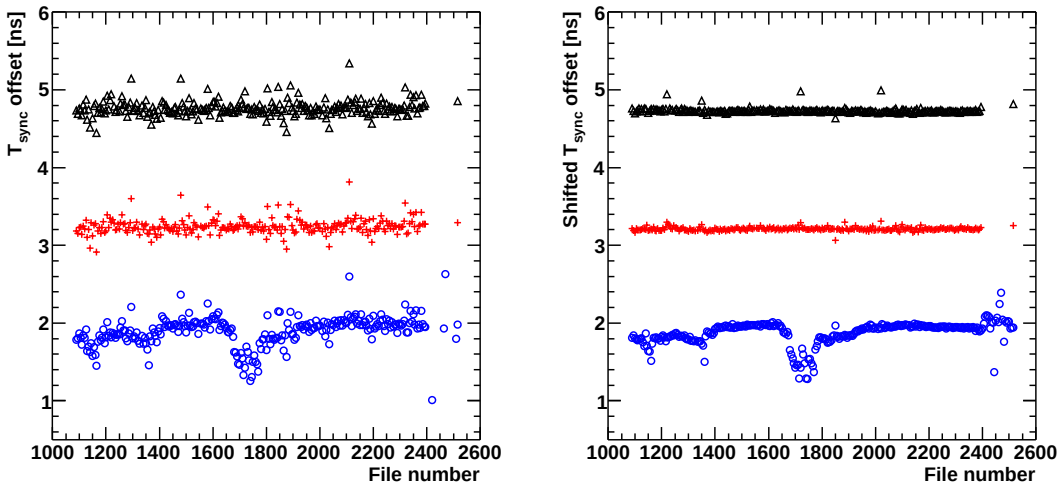

Figure 4.8: LAND T_{sync} parameter evolution as a function of file number. T_{sync} parameter before (left panel) and after (right panel) common shift subtraction. Data labels: LAND paddle 5 (△), 6 (+) and 42 (○).

to switching the concerned paddles off for the analysis. In other cases, both PM tubes delivered signals, but the reconstructed position distributions were strongly skewed. Such a case is shown in figure 4.9. In a normally working LAND paddle, the cosmic ray position distribution is homogeneous over the entire paddle length, as can be seen in figure 4.4. A material defect in the scintillator or a too high PM tube threshold can be the origin of this effect. Extreme cases as depicted in figure 4.9 must be excluded from the analysis, since the position reconstruction cannot be trusted. As has been described in subsection 4.2.4, the DIFF parameters are adjusted to match the geometrical width of the paddle. If, however, only a small portion of the paddle is observed by one of the PM tubes, this small region will be adjusted to match the entire paddle length. Neutrons detected in these paddles will be shifted to wrong locations, resulting in wrong angles and velocities. In less severe cases, where both edges of the paddle can be observed, the effective threshold of both channels has been measured, such that they can be taken into account later by the LAND event generator (section 4.5). In conclusion, 25% of the LAND paddles have been removed from the analysis. The LAND efficiency and acceptance corrections, however, take this into account in detail since it affects the neutron detection probability.

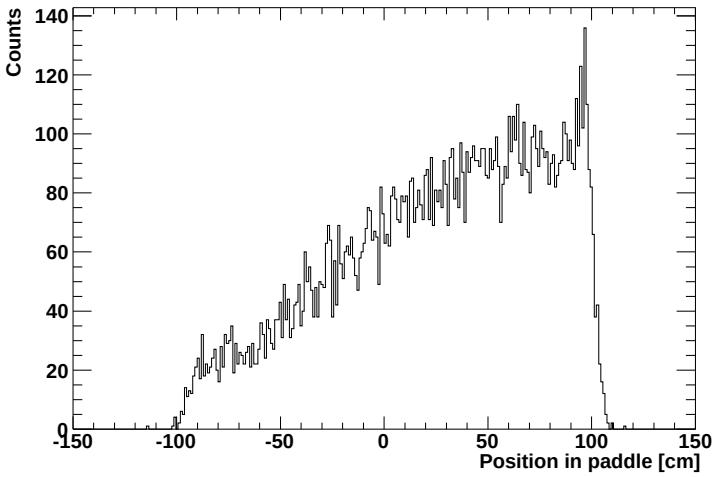

Figure 4.9: Skewed cosmic ray position distribution in LAND paddle 96.

4.3 Calibration of CsI Gamma Detector

The CsI detector is calibrated by measuring the energy spectrum of several radioactive sources, such as ^{22}Na and ^{60}Co. Figure 4.10 illustrates the calibration procedure: in order to extract the precise energy of the photopeaks, a background function must be included in the fitting procedure. In the present case, a linear background convoluted with a smeared step function was assumed[†]. The peak energy is then obtained from the underlying Gaussian distribution.

In figure 4.10, the 511 keV peak from the positron annihilation of the ^{22}Na decay can be observed at approximately channel 4570, along with the 1275 keV $2^+ \rightarrow 0^+$ transition at channel 4780. Combining several peak values allows the determination of the energy slope and offset for the individual crystals. The sources, however, only provide photons with relatively low energies (1-2 MeV). For photons finding their origin in the rest frame of the incoming ions, the Doppler shift must be taken into account, which easily shifts the photon energies to much higher values for forward angles. In order to produce photons for calibration in this energy region, a Pu-C neutron source can be used, producing photons with higher energies *via* the ^{13}C(α,n)^{16}O reaction. The neutrons, however, are also observed in the CsI detector, which complicates the analysis.

4.4 Fragment Tracking through ALADIN

The tracking of charged fragments through the magnetic field of the ALADIN magnet provides the mass-over-charge ratio by considering the balance of the centripetal and

[†]O. Ershova, private communication.

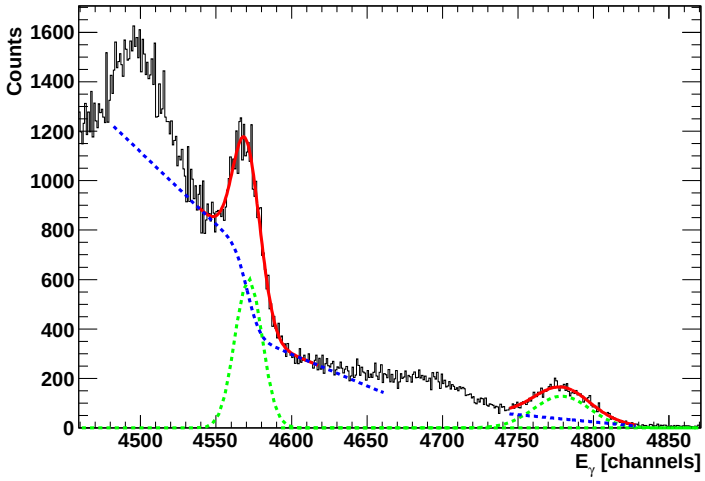

Figure 4.10: CsI calibration with a ^{22}Na source. The spectrum of crystal 40 is shown. The red solid lines show the fit functions for the photopeaks. The dashed blue lines indicate a linear background convoluted with a smeared step function, and the dashed green lines represent the actual Gaussian photopeak.

Lorentz forces:

$$B\rho = \frac{m_u c}{e}\frac{A}{Z}\beta\gamma \tag{4.10}$$

where B is the strength of the magnetic field, ρ is the trajectory radius in the magnetic field, m_u is the unit mass, c is the velocity of light, e is the unit charge, A and Z are the mass and charge numbers of the fragment, β is the fragment velocity, and γ is the Lorentz factor of the fragment. Since the exact value of $B\rho$ for each event cannot be measured in the present experiment, the A/Z ratio must be determined by using a reference-fragment trajectory, where all variables of equation (4.10) are known except for $B\rho$. Equation (4.10) can be re-written for the reference fragment:

$$(B\rho)_0 = \frac{m_u c}{e}\frac{A_0}{Z_0}\beta_0\gamma_0 \tag{4.11}$$

where all quantities with a subscript zero refer to the reference fragment. If equation (4.10) is divided by equation (4.11), the following expression for the mass of any fragment is obtained after rearrangement:

$$A = A_0\frac{B\rho}{(B\rho)_0}\frac{Z}{Z_0}\frac{\beta_0\gamma_0}{\beta\gamma} \tag{4.12}$$

By defining $B\rho = (B\rho)_0 + \delta(B\rho)$, equation (4.12) becomes:

$$A = A_0\left(1 + \frac{\delta(B\rho)}{(B\rho)_0}\right)\frac{Z}{Z_0}\frac{\beta_0\gamma_0}{\beta\gamma} \tag{4.13}$$

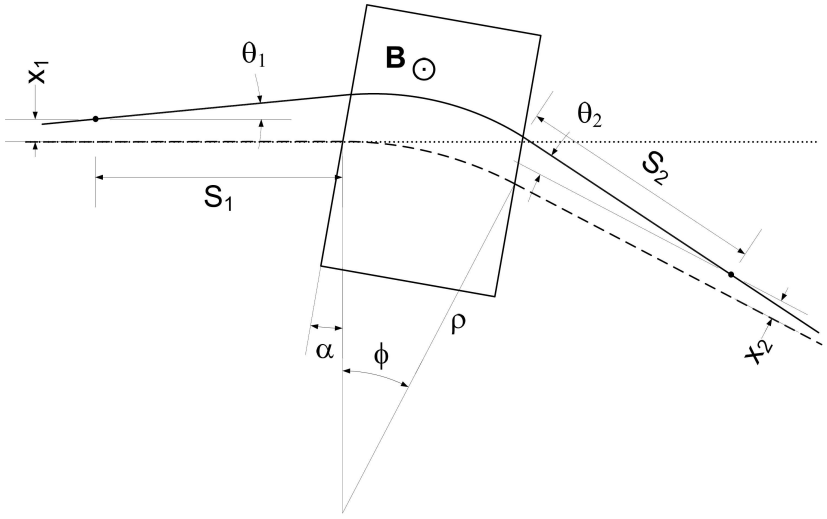

Figure 4.11: Trajectory of charged particles in a dipole magnetic field. The dashed line represents the reference trajectory. For the description of the various variables, see text.

The evaluation of the mass now depends on the relative deviation of the magnetic rigidity with respect to the reference trajectory.

The present situation is illustrated in figure 4.11. The trajectory of a charged fragment can be described by:

$$\begin{pmatrix} x_2 \\ \vartheta_2 \\ \left(\frac{\delta(B\rho)}{(B\rho)_0}\right)_2 \end{pmatrix} = T_2 \cdot F_2 \cdot M \cdot F_1 \cdot T_1 \cdot \begin{pmatrix} x_1 \\ \vartheta_1 \\ \left(\frac{\delta(B\rho)}{(B\rho)_0}\right)_1 \end{pmatrix} \tag{4.14}$$

where the subscripts 1 and 2 indicate the measurement locations before and after the magnet, respectively, x is the lateral displacement with respect to the reference trajectory, ϑ is the angle of the fragment with respect to the reference trajectory, $\left(\frac{\delta(B\rho)}{(B\rho)_0}\right)$ is the deviation of the magnetic rigidity of the fragment with respect to the reference beam, T is the transport matrix in the field-free region, F is the (de)focusing matrix depending on the fringe fields and on the tilt angle α of the field region, and M is the fragment motion matrix in the dipole magnetic field. This formalism is only valid if the $B\rho$ value remains constant in the region depicted by figure 4.11. The transport matrix depends in this case only on the distance S_i between the measuring point and the beginning of the magnetic field and acts only on the lateral displacement:

$$T_i = \begin{pmatrix} 1 & S_i & 0 \\ 0 & 1 & 0 \\ 0 & 0 & 1 \end{pmatrix}, \quad i = 1, 2 \tag{4.15}$$

The (de)focusing matrix modifies the trajectory angle and depends on the angle α at

which the beam enters the magnetic field and on the curvature radius ρ:

$$F_i = \begin{pmatrix} 1 & 0 & 0 \\ \frac{\tan\alpha}{\rho} & 1 & 0 \\ 0 & 0 & 1 \end{pmatrix}, \quad i = 1, 2 \tag{4.16}$$

Finally, the trajectory of a charged particle in a dipole magnetic field is defined by the following matrix:

$$\begin{aligned} M &= \begin{pmatrix} \cos\psi & \frac{\rho}{\eta}\sin\psi & \frac{\rho}{\eta^2}(1-\cos\psi) \\ -\frac{\eta}{\rho}\sin\psi & \cos\psi & \frac{1}{\eta}\sin\psi \\ 0 & 0 & 1 \end{pmatrix} \\ \psi &= \eta\phi \\ \eta &= \sqrt{1-n} \end{aligned} \tag{4.17}$$

where ϕ is the bending angle of the magnetic field and n is the so-called field index, which takes the value $n = 0$ when the dipole field is ideal. By solving equation (4.14) using the matrices described in equations (4.15), (4.16) and (4.17), a general parameterization is obtained:

$$x_2 = a \cdot x_1 + b \cdot \vartheta_1 + c \cdot \frac{\delta(B\rho)}{(B\rho)_0} \tag{4.18}$$

where the parameters a, b and c are determined by evaluating equation (4.14).

The calculation of the fragment mass is quite straightforward from this point on: the deviation of the magnetic rigidity can be obtained with equation (4.18), if the trajectory angle and position are measured on one side of the magnet and another position on the other. This value can then be introduced directly into equation (4.13), which provides the mass value when the charge and velocity has also been measured. A more detailed description of this procedure can be found in reference [72].

4.5 Detector Response

4.5.1 General Considerations

The results obtained by analyzing the experimental data do not match calculated data well due to two major effects: detector efficiency and detector response. The former modifies the measured cross sections, while the latter mainly distorts the data distributions. Even though the two effects can be handled simultaneously, they are decoupled in the present case.

The detection efficiency is mainly defined by LAND, since the neutron trigger was always used, and since the detectors of the charged fragment branch do not cut into the position distributions of the fragments. The first step is the correction of the data for the neutron acceptance and efficiency. Then, the response functions of LAND and of

the CsI gamma detector are calculated separately, since these functions are too complex to be used for the deconvolution of the experimental data. Instead, the two response functions are combined and used to simulate convoluted data based on various input models, which are finally compared to the experimental data.

The LAND contribution to the detector response is obtained *via* a dedicated event generator, which generates neutrons according to several implemented decay models, such as a statistical decay, an n-body decay, and a parametrized decay using experimental neutron position and velocity distributions. For the present case of electromagnetic excitation, the statistical-decay model will be most appropriate. The CsI gamma response is obtained with an external GEANT3 simulation. Photons of known energy and with a known Lorentz boost are generated and directed into the CsI detector. Energy entries in the various CsI crystals are obtained, which allow the calculation of the gamma response based on the add-back routine used for the experimental data, which will be described in subsection 4.5.3.

4.5.2 LAND Efficiency and Acceptance

A precise knowledge of the efficiency and acceptance of LAND is vital for the present experiment, since conditions on the LAND data have been used for all physics results in this analysis. Moreover, many LAND paddles have been deactivated in order to reduce the amount of falsely reconstructed data (*cf.* subsection 4.2.7). First, the effective LAND thresholds must be measured by fitting the lower range of the energy distribution of each channel with a Fermi function multiplied with an exponential decay, as can be seen in the left panel of figure 4.12. The fit function takes the following form:

$$f(E) = \frac{p_1 \exp\left[-E \cdot p_2\right]}{1 + \exp\left[-\left(E - p_3\right) \cdot p_4\right]} \tag{4.19}$$

where E is the energy entry and p_1 to p_4 are the fit parameters. The threshold is represented by parameter p_3. The right panel of figure 4.12 shows the distribution of measured LAND thresholds, which will be used in the LAND event generator. Next, the threshold value must be converted from QDC channels to MeV, since the event generator runs in the latter unit. This is achieved by considering the neutron energy distributions of the measured and simulated neutron events. The comparison either of the neutron energy peak values or of the fit parameter values of the high-energy tail in the energy distributions yields the conversion parameters. The experimental and simulated hit multiplicity distributions are then compared to check the validity of the conversion. If they do not perfectly match, the channel-to-energy conversion factor can be slightly adjusted until the distributions match.

Finally, the event generator creates neutrons over a wide range of energies, taking into account the deactivated LAND paddles and the effective thresholds. This generated

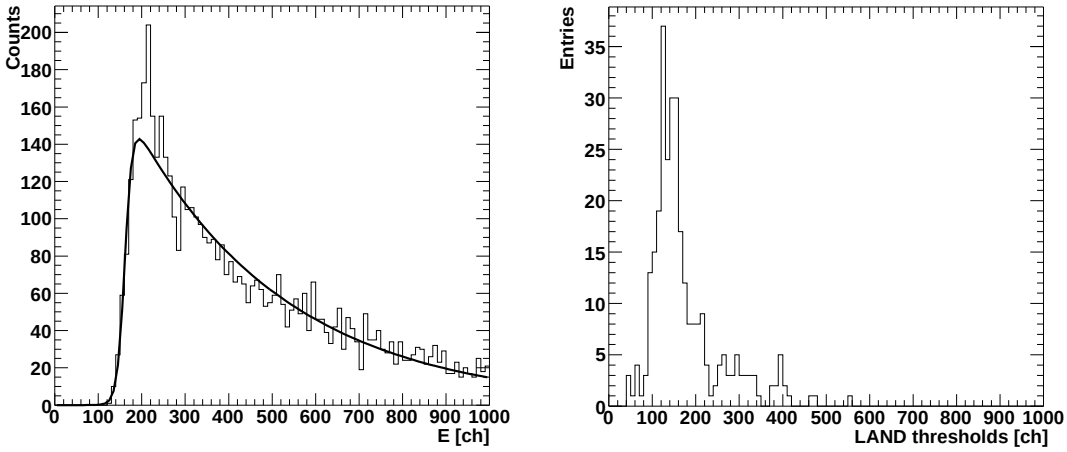

Figure 4.12: Measurement of the LAND threshold values. Left panel: lower range of the energy distribution of LAND plane 10, paddle 19, 2^{nd} PM tube, with fit function. Right panel: LAND threshold distribution for all 400 electronic channels, given in QDC channel units.

data provides three contributions to the efficiency and acceptance of LAND: the nominal neutron detection efficiency, the additional LAND efficiency contribution, and the LAND acceptance. All quantities can be expressed as a function of the kinetic energy of the neutron, for the 1n-channel, or as a function of the sum of the kinetic energies when more than one neutron is emitted. The nominal LAND efficiency was derived from an earlier LAND calibration experiment and depends on the neutron energy. It is the maximum neutron-detection efficiency that can be reached. For 500 MeV neutrons, this value is approximately 94% [73]. The additional efficiency contribution depends on the kinetic energy of the neutrons and takes the inactive paddles and effective thresholds into account. Due to the position of the switched-off paddles, the increase of kinetic energy expands the possible neutron interaction region over an increasing number of blind paddles, thus decreasing the efficiency, until the entire detector face is covered, yielding a constant efficiency value from this point on. The LAND acceptance depends on the neutron kinetic energy only and arises from the neutron kinematics. The acceptance remains at 100% up to a precise energy, from which point on the proportion of neutrons flying past LAND increases with increasing neutron kinetic energy. The decrease of acceptance is well described by an exponential decay function.

The experimental data can be corrected for these effects on an event-by-event basis, by using the following factor:

$$w\left(E_{n,kin}\right) = \epsilon_{nom}^{-1} \cdot \epsilon_{eff}^{-1} \cdot \epsilon_{acc}^{-1} \tag{4.20}$$

where w is the correction factor, with which the event must be weighted, ϵ_{nom} is the

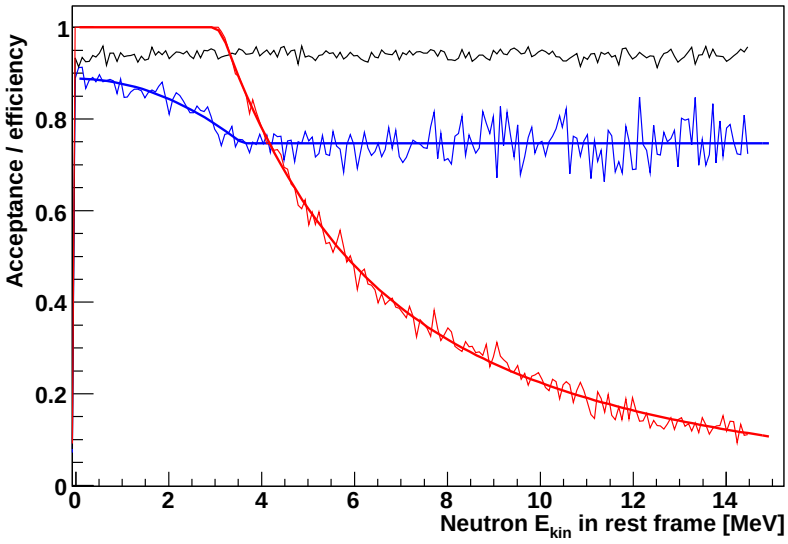

Figure 4.13: LAND efficiency and acceptance contributions in the 1n-channel. The horizontal black line represents the nominal LAND efficiency and was used as a data integrity check. The LAND acceptance (red line) stays constant at 100% up to 3.07 MeV, from which it thereafter decreases exponentially. The additional LAND efficiency contribution (blue line) slightly decreases up to 3.58 MeV and then remains at a constant value.

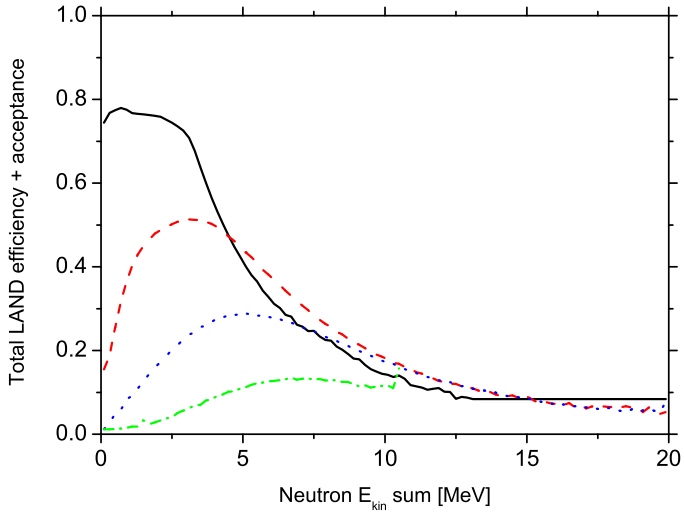

Figure 4.14: Total LAND efficiency and acceptance as a function of the sum of neutron kinetic energies. 1n channel: solid black line. 2n channel: dashed red line. 3n channel: dotted blue line. 4n channel: dashed-dotted green line.

nominal LAND efficiency, ϵ_{eff} is the additional efficiency contribution, and ϵ_{acc} is the acceptance contribution. Figure 4.14 shows the total combined LAND efficiency and acceptance $w\left(E_{n,kin}\right)$ as a function of the sum of the neutron kinetic energies up to the 4n-channel. A strong inefficiency is observed at small neutron kinetic energy sums for the 2n-, 3n- and 4n-channels, which is due to the neutron reconstruction algorithm. Since each neutron interaction in LAND leads to the production of many secondary particles, several LAND hits will be associated with one neutron. The hit-multiplicity distribution peaks around 2 or 3 for neutrons at approximately 500 MeV. If the hit distributions of several neutrons strongly overlap in time and/or in space, there is a high probability that the algorithm will attribute hits from neutrons later in time to the earlier ones, which might result in losing one or more neutrons. The highest combined efficiency and acceptance is therefore obtained when the neutrons are far enough apart, such that the hit distributions do not overlap, but still in an energy range where they cannot fly past LAND.

4.5.3 CsI Response

Before the LAND setup response can be established, the CsI gamma detector response must be determined, since it is required as input for the total response. A GEANT3 simulation is used to generate energy entries in the 144 CsI crystals of the detector. The gamma emission frame is boosted to approximately 500 AMeV, in which gammas with energies ranging from 0 to 5 MeV are emitted at random angles. In order to reconstruct the gamma energies in the emission rest frame, the energies of the individual crystals must be summed and Doppler-corrected. Two effects prevent the routine from reconstructing the emission energy: the CsI crystal efficiency and the clustering algorithm. The efficiency is determined with source runs during the experiment and is defined for the 12 rings of the detector[‡]. The values are listed in table 4.1. It should be noted

CsI ring	1	2	3	4	5	6
Efficiency	1.0	0.973	1.0	0.963	0.914	0.781
CsI ring	7	8	9	10	11	12
Efficiency	0.808	0.754	0.748	0.601	0.557	0.750

Table 4.1: CsI ring-efficiency values.

that these values are not the absolute efficiencies of the detector rings, but rather the additional observed efficiencies with respect to the efficiencies determined by the simulation. These values are then used in the crystal clustering routine, which reconstructs

[‡]O. Ershova, private communication.

the gamma energy convoluted with the CsI detector response. A cluster is defined by the crystal with the highest lab-frame-energy value and its 12 neighboring crystals, in which a portion of the initial energy has been also deposited. All energies are summed and then Doppler-corrected to the angle of the crystal with the highest energy entry. Four gamma response functions are shown in figure 4.15. All functions that have been generated are parametrized and stored for use in the LAND setup response calculation.

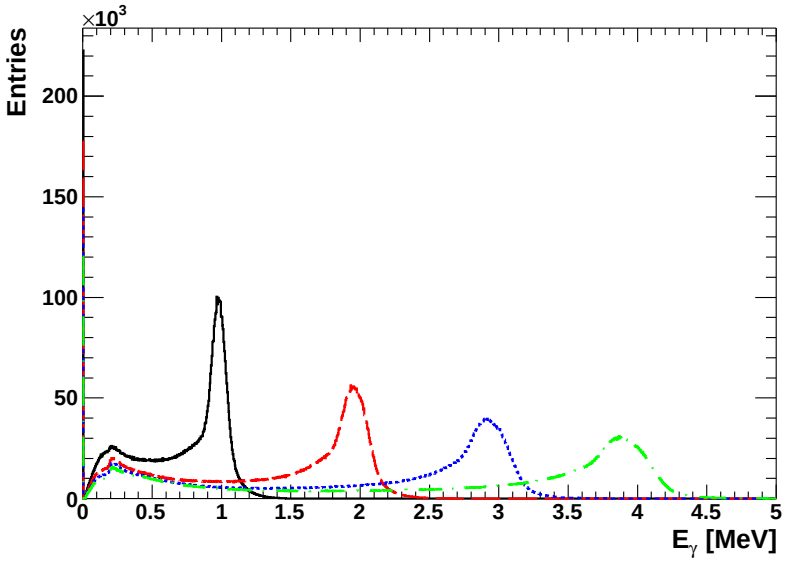

Figure 4.15: CsI gamma-detector response for the cluster add-back. Four gamma energies are shown: 1 MeV (black solid line), 2 MeV (dashed red line), 3 MeV (dotted blue line) and 4 MeV (dashed-dotted green line). The photons are emitted isotropically in the rest frame.

4.5.4 Setup Response

The experimental data is not only distorted by the response of the various detectors, but can also contain contaminations of nuclei with neighboring masses if the neutron reconstruction and conditions on the fragment mass are not conservative enough. The final setup response must therefore take these effects into account. The LAND event generator is tuned to provide realistic LAND events, also using the gamma response as input (*cf.* subsection 4.5.3). While in the analysis of the experimental data the neutron multiplicity is required to be consistent with the fragment mass, this condition is removed for the creation of the response matrix, since all possible contaminations must be quantified in order to identify them in the data. For a given nucleus, events are generated with all possible excitation energies in a reasonable range, keeping all possible generated and detected neutron multiplicities. The results are filled into a

four-dimensional response matrix, indexed with the number of generated neutrons, the number of detected neutrons, the generated excitation energy, and the reconstructed excitation energy.

When using the statistical-decay model, the LAND event generator receives an excitation energy value and distributes it among all nucleons. The event generator requires at least one neutron to be emitted from the nucleus, according to the statistical decay described in subsection 4.5.4. Neutrons are emitted until the remaining excitation energy is smaller than the subsequent neutron threshold. After the emission of the last neutron, the remaining excitation energy is emitted *via* a gamma cascade. The nuclear structure of the remaining nucleus is required to generate realistic gamma transitions. If the excitation energy is above the last level provided by the input from literature, a level continuum is assumed. One or several photons will be generated, such that discrete levels are reached in order to decay to the ground state of the fragment. In this process, the spin and parity selection rules are respected. For each gamma transition, an energy is randomly selected from the corresponding gamma response function. The results are then stored in an n-tuple data structure for further use by the response matrix routine.

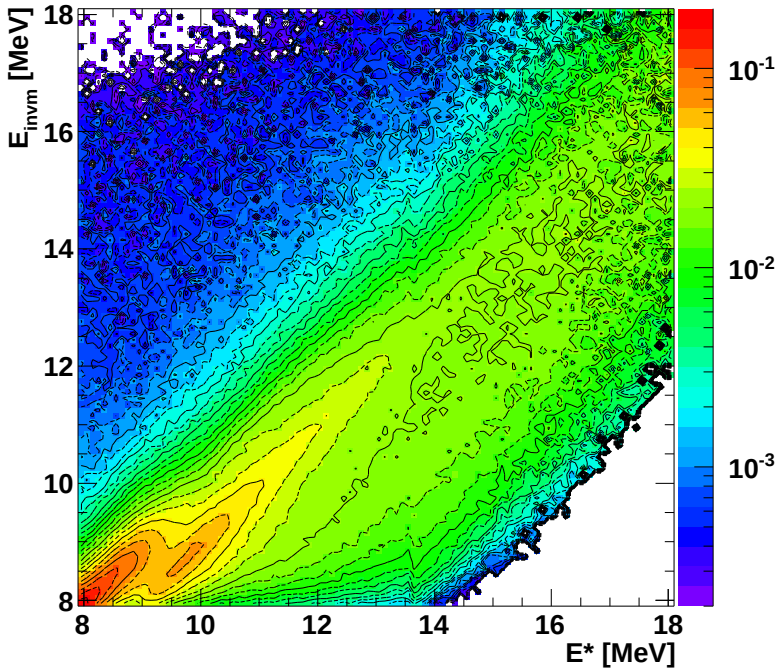

Figure 4.16: Response matrix for the 1n channel of ^{68}Ni. E* is the generated excitation energy and E_{invm} is the reconstructed excitation energy obtained *via* the invariant mass.

Figure 4.16 shows an example of a two-dimensional projection of the response matrix, where the number of generated neutrons and the number of detected neutrons are both

fixed at one. If the detector response were perfect, all entries would be located on a diagonal line, thus reconstructing exactly the generated excitation energy E*. This is clearly not the case, since the reconstructed excitation energy is systematically smeared to lower values. This information is required to interpret the experimental data. Since the measured data is intrinsically convoluted with the detector response, the following procedure will be applied to extract the deconvoluted results using various models:

1. The model generates a variable distribution based on several parameters.
2. The distribution is converted to Coulomb excitation units.
3. The distribution is convoluted with the detector response.
4. The generated and experimental distributions are compared using χ^2 minimization.
5. If the χ^2 minimum is not reached, the model parameters are adjusted and the procedure restarts at step 1.

Once the minimum has been reached, the model can be considered as describing the deconvoluted data distribution. The folding procedure for the excitation energy distribution can be described with the following equation:

$$\left(\frac{d\sigma_C}{dE_{invm}}\right)(E_{invm}) = \sum_{i=1}^{4}\sum_{j=1}^{3}\int_{E^*}\mathcal{R}\,(i,j,E^*,E_{invm})\cdot\mathcal{B}\,(i,E^*)\cdot\mathcal{M}\,(i,j)\cdot\left(\frac{d\sigma_C}{dE^*}\right)(E^*)\,dE^* \tag{4.21}$$

where $d\sigma_C/dE_{invm}\,(E_{invm})$ is the convoluted Coulomb excitation strength function, i and j are the number of neutrons generated and detected, respectively, E^* is the generated excitation energy, E_{invm} is the reconstructed excitation energy, $\mathcal{R}$ is the response matrix, $\mathcal{B}$ is the branching ratio matrix, $\mathcal{M}$ is the mass matrix, and $d\sigma_C/dE^*\,(E^*)$ is the generated Coulomb excitation strength distribution. While the response matrix has been discussed previously, the branching ratio and mass matrices must still be described.

The branching ratio matrix provides the probability of accessing a given decay channel as a function of excitation energy. In the present case, only neutron decay channels are considered. The values are linked to the statistical decay of the nuclei under investigation, and therefore the matrix can be directly obtained while establishing the response matrix. Figure 6.10 (page 108) shows the branching ratios for ^{68}Ni obtained with three different routines.

The mass matrix defines the proportion of statistics of a given fragment inside the mass cuts, along with the amount of contamination. The following matrix shows the

values of the first few decay fragments of ^{68}Ni:

$$\mathcal{M}(i,j) = \begin{pmatrix} 1.0 & 0.05 & 0 & \dots \\ 0.02 & 1.0 & 0.02 & \dots \\ 0 & 0.02 & 1.0 & \dots \\ \vdots & \vdots & \vdots & \ddots \end{pmatrix} \tag{4.22}$$

Each mass cut is evaluated in order to extract the amount of data inside the cut as well as the degree of contamination. The cross sections are corrected for the number of good events lying outside the cut, which explains why $\mathrm{diag}(\mathcal{M}) = (1.0, 1.0, \dots)$. The contamination values are obtained from the experimental data analysis routine, and are also corrected as the $i = j$ elements. The ability to partially resolve the fragment masses reduces the amount of contamination, seen as a reduction of off-diagonal values in the mass matrix (4.22). The contamination values in the present data set are almost negligible, meaning that structures in the excitation energy distributions due to other isotopes will not play a major role.

Chapter 5

Analysis Concepts

Up to this point in the analysis, the data has been treated in a non-specific manner, since the calibration procedure does not strongly depend on the type of target or on the ion species present in the beam. In order to derive absolute cross sections from various runs, the data must be normalized appropriately. This procedure will be explained in the first section. Once normalized data is accessible, the nuclear and background contributions can be identified and subtracted, which will be described in the second section, giving access to clean electromagnetic excitation data. The third section of this chapter will present the procedure to access the excitation energy distributions based on the invariant-mass formalism. Finally, a set of conditions and approximations on the data will be introduced, which are required to isolate individual reaction channels.

5.1 Data Normalization

In order to measure a reaction cross section, not only the number of reactions is required, but also the total number of events, such that a reaction probability can be calculated. This is achieved by using the various triggers set up for the present experiment. Table 5.1 lists the first few triggers used in the nickel experiment. The Good Beam signal is the POS signal in anti-coincidence with the ROLU signal, which ensures triggering on a collimated beam. The fragment signal is in principle produced by the GFI detectors, although this trigger was not used in the present experiment. The Spill On signal is provided by the accelerator signal infrastructure, and simply indicates when the beam should be expected. The other signals speak for themselves. The various triggers are created when the selected signals are observed in coincidence.

The full measurement of the non-reacting events is not useful, since it simply wastes data-storage space and increases the dead time of the acquisition system. Less important hardware triggers, such as the minimum-bias trigger, are therefore down-scaled, which systematically ignores a certain number trigger requests. In the present experiment, a

Tbit	Tpat	Name	Good Beam	Frag	LAND	TFW	CsI Veto	CsI Sum	Spill On
1	1	Min Bias	x						x
2	2	Fragment	x	x		x			x
3	4	LAND	x		x				x
4	8	CsI Sum	x					x	x
5	16	CsI Veto	x				x		x

Table 5.1: On-spill trigger-pattern list for the nickel experiment. Only the first few triggers are listed.

down-scale factor of 2^n can be selected. As an example, an $n = 8$ setting corresponds to a down-scale factor of 128, which means that 127 trigger requests are ignored and only the 128^{th} request will lead to a trigger. Figure 5.1 presents as example the trigger-pattern

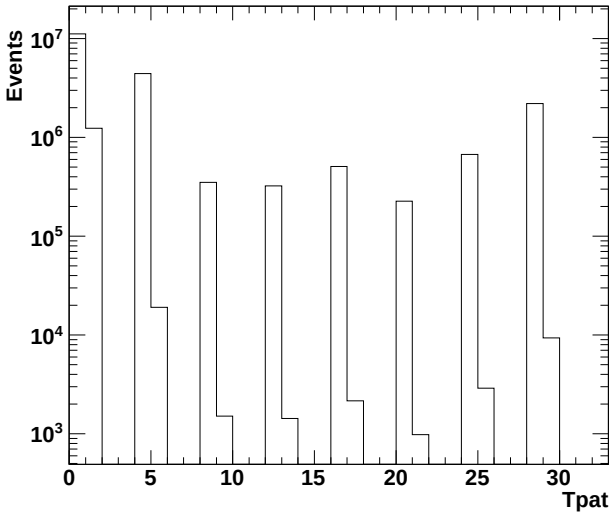

Figure 5.1: Trigger-pattern distribution for the Pb target runs of ^{68}Ni.

distribution of the Pb target runs of ^{68}Ni. Each event is labeled with the so-called Tpat variable representing the various signals used to build the master trigger for the read-out of the data stored in the electronic modules. The Tpat variable is a 16-bit data word, which is defined by the various analog signals originating coincidently from various detectors. A so-called Tbit value is assigned to each signal, switching the defined bit on or off if the signal is present or not. The value of the Tpat variable is simply the 16-bit data word expressed in the decimal system. Therefore, a Tpat=5 event has a LAND

event in coincidence with the Minimum Bias trigger. If the latter trigger would not have been down-scaled, one should only observe Tpat=5 events, since the LAND trigger can only be generated when the Minimum Bias conditions are met as well.

As the number of incoming ions is required for the calculation of cross sections, the Tbit=1 events could simply be counted and multiplied by the corresponding down-scale factor. The precise value of this factor can, however, deviate from the nominal value which has been set manually. A direct measurement of the down-scale factor is possible by using the Tpat distribution and by choosing the Tbit used in the analysis. For the study of neutron-rich nuclei, the LAND trigger is the most important trigger, and will therefore be chosen for this purpose. Since Tbit=3 is not down-scaled, the calculation is simple. The coincidence of Tbit=1 and Tbit=3 leads to a Tpat=5 trigger only every 2^n-th event, meaning that the remaining 2^n-1 events are seen as Tpat=4 events. The down-scale factor is then calculated by:

$$2^n = \frac{N(4) + N(5)}{N(5)} \tag{5.1}$$

where $N(i)$ is the integral of the Tpat=i bin. The value of n is usually close to an integer. Deviations can occur due to the electronics, or if different values of n have been used in the same run.

5.2 Handling of Background and Nuclear Contributions

The measurement of electromagnetic excitation is always accompanied by secondary reactions when measured *via* the virtual photon approach. Two contributions come into play, namely non-specific reactions taking place outside of the target and reactions at the target due to nuclear interactions. The former can be estimated with data from runs without a target: this provides typical interactions in material in the beam line, around the target area and in the various detectors. However, these runs do not give exactly the background distributions measured in the lead target. Since empty-target runs mainly deliver unreacted beam, the position of the beam through the detectors behind the target is slightly different from when a target is inserted, due to the absence of straggling in the target material. Unlike reactions inside the target, the background reactions are undefined due to the complex mixture of materials in the beam line. Therefore, it is impossible to calculate a cross section for these interactions, forcing the background subtraction to take place on the interaction-probability level, which is defined as the ratio of events attributed to the chosen reaction channel to the total number of events.

The nuclear contribution can be estimated with data from carbon-target runs. The electromagnetic and nuclear cross sections will be considered as independent quantities, neglecting eventual Coulomb-nuclear interference terms (*cf.* equation (2.13)), as the precision of the present data is not sufficient to identify an interference contribution.

Since electromagnetic excitation follows approximately a quadratic law with respect to the charge of the target nucleus, the carbon target will only provide a minor electromagnetic excitation contribution with respect to the lead target. The nuclear interaction cross section is related to the size and thus to the radii of the interacting nuclei. Since the nuclear interaction cross section is measured on carbon, it must be rescaled for the lead target. This can be achieved by using the following semi-empirical model [74], providing the nuclear cross section σ_T^{nucl} for a target T using the measured cross section of a carbon target σ_C:

$$\sigma_T^{nucl} = \frac{1 + a \cdot A_T^{1/3}}{1 + a \cdot A_C^{1/3}} \sigma_C \equiv \alpha_T \sigma_C \tag{5.2}$$

with $a = 0.14$. Considering a ^{nat}Pb target with $A_{Pb} = 207.2$, a scaling factor $\alpha_{Pb} = 1.385$ is obtained. The calculation of the Coulomb excitation cross section relies on the following relationship connecting the cross section σ with the interaction probability p for a target T:

$$\sigma_T = p_T \cdot \frac{M_m(T)}{d_T \cdot N_{Av}} \tag{5.3}$$

where $M_m(T)$ is the molar mass of the target material [g/mol], d_T is the target thickness [g/cm^2], and N_{Av} is the Avogadro number [mol^{-1}]. Taking into account that the background contribution must be subtracted on the interaction-probability level, the Coulomb excitation interaction probability is given by the following expression:

$$p_{Coulex} = (p_{Pb} - p_{empty}) - (p_C - p_{empty}) \cdot \left(\alpha_{Pb} \frac{d_{Pb} \cdot N_{Av}}{M_m(Pb)} \cdot \frac{M_m(C)}{d_C \cdot N_{Av}} \right) \tag{5.4}$$

Since both Pb and C target measurements contain background, it must be subtracted from both contributions. However, subtracting the background from both measurements yields a larger statistical error than if only the background difference is subtracted once in the end. This can be shown by rearranging equation (5.4):

$$p_{Coulex} = p_{Pb} - p_C \left(\alpha_{Pb} \frac{d_{Pb}}{M_m(Pb)} \cdot \frac{M_m(C)}{d_C} \right) - p_{empty} \left(1 - \alpha_{Pb} \frac{d_{Pb}}{M_m(Pb)} \cdot \frac{M_m(C)}{d_C} \right) \tag{5.5}$$

The final Coulomb excitation cross section is given when combining equations (5.5) and (5.3):

$$\sigma_{Coulex} = p_{Pb} \left(\frac{M_m(Pb)}{d_{Pb} N_{Av}} \right) - p_C \left(\alpha_{Pb} \frac{M_m(C)}{d_C N_{Av}} \right) - p_{empty} \left(\frac{M_m(Pb)}{d_{Pb} N_{Av}} - \alpha_{Pb} \frac{M_m(C)}{d_C N_{Av}} \right) \tag{5.6}$$

This last expression not only provides pure electromagnetic excitation integral cross sections, but may also be applied bin-wise to any observable distribution.

While the cross section expression (5.6) is valid for any target thickness d and nuclear interaction scaling factor α_{Pb}, it can be shown that a measurement on an empty target

is not necessary if the Pb and C target thicknesses are carefully chosen to satisfy:

$$\frac{d_{Pb}}{d_C} = \frac{M_m(Pb)}{\alpha_{Pb} M_m(C)} \tag{5.7}$$

Using (5.7) in (5.6), the expression for the cross section reduces to:

$$\sigma_{Pb} = \frac{M_m(Pb)}{d_{Pb} N_{Av}} \left(p_{Pb} - p_C\right) \tag{5.8}$$

As an example, the lead-to-carbon target thickness ratio must be equal to 12.5 if the nuclear scaling factor is evaluated with expression (5.2) in order to be able to use equation (5.8) for the cross section calculation.

5.3 Neutron Kinetic Energy

In order to calculate the kinetic energy of the neutrons detected by LAND, knowledge of their momenta is required. In turn, the momentum is obtained from the flight time of each neutron between the target and its primary interaction in LAND, as well as from the angle of its trajectory. Since eventually the kinetic energy in the rest frame of the incoming ion is requested, the velocity and angles of the incoming ion are also necessary. As described in subsection 2.3.2, the neutrons are expected to be emitted by the parent nucleus *via* statistical decay, meaning that the neutron energies are relatively small in the rest frame, which in turn yields neutron velocities of the order of the incoming beam velocity in the lab frame. Since the beam energy of the present experiment is approximately 500 AMeV, the kinematic treatment of the neutrons must take relativistic effects into account. The kinetic energy can be obtained by performing a Lorentz transform on the total energy and longitudinal momentum measured in the lab frame:

$$\begin{pmatrix} E^* \\ p^*_{\parallel} \end{pmatrix} = \begin{pmatrix} \gamma_f & -\beta_f\gamma_f \\ -\beta_f\gamma_f & \gamma_f \end{pmatrix} \begin{pmatrix} E \\ p_{\parallel} \end{pmatrix}, \quad p^*_{\perp} = p_{\perp} \tag{5.9}$$

where E^* and $p^*_{\parallel}$ are the energy and longitudinal momentum in the rest frame, and E and $p_{\parallel}$ the same quantities in the lab frame. The subscript f refers to the rest frame of the starred (*) quantities. The transversal momentum $p_{\perp}$ is not affected by the Lorentz transformation. When the energy term of equation (5.9) is evaluated while remembering that $E = \gamma m_0 c^2 = E_{kin} + m_0 c^2$, the following expression for the kinetic energy in the rest frame is obtained:

$$E^*_{kin} = \gamma_f \gamma m_n - \beta_f \gamma_f p_{\parallel} - m_n \tag{5.10}$$

where m_n is the neutron rest mass. The longitudinal momentum of the neutron in the lab frame is given by:

$$p_{\parallel} = m_n \beta \gamma \cos\vartheta \tag{5.11}$$

The angle ϑ is defined by the vector of the incoming parent ion and the outgoing neutron.

5.4 Invariant Mass

While investigating heavy-ion-induced electromagnetic excitation of atomic nuclei, many observables may be measured directly with the experimental setup, *e.g.*, time-of-flight, position and energy loss. Other quantities, however, are only accessible *via* an event-by-event reconstruction. One of the main interests in the field of electromagnetic excitation of exotic nuclei is the measurement of their excitation function. Since the experiments at the LAND setup are performed in inverse kinematics at relativistic beam energies, the direct measurement of the excitation energy is impossible when applying the equivalent-photon formalism. Therefore, the excitation energy may only be reconstructed by identifying all incoming and by tracking and identifying all outgoing species, and by calculating the invariant mass on an event-by-event basis.

The invariant mass is, as its name suggests, Lorentz invariant, which is helpful when switching between laboratory and ion rest frames. In the rest frame of a given object, the invariant mass is equal to its rest mass m_0. The measurement of the invariant mass relies on the use of four-momentum vectors [75], which are composed of the total energy and of the three momentum vector components:

$$\mathbf{P}^{\mu} = \begin{pmatrix} E \\ p_x \\ p_y \\ p_z \end{pmatrix} \tag{5.12}$$

$$M_{inv}^2 = \eta_{\mu\nu}\mathbf{P}^{\mu}\mathbf{P}^{\nu} = E^2 - p_x^2 - p_y^2 - p_z^2 \tag{5.13}$$

where $\eta_{\mu\nu} = \mathrm{diag}(1, -1, -1, -1)$ is the Minkowski metric and $c = 1$.

As shown in equation (5.13), the invariant mass squared is then the inner product of the four-momentum. The invariant masses of the excited incoming (1) and outgoing (2) systems are given by the following expressions:

$$M_{inv}^{(1)} = m_{proj} + E^* \tag{5.14}$$

$$M_{inv}^{(2)} = \sqrt{\left(\begin{array}{c} \sum\limits_i E_i \\ \sum\limits_i \overrightarrow{p_i} \end{array} \right)^2} \tag{5.15}$$

where the sums run over all i fragments in the outgoing channel. The excitation energy E^* in expression (5.14) is decoupled from the projectile invariant mass m_{proj} after expanding the total invariant mass in a Taylor series, where the recoil of the photon on the heavy ion is neglected. The energy of the gamma photons may as well be decoupled from the heavy fragments in a similar way for the outgoing invariant mass. Neglecting the energy of the emitted gamma photons in a first step, the energy and momentum

terms of (5.15) are defined as following:

$$\left(\sum_i E_i\right)^2 = \sum_i \left(\gamma_i m_i\right)^2 + \sum_{i\neq j} \gamma_i\gamma_j m_i m_j \tag{5.16}$$

$$\left(\sum_i \overrightarrow{p_i}\right)^2 = \sum_i \left(\beta_i\gamma_i m_i\right)^2 + \sum_{i\neq j} \beta_i\beta_j\gamma_i\gamma_j m_i m_j \cos\vartheta_{ij} \tag{5.17}$$

Taking into account that $\gamma^2\left(1-\beta^2\right)=1$, equations (5.16) and (5.17) are introduced into expression (5.15), to which the gamma energy has been added, providing the following outgoing invariant mass:

$$M_{inv}^{(2)} = \sqrt{\sum_i m_i^2 + \sum_{i\neq j} \gamma_i\gamma_j m_i m_j \left(1-\beta_i\beta_j\cos\vartheta_{ij}\right)} + E_\gamma \tag{5.18}$$

Due to the conservation of the invariant mass, the excitation energy is expressed by:

$$E^* = \sqrt{\sum_i m_i^2 + \sum_{i\neq j} \gamma_i\gamma_j m_i m_j \left(1-\beta_i\beta_j\cos\vartheta_{ij}\right)} + E_\gamma - m_{proj} \tag{5.19}$$

Expression (5.19) shows that the reconstruction of the excitation energy relies on the identification and tracking of all outgoing species and on the rest mass of the incoming ion.

5.5 Data Conditions and Approximations

Since the experiments at the LAND setup are performed using heavy ions at relativistic energies, a large variety of reaction channels is accessible. Also, since the FRS was set up to deliver a cocktail beam in order to measure several nuclei simultaneously, the incoming nuclei must be selected very carefully. The isolation of a reaction channel requires several conditions on the various measured quantities, *e.g.*, charge, mass, and velocity. The following subsections divide the applied conditions into two classes, namely the conditions for the incoming and outgoing channels, respectively.

5.5.1 Incoming Channel

The identification of the incoming ions is performed using on one hand the charge of the ions, provided by the energy loss in a position-sensitive pin diode, and on the other the mass-over-charge ratio, given by the measurement of the magnetic rigidity and by the velocity measurement between the end of the FRS (by the S8 scintillator) and the POS detector in Cave C. A two-dimensional histogram of these two quantities provides the opportunity to place a graphical cut around individual ion distributions. Figure 5.2

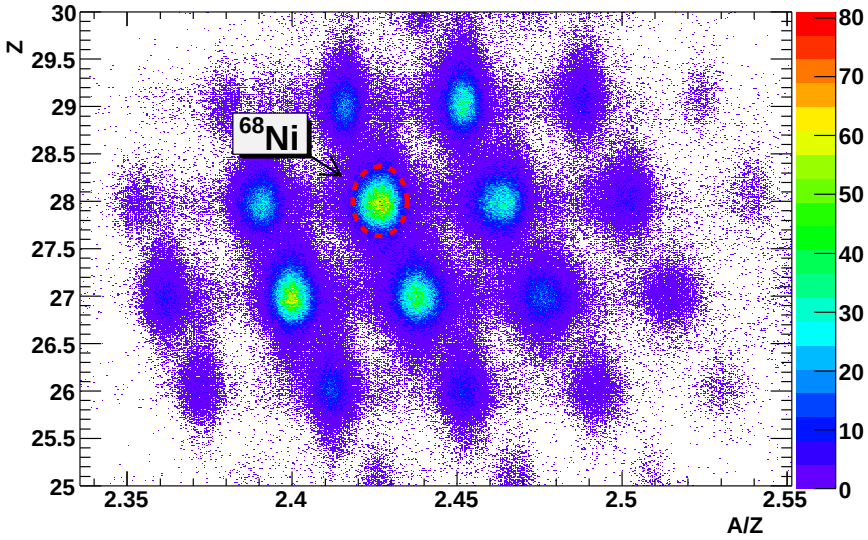

Figure 5.2: Identification plot for the incoming ions. The graphical cut for ^{68}Ni is shown as an example.

shows the incoming identification plot for a run from which the ^{68}Ni data will be extracted. Although any two-dimensional graphical cut will work, elliptical cuts will be used, since they can be stored only by specifying the two radii σ and the center of the ellipse ($\overline{Z}_{in}$ and $\overline{\left(\frac{A}{Z}\right)}_{in}$):

$$\left(\frac{Z_{in}-\overline{Z}_{in}}{\sigma_{Z_{in}}}\right)^2+\left(\frac{\left(\frac{A}{Z}\right)_{in}-\overline{\left(\frac{A}{Z}\right)}_{in}}{\sigma_{\left(\frac{A}{Z}\right)_{in}}}\right)^2<1 \tag{5.20}$$

Since all quantities for the chosen reaction channel will use the same incoming cut, precise knowledge of the fraction of incoming ions enclosed inside the cut is not required. However, if the incoming cut is too restrictive, the resulting measured quantities will have a higher associated error, due to lower statistics. The incoming cut should therefore enclose as many incoming ions as possible, while restricting the contamination by neighboring ion species to a minimum amount.

5.5.2 Outgoing Channel

Once the incoming species has been selected, the reaction channel must be defined by selecting the appropriate outgoing species. As for the incoming channel, the mass and charge of the fragments define precisely the outgoing channel. Due to the limited resolving power of the present experimental setup, a high-resolution measurement of both quantities is not available. The following conditions are therefore required to define unambiguously the outgoing channel.

When converting quantities from the lab frame into the rest frame of the incoming ion, an approximation on the ion velocity must be made. The thickness of the targets used during the present experiment is too large to neglect the energy loss of the ions. The precise location of the reaction vertex cannot be defined inside the target, and therefore the reaction is considered to take place in the middle of the target depth. The rest frame of the incoming ion will thus be traveling with the ion velocity at this point with respect to the lab frame. The velocity measured by the time-of-flight method between the target and the TFW does not deliver a time resolution with sufficient precision, such that the incoming velocity is used for the conversion. Since the momentum transfer in Coulex reactions is small compared to the total momentum of the heavy ion and to the momentum spread of the incoming beam, this approximation can be easily justified.

Fragment Charge

The charge of a particle can be determined by measuring its energy loss in matter, which is governed by the Bethe-Bloch formula [76]:

$$-\frac{dE}{dx} = 2\pi N_{Av} r_e^2 m_e c^2 \rho \frac{Z_T}{A_T} \frac{Z_P^2}{\beta^2} \left(\ln \left[\frac{2m_e \gamma^2 v^2 W_{\max}}{I^2} \right] - 2\beta^2 - \delta - 2\frac{C}{Z} \right) \tag{5.21}$$

with Avogadro's number N_{Av}, the classical electron radius r_e, the electron mass m_e, the density ρ, the charge Z_T and mass A_T numbers of the absorbing material, the charge Z_P and velocity v (leading to β and γ) of the projectile, the maximum energy transfer on a central collision $W_{\max}$, the mean excitation potential I, and the density δ and shell C correction terms. Since only relative energy-loss measurements have been performed, most of the terms above can be safely neglected. Formula (5.21) can then be reduced to [76]:

$$Z_P \propto f(\beta) \sqrt{-\frac{dE}{dx}} \tag{5.22}$$

where $f(\beta)$ is a function of the velocity alone. For the following development, a low-level assumption is made on the velocity dependence, setting $f(\beta) = \beta$. The fragment charge must only be reconstructed in the immediate vicinity of the charge of the incoming ion, leading to small velocity variations and justifying the use of a linear function. Since the energy-loss measurement offers a sufficiently high resolution, such that individual charges can be distinguished, an analytical expression for the charge can be deduced by fitting the energy-loss values with the following function:

$$Z_P = \beta \sqrt{E_m \cdot S + O} \tag{5.23}$$

where E_m is the measured energy loss in the detector and S and O are slope and offset parameters to be determined by the fit.

The fragment charge can be easily determined with equation (5.23) by choosing two detectors after the target: the third PSP detector and the TFW. The PSP detector is

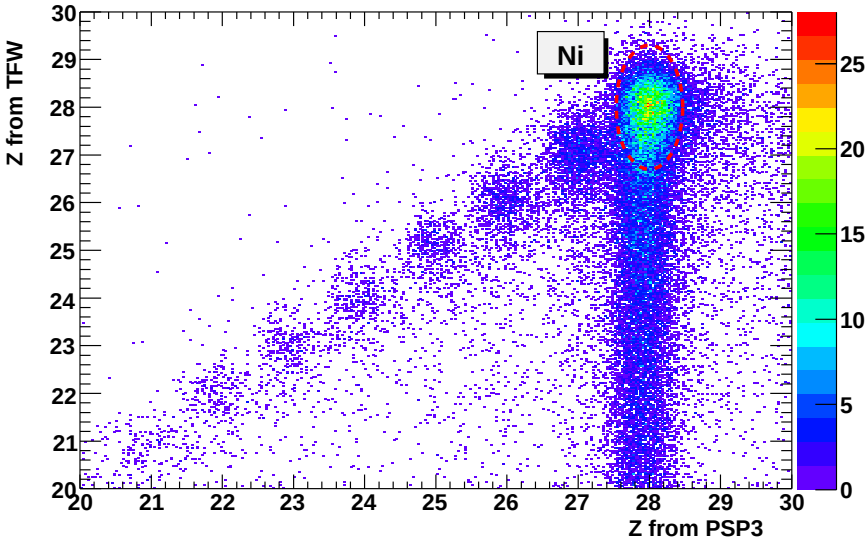

Figure 5.3: Outgoing charge-correlation plot. The graphical cut for all outgoing Ni fragments is shown as example.

located directly behind the target, and offers a good charge resolution. Although the width of the individual charge distributions measured by the TFW is larger, it offers a very useful check for the survival of the fragment up to the last detector of the setup. Figure 5.3 shows the correlation plot for the fragment charge measured in the third PSP and in the TFW. The surviving fragments are selected by an elliptical graphical cut (*cf.* (5.20)) around $Z = 28$, which excludes all background fragments originating from reactions in the detectors and air behind the target, and which form the tail in the TFW charge distribution. No distinct charge distributions can be observed in this tail due to the wrong velocity correction, since it is undefined for fragments produced in the detectors after the target.

Unlike the conditions on the incoming channel, a precise analysis of the portion of good events included by the condition on the outgoing channel is necessary in order to calculate cross sections. Also, the amount of contamination in the elliptical cut should be calculated, such that it can be kept at reasonably low levels. Figure 5.4 shows an example of the treatment of the outgoing charge for a ^{68}Ni non-reacting beam. The left panel shows the charge correlation plot as in figure 5.3 for the non-reacting beam, selected by the appropriate trigger condition. An additional condition on the maximum difference of charge values in both detectors is added ($|Z_{PSP3} - Z_{TFW}| < 1.5$) in order to reduce the influence of the background fragments due to break-up in the detectors behind the target. The center and right panels show the charge distributions in the individual detectors, along with the Gaussian fit functions. The charge resolution values for this example are

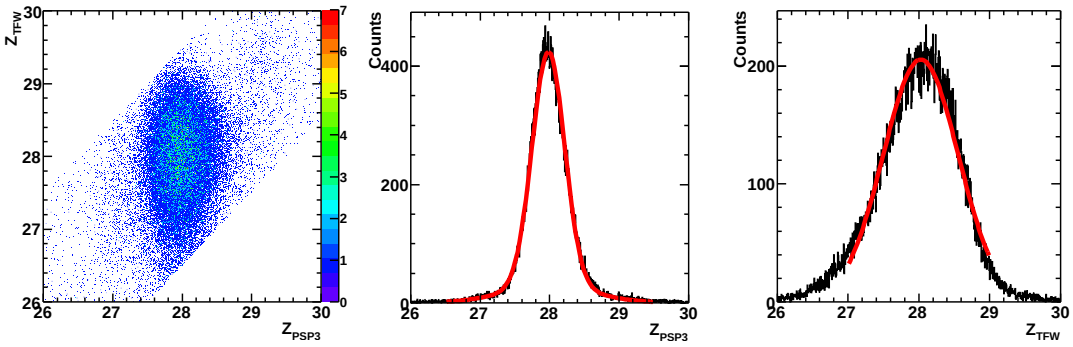

Figure 5.4: Outgoing charge-distribution statistics evaluation for a ^{68}Ni beam on the Pb target. Left panel: charge correlation plot for non-reacting beam, with condition on tolerated charge difference between the two measurements. Center panel: charge distribution in PSP3. Right panel: charge distribution in TFW. The fit functions for the individual charge distributions (red lines) are also shown.

0.234 and 0.533 for the PSP3 and TFW, respectively. The PSP3 distribution requires two Gaussian distributions to take into account the background, as can be seen in the left panel. Due to the greater width of the TFW charge distribution, this component is completely incorporated into the main distribution and therefore cannot be observed. Assuming that the two-dimensional distribution parameters besides the mean values do not strongly depend on the fragment charge, the amount of events enclosed by the graphical cut can be evaluated by randomly generating events according to the Gaussian parameters and by calculating the ratio of counts inside the cut with respect to the total number generated. This simple procedure also allows the simultaneous approximation of the amount of contamination of the neighbor charge distribution, by shifting the elliptical cut by one unit on both charge axes. Since the charge resolution partially depends on the reaction target due to straggling, this procedure must be repeated for each target individually. The cross sections can finally be corrected for the amount of good events that lie outside of the graphical cut.

Fragment Mass

The mass of the fragments can be determined by measuring their deflection in the magnetic field of the ALADIN magnet according to the formalism described in section 4.4. The method used in this analysis requires the measurement of a reference beam, which does not produce fragments. All positions are measured with respect to the track of the reference beam. In order to reduce the error on the mass, the unreacted incoming beam was used as reference beam. Based on the fragment-mass calculation described in subsection 4.4, expression (4.13) is slightly modified in order to remove the spread in

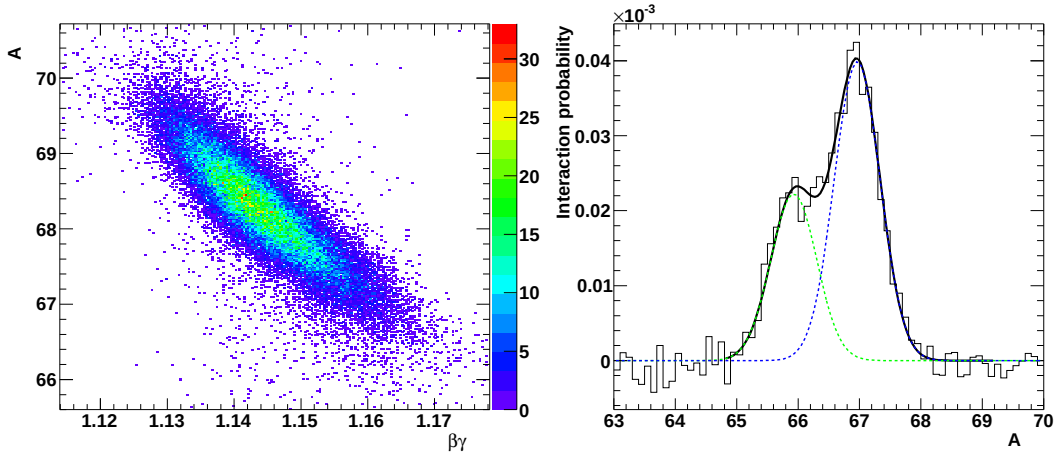

Figure 5.5: Left panel: velocity dependence of fragment mass of a ^{68}Ni beam. Right panel: mass distribution of the ^{68}Ni(γ,n)^{67}Ni channel after velocity correction and background subtraction, for a LAND neutron multiplicity of exactly one. Only the A-1 neighbor distribution is shown since the A+1 peak is absent.

magnetic rigidity:

$$A = A_R \frac{Z}{Z_R}\ \mathrm{dbr}\ \frac{\beta_R\gamma_R}{\beta\gamma}\frac{(B\rho)_{\mathrm{FRS}}}{B\rho} \qquad \text{with}\ \ \mathrm{dbr} = 1 + \frac{d\,(B\rho)}{B\rho_R} \tag{5.24}$$

where the variables with the subscript R correspond to the reference beam and where $(B\rho)_{\mathrm{FRS}}$ is the magnetic rigidity set by the FRS. Due to the higher precision of the FRS magnetic rigidity value, the mass resolution can be improved by including the last fraction of equation (5.24). The tracking formulae only require three position measurements (two on one side of the magnet and one on the other), although two positions before (position in the target and PSP3) and four behind ALADIN (three GFIs and TFW) are available. This redundancy can be used to improve the mass resolution by averaging the calculated masses of independent measurements. The position resolution of the TFW is not sufficient to resolve the masses, and is therefore not used. In order to minimize the mass correlation, mass variables using at most one common detector are chosen: Target+PSP3+GFI2 and PSP3+GFI1+GFI3. It should be noted that the mass resolution is determined by the angular straggling in the middle detector. The experimental mass distribution has a strong velocity dependence, as can be seen in the left panel of figure 5.5. This correlation finds its origin in a non-understood deficit of the tracking procedure and must be corrected for in order to improve the mass resolution. The mass distribution for the ^{68}Ni(γ,n)^{67}Ni channel after the velocity dependence removal and background subtraction is shown in the right panel of the same figure, while requiring

exactly one neutron to be detected in LAND. Although the mass resolution of $\sigma = 0.37$ mass units is obtained, which corresponds to 0.55%, neighboring masses are not fully resolved, which complicates the setting of the mass cut boundaries. As for the fragment charge distribution, the amount of excluded good events and the contamination must be evaluated for each target. The mass distribution $f(A)$ can be well described by three Gaussian distributions:

$$f(A) = \sum_{i=1}^{3} \frac{C_i}{\sigma\sqrt{2\pi}} \exp\left[-\frac{1}{2}\left(\frac{A-\overline{A}_i}{\sigma}\right)^2\right] \tag{5.25}$$

where C_i is the integral and $\overline{A}_i$ is the mean mass of the i-th Gaussian. The width σ should be similar for all masses in the considered mass region, and is therefore a global fit parameter. The integral $D_i(A)$ of each Gaussian can be calculated using the following expression for the integral from $-\infty$ to A:

$$D_i(A) = C_i \frac{1}{2}\left(1 + \mathrm{erf}\left[\frac{A-\overline{A}_i}{\sqrt{2}\sigma}\right]\right) \tag{5.26}$$

The mass cut will be brought into a symmetric position around the fragment mass of the particular outgoing channel, such that it can be defined by two parameters: mean mass $\overline{A}_m$ and half-width $\delta\sigma$. The integral I_m of the A_m mass distribution is given by:

$$\begin{aligned} I_m(\delta\sigma) &= \frac{1}{\Delta x}\left(D_m\left(\overline{A}_m + \delta\sigma\right) - D_m\left(\overline{A}_m - \delta\sigma\right)\right) \\ &= \frac{C_m}{2\Delta x}\left(\mathrm{erf}\left[\frac{\delta\sigma}{\sqrt{2}\sigma}\right] - \mathrm{erf}\left[\frac{-\delta\sigma}{\sqrt{2}\sigma}\right]\right) \\ &= \frac{C_m}{\Delta x}\ \mathrm{erf}\left[\frac{\delta}{\sqrt{2}}\right] \end{aligned} \tag{5.27}$$

where Δx is the bin width of the experimental data, in order to match the Gaussian integral with the bin-wise integral of the histogram. Using a similar development, the contamination of the $m \pm 1$ distribution can be calculated:

$$\begin{aligned} I_\pm(\delta\sigma) &= \frac{1}{\Delta x}\left(D_\pm\left(\overline{A}_m + \delta\sigma\right) - D_\pm\left(\overline{A}_m - \delta\sigma\right)\right) \\ &= \frac{C_\pm}{2\Delta x}\left(\mathrm{erf}\left[\frac{\overline{A}_m + \delta\sigma - \overline{A}_\pm}{\sqrt{2}\sigma}\right] - \mathrm{erf}\left[\frac{\overline{A}_m - \delta\sigma - \overline{A}_\pm}{\sqrt{2}\sigma}\right]\right) \end{aligned} \tag{5.28}$$

When using the mass cut, the resulting cross section must be multiplied by a factor $I_m(\infty)/I_m(\delta\sigma)$, thus taking the excluded good mass entries into account. The mass distribution of the lead target is usually defined as the main distribution, defining the cuts for the other targets. The Gaussian parameters of the distribution are also considered to be identical for all targets. When the quantitative contamination by the neighboring masses is included in the analysis, the interaction probability must be multiplied by:

$$p_{cont}(\delta\sigma) = 1 - \frac{I_+(\delta\sigma) + I_-(\delta\sigma)}{I_m(\delta\sigma) + I_+(\delta\sigma) + I_-(\delta\sigma)} \tag{5.29}$$

$p_{cont}(\delta\sigma)$ is the probability for an event inside the cut boundaries to be a good event.

Velocity Conditions

The proximity of the fragment branch detectors to LAND cause a non-negligible background, produced by the interaction of the fragments with the detectors. If these particles reach LAND while the electronics gate is open, they can be registered as neutrons, since LAND cannot easily identify different particles. The only possibilities to exclude these hits is either to use the Veto wall, or to exclude them with conditions on the measured velocity. Evaporation neutrons reach LAND with velocities close to the beam velocity, while the background hits are usually slower due to the large angles involved. This behavior is shown in figure 5.6, where the neutron velocity is displayed as a function

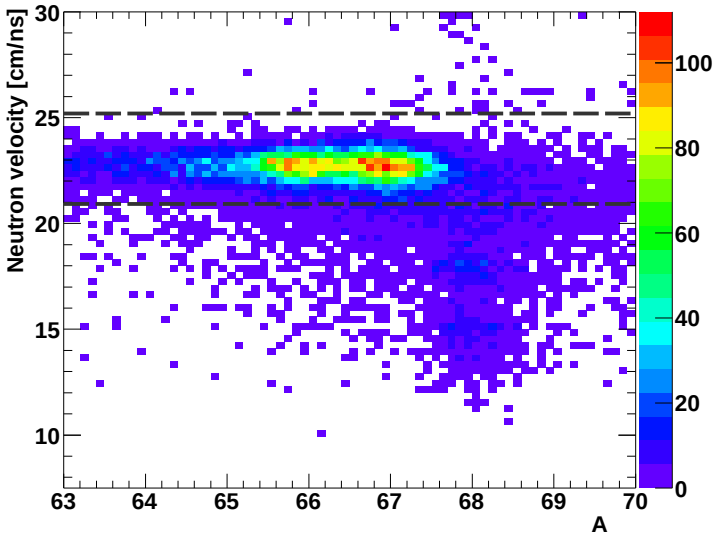

Figure 5.6: Neutron velocity as a function of the reconstructed fragment mass for the ^{68}Ni(γ,n)^{67}Ni channel on the Pb target. The dashed lines shown the limits of the velocity cut.

of the reconstructed fragment mass for the ^{68}Ni(γ,n)^{67}Ni channel on the Pb target. The dashed lines show the limits of the velocity cut, excluding a large fraction of the background events with mass $A = 68$. A short example shows that all neutrons should fall into the velocity window. For a 500 AMeV beam with a velocity window of ± 2 cm/ns, a neutron emitted at 0° with respect to the beam direction having a kinetic energy of 16.1 MeV in the rest frame will reach the upper edge of the velocity window. Alternatively, a neutron emitted at 180° with respect to the beam direction having a kinetic energy of 9.9 MeV in the rest frame will reach the lower edge of the velocity window. As a comparison value, the statistical model used for the present experiment generates neutrons with kinetic energies up to 8-9 MeV, while the distribution typically peaks near 1 MeV. The measured data is not corrected for the acceptance loss introduced by this

condition, which can affect the neutrons originating from the direct decay of the giant dipole resonance.

A similar condition is applied on the fragment velocity, measured by time-of-flight by the TFW. The velocity distribution of the non-reacting beam can be easily measured, and a wide cut (3σ) is applied around the centroid velocity. In the case of peripheral reactions, the change in velocity is small enough such that the distribution is well inside the cut. However, it should be noted that the energy loss in the target and in the detector material of different fragment masses leads to different final velocities, which must all lie inside the condition boundaries.

Other Conditions

When the mass resolution is not sufficient for the identification of the fragment masses, one must rely on the number of neutrons reconstructed in LAND. This procedure, however, misidentifies a significant number of neutron hits. Combining the mass information and the neutron track multiplicity, the mass identification is more efficient. The expected neutron track multiplicity is defined by the mass A and charge Z numbers of the incoming and outgoing channels:

$$\mathrm{Ntmul} = A_{in} - A_{out} - (Z_{in} - Z_{out}) \tag{5.30}$$

If the measured multiplicity matches the expected value, the mass peaks of the contaminants of the selected outgoing channel are partly suppressed, which allows wider mass cuts without a dramatic increase of the contamination.

Chapter 6

Experimental Results

The experimental results obtained from the present experiment on neutron-rich nickel isotopes will be presented in this chapter. The previous chapter explained the main conditions and approximations required to obtain the results of the subsequent sections. The results obtained for ^{58}Ni will first be compared to an earlier measurement using real photons and thus serves as a test case for our experimental method. The differential cross sections obtained for $^{67-69}$Ni will then be discussed with respect to the giant dipole resonance and to eventual low-lying dipole strength. Finally, the results will be compared to calculations and previously published data.

Table 6.1 provides the list of all projectiles used in the analysis of this experiment. The projectile energy is determined with the nominal $B\rho$ value set at the FRS and with the projectile masses [77]. The energy in the middle of the target will later define the projectile rest frame, to which the kinetic energy distributions will be related.

6.1 The ^{58}Ni Test Case

The results of ^{58}Ni will be presented first, a stable nucleus for which data has been published previously. Even though this nickel isotope is not of major interest for the present experiment, it provides the only direct comparison with previously published Giant Dipole Resonance (GDR) data, which is of great interest due to the complexity of the analysis of the present exclusive measurement (discussed in chapter 4). The photoneutron cross sections of ^{58}Ni and ^{60}Ni have been measured at the Lawrence Livermore Laboratory by Fultz and coworkers and published in 1974 [2, 21, 78].

The photoneutron data for the 1n channel is shown in the left panel of figure 6.1. ^{58}Ni is located on the proton-rich side of the valley of β-stability, leading to p, n and np thresholds at S_p = 8.17 MeV, S_n = 12.2 MeV and S_{np} = 19.6 MeV. Due to the experimental conditions, the 1n photoneutron data contains the (γ,n) and (γ,np) channels. The right panel of figure 6.1 contains the same data after conversion to Coulomb

Projectile	$B\rho_{FRS}$ [Tm]	E_{FRS} [AMeV]	Target with thickness [mg/cm^2]	$E_{mid-target}$ [AMeV]
^{58}Ni	7.6412	515.36	Pb 519	500.99
^{58}Ni	7.6412	515.36	C 187	503.05
^{58}Ni	7.6412	515.36	Empty 0	506.18
^{67}Ni	8.9550	527.61	Pb 519	515.29
^{67}Ni	8.9550	527.61	C 187	517.06
^{67}Ni	8.9550	527.61	Empty 0	519.75
^{68}Ni	8.9550	514.92	Pb 519	502.67
^{68}Ni	8.9550	514.92	C 187	504.42
^{68}Ni	8.9550	514.92	Empty 0	507.10
^{69}Ni	8.9550	502.64	Pb 519	490.45
^{69}Ni	8.9550	502.64	C 187	492.19
^{69}Ni	8.9550	502.64	Empty 0	494.85

Table 6.1: List of projectile energies for all targets used in the present analysis. E_{FRS} is the projectile energy at the exit of the FRS, while $E_{mid-target}$ is its energy calculated for the middle of the target. The projectile masses are provided by the atomic mass table [77]. The energies are calculated with ATIMA [71].

excitation cross section for the reaction of ^{58}Ni on a Pb target at a beam energy of 500 AMeV. This distribution is well described by a Lorentzian function, which can be used as a model function.

The Coulomb-excitation data from Fultz *et al.* can be compared to the data measured in this experiment. In the present experiment, however, the reaction channels are well defined. Both (γ,n) and (γ,np) channels must therefore be evaluated separately, and the sum of both Coulomb-excitation cross sections must be compared to the literature result. The comparison of the Coulomb-excitation cross sections is presented in table 6.2,

Data set	σ(1n) [mb]	σ(1np) [mb]	σ(1n+1np) [mb]	Syst. error [mb]
Fultz *et al.*	-	-	123(6)	15
Present experiment	111(4)	25(4)	136(8)	8

Table 6.2: Summary of ^{58}Ni Coulomb-excitation cross sections. The statistical errors are indicated between brackets for each cross-section value. The last row contains the estimated systematical error on the combined 1n+1np cross sections. The mean value for each error source is taken into account for the Fultz *et al.* data.

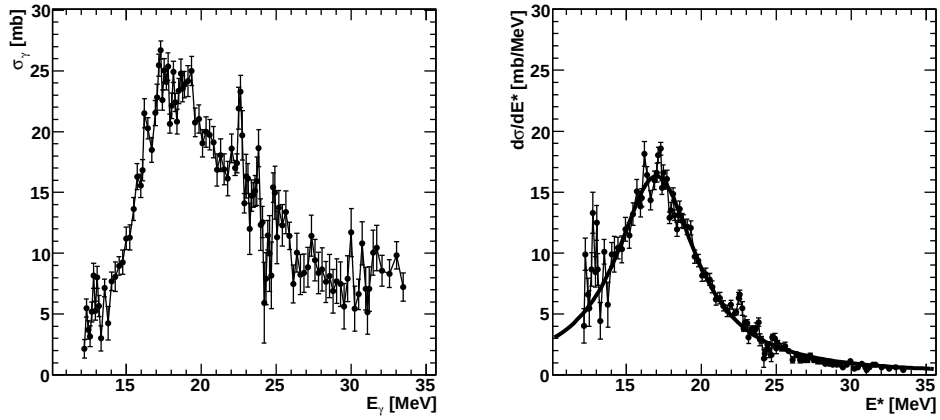

Figure 6.1: Left panel: ^{58}Ni photoneutron cross section from Fultz *et al.* [2,21,78]. Right panel: ^{58}Ni Coulomb-excitation cross section for ^{58}Ni on a Pb target at 500 AMeV, derived from the data presented in the left panel, using a semi-classical calculation. The shown Lorentzian can be used as a model function for the Coulomb-excitation function.

showing a good agreement within the respective errors. Fultz *et al.* report also a series of systematical errors. Since the photons are generated by positron annihilation, the bremsstrahlung subtraction is reported with an error of at most 4%. The error on the photon flux is of the order of 5-10%, and the efficiency of the neutron detector varies from 1% to 5%, depending on the neutron energy. In the present experiment, a systematical error of 6% is attributed to the efficiency correction, originating from a small discrepancy in the neutron-hit distributions of the experimental and simulated data.

6.2 The Neutron-rich $^{67-69}$Ni Isotopes

6.2.1 Neutron Kinetic Energy Distributions

Figure 6.2 shows the kinetic energies of the neutrons in the projectile rest frame for $^{67-69}$Ni. The experimental data has been obtained using equations (5.10) and (5.11) described in subsection 5.3 and is compared to a statistical decay calculation convoluted with the detector response.

As explained in subsection 2.3.2, the evaporation spectra of neutrons is described by a Maxwell distribution, depending in particular on the level-density parameter. Due to the closed $Z = 28$ proton shell of nickel and due to the proximity to the eventual $N = 40$ neutron sub-shell [79–82], the considered nickel isotopes are expected to present smaller level densities than the calculated value from equation (2.36). An ABRABLA calculation [83, 84] has been performed for this purpose, providing the nuclear temperature as a function of excitation energy minus the neutron binding energy for a series of nickel

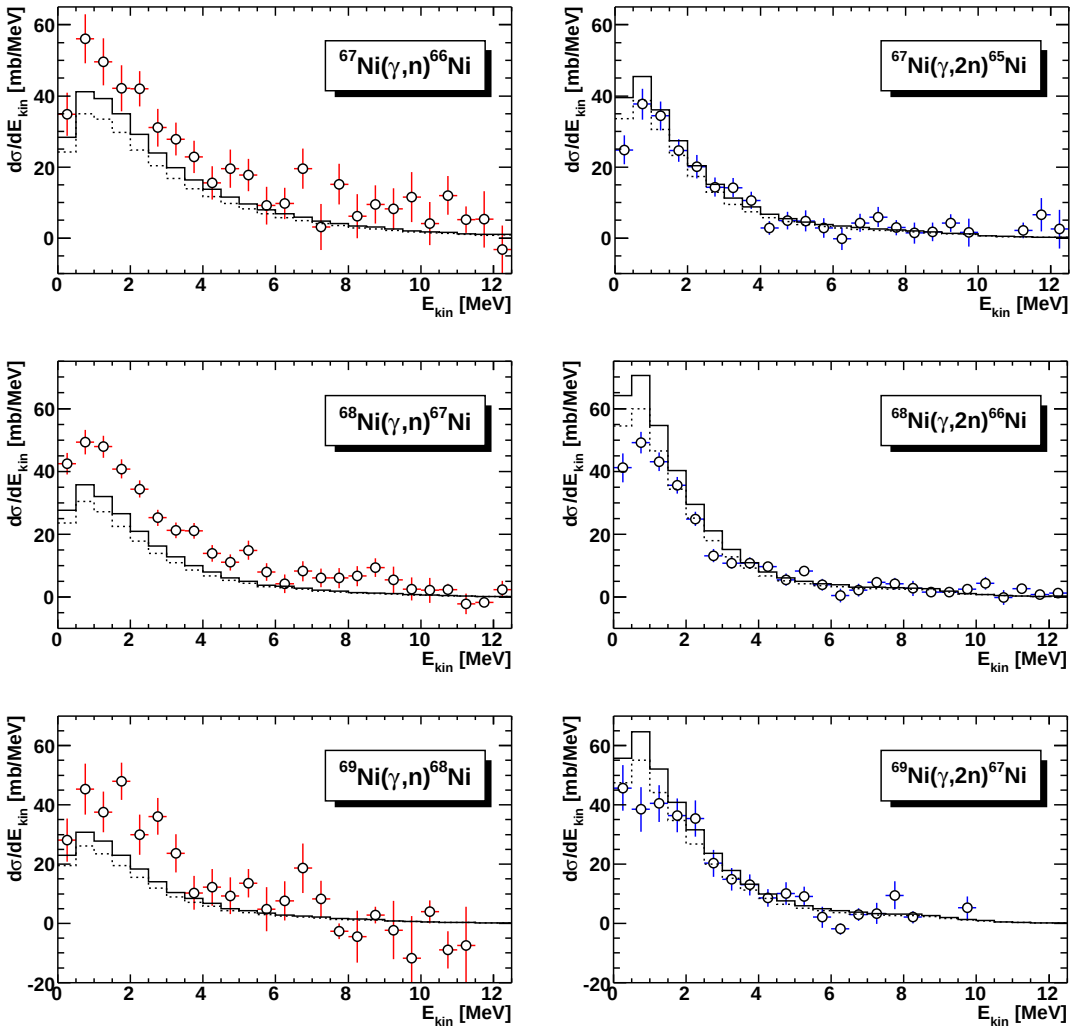

Figure 6.2: Neutron kinetic energy distributions for $^{67-69}$Ni. Left panels: 1n channels. Right panels: 2n channels. The experimental data (points with error bars) is compared to the calculated kinetic energy distributions (from Junghans *et al.* GDR parametrization). Solid line: 100% TRK sum rule. Dotted line: 85% TRK sum rule. A clear excess to the assumed GDR distribution is observed in the (γ, n) channels.

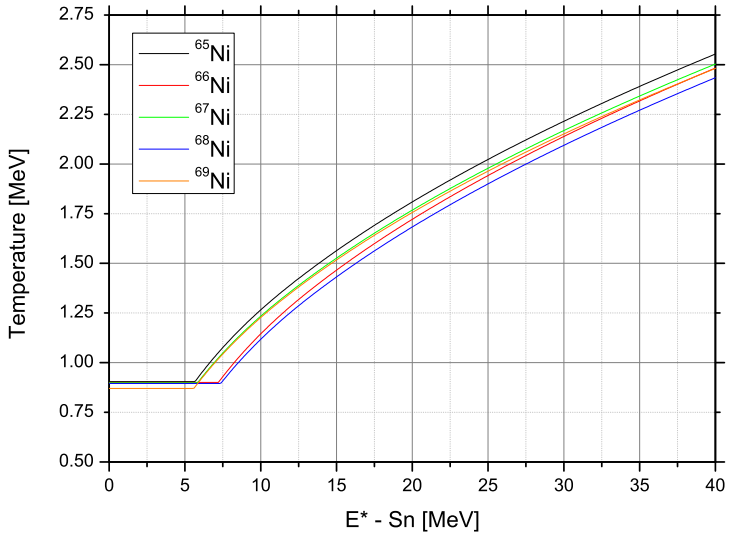

Figure 6.3: Dependence of nuclear temperature on available excitation energy. The curves have been calculated with the constant-temperature model of the ABRABLA code.

nuclei in figure 6.3. These curves have been parametrized for use in the LAND event generator, in order to simulate a realistic statistical decay.

The GDR often is located near or above the two-neutron separation threshold, meaning that a sizable fraction of the total cross section will be observed in the 2n channel. Since the pre-factor of the Maxwell distribution of the kinetic energy spectrum of the emitted neutrons depends on the number of particles emitted (*cf.* subsection 2.3.2), two different distributions must be available in the event generator. The statistical model applied here performs step-wise particle evaporation, meaning that if the excitation energy exceeds the S_{2n} threshold, the total number of evaporated neutrons cannot be determined *a priori*. This dilemma can be partly solved by applying the following condition: if, for the first neutron to be emitted, the excitation energy of the parent nucleus is lower than the S_{2n} threshold, the pre-factor E is applied. In all other cases, the pre-factor $\sqrt{E}$ is used. This only works since the nuclear temperature is relatively small, generating reasonably small neutron kinetic energies. For small E, the difference between the linear and square-root pre-factors is small. Figure 6.4 presents schematically the algorithm used for the statistical decay. An excitation-energy value is first randomly determined according to the E1-strength distribution. If this energy is above the one-neutron threshold, neutrons are evaporated according to a Maxwell distribution using $\sqrt{E}$ or E as pre-factor, as described above. As soon the remaining excitation energy is below the one-neutron-threshold, the energy will be released in a gamma cascade.

The event generator uses the nuclear level structure to determine the possible gamma transitions. Since often only a few levels are known in exotic nuclei, a level-continuum is considered above the last known level. The photon energy in this region therefore depends on the level density. The last gamma transition in the continuum usually is slightly corrected, such that a discrete level can be reached.

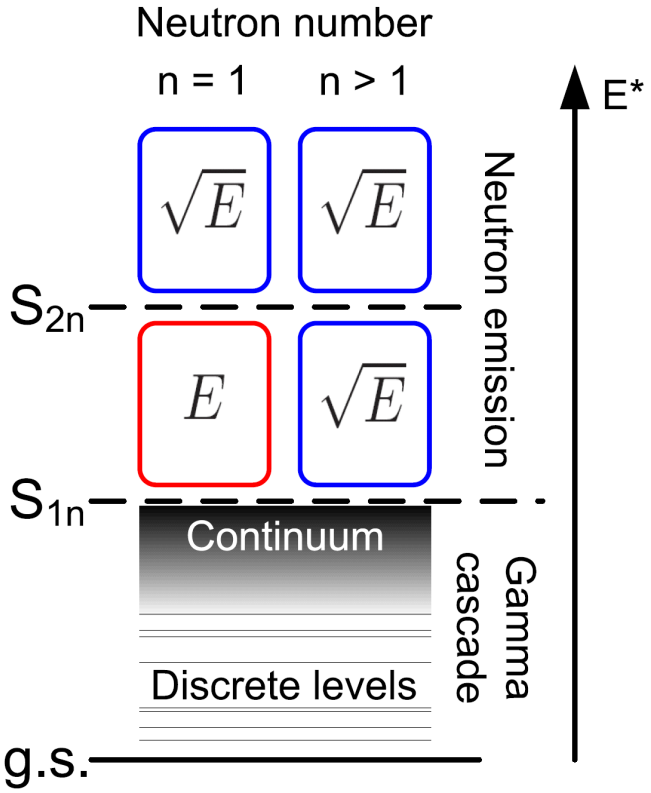

Figure 6.4: Visualization of the algorithm of the statistical-model decay used in the event generator. The pre-factor of the Maxwell distribution of the neutron emission distributions is shown as a function of excitation energy and neutron number. Below the one-neutron-threshold, the excitation energy is released through a gamma cascade, bringing the nucleus to its ground state.

In this and the following subsections, the recent GDR parametrization proposed by Junghans *et al.* [24] is used to describe the GDR of $^{67-69}$Ni. Although the model is valid for nuclei with $A > 80$, the generated GDR distributions of ^{74}Ge, ^{76}Ge, ^{80}Se and ^{82}Se have been compared to experimental data [21], which agree well. Figure 6.5 shows the ^{76}Ge test case, along with the experimental data obtained from Carlos *et al.* [85]. The GDR distributions for $^{67-69}$Ni will be generated with this model, by extrapolating the validity range to this mass region. The peak energies and widths of the GDR distributions depend on the nuclear deformation, which is required as input for the

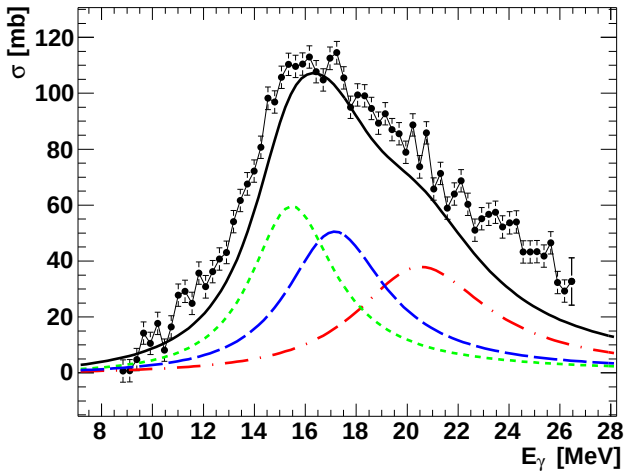

Figure 6.5: Test of GDR parameterization of Junghans *et al.* for ^{76}Ge. The experimental data (black dots) is obtained from Carlos *et al.* [85]. The deformation parameters for the GDR (black line) are $\beta = 0.262$ [86] and $\gamma = 30$ [25]. The dotted green, dashed blue and dashed-dotted red curves are the individual GDR contributions from the three nuclear axes.

calculation. Since the deformation parameters are often not known for unstable nuclei, one must rely on calculated values. The deformation of ^{68}Ni provided by Möller *et al.* is small [25] and generates a GDR distribution barely different from the GDR for a spherical ^{68}Ni nucleus. Figure 6.6 presents the energies of the first 2^+ state in even Fe, Ni and Zn nuclei, showing significantly larger values for ^{56}Ni and ^{68}Ni. In the case of the latter isotope, it is shifted to higher energies by more than 500 keV, *i.e.*, to 2.033 MeV [79, 80, 86] with $B(E2)_{abs} = 255(60)$ e^{2}fm^4 [86, 87]. Therefore, this nickel isotope will be considered to be spherical, along with the neighboring isotopes ^{67}Ni and ^{69}Ni, since the removal or addition of a neutron is not expected to modify the geometry significantly.

The calculations shown in figure 6.2 have been generated with the algorithm described above, and have been scaled to match 100 (solid line) and 85 (dotted line) percent of the Thomas-Reiche-Kuhn sum rule* for a GDR distribution calculated with the parametrization of Junghans *et al.* [24] (*cf.* equations (2.26), (2.27), (2.28) and (2.29), as well as table 6.4). The 85% TRK sum rule kinetic energy distributions and the measured data agree well for the 2n channels, whereas this is not the case for the 1n channels, where a large portion of the observed strength cannot be described by the GDR alone. The calculated 1n distributions cannot be scaled without scaling the 2n

*All sum rule percentage values refer to the entire strength distribution, *i.e.*, taking also the integral below the 1n threshold into account.

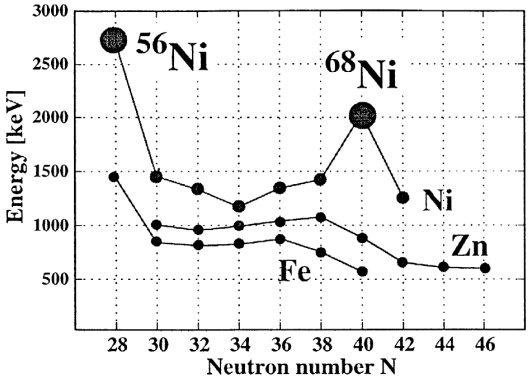

Figure 6.6: First 2^+ state energies of even Fe, Ni and Zn nuclei. From Oros-Peusquens *et al.* [80].

distributions as well, since they are linked by the Lorentzian shape of the GDR and by the branching ratios. Another interesting feature is the small strength excess at 8-9 MeV in the ^{68}Ni 1n distribution, which could be explained by the direct decay of the GDR.

6.2.2 Gamma Spectra

The statistical-decay model used to describe the relaxation of the excited nucleus generates neutrons according to a Maxwell distribution, transferring a significant fraction of the excitation energy to them. When the remaining energy is below the neutron threshold, neutron evaporation stops, forcing the nucleus to relax *via* different channels, *e.g.*, photon emission, internal conversion or internal pair formation. The probability for an internal conversion decay strongly decreases with increasing energy and is only significant for energies lower than the rest mass of the electron (*i.e.*, 511 keV). Also, the internal pair-formation decay becomes significant only at high energies [88], which are not reached in the present experiment. Therefore, gamma decay will be the only relaxation mode considered below the neutron threshold (*cf.* figure 6.4).

The γ-sum-energy spectra are shown in figure 6.7 for each reaction channel separately. Even though the sum energies are shown, some strong gamma transitions are visible, such as the $2^+ \longrightarrow 0^+$ line in ^{66}Ni. The solid line in this figure represents the simulated γ-sum-energy spectrum convoluted with the CsI response, based on the nuclear-level structure provided as input. The detector is intrinsically inefficient, revealing individual strong transitions in the energy-sum spectra, since the probability of missing at least one photon of the cascade is high. The dotted line shows the simulated remaining excitation energy distribution, which would be observed if the gamma detector were a full-efficiency calorimeter. In reality, however, the low efficiency of the CsI detector shifts the energy sum to lower values. Since the individual gamma photons trigger several

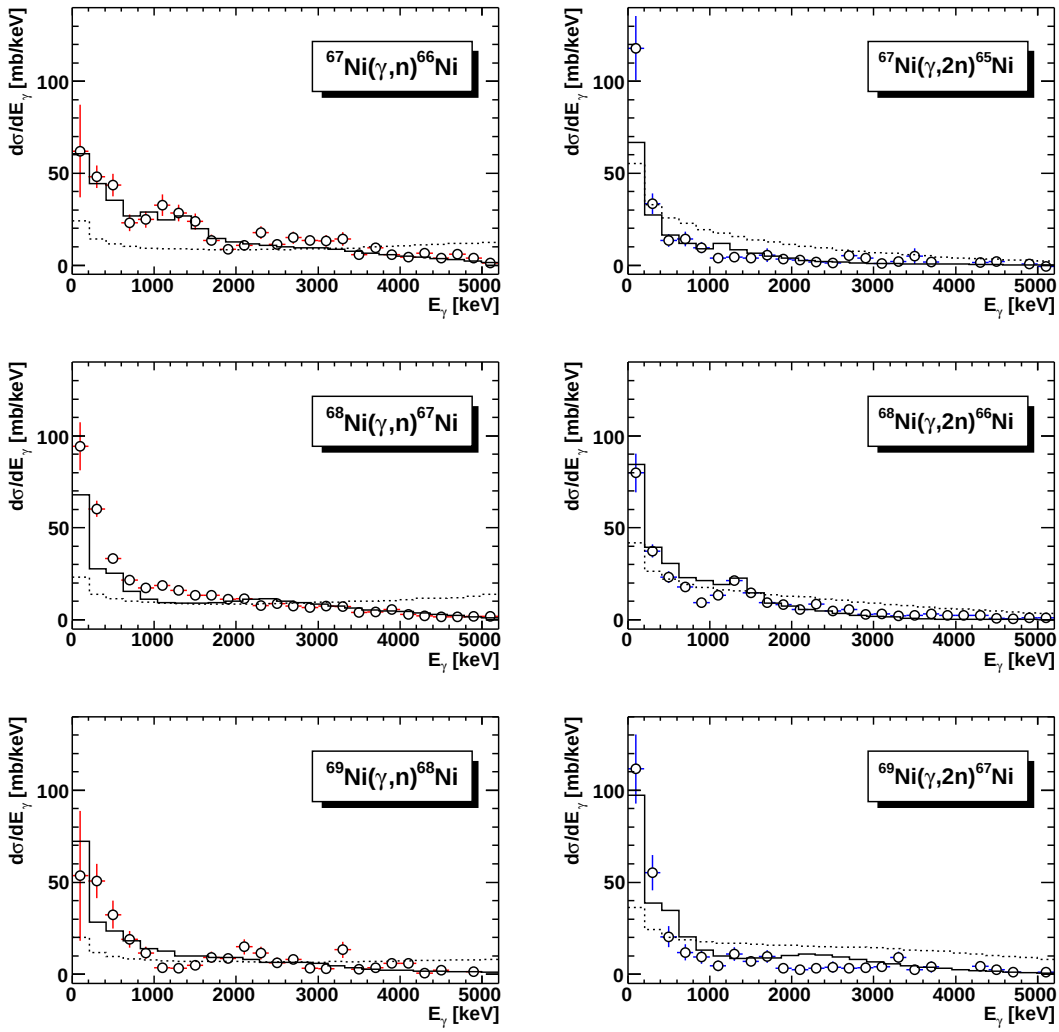

Figure 6.7: Gamma-sum spectra for $^{67-69}$Ni. Left panels: 1n channels. Right panels: 2n channels. The experimental data (points with error bars) is compared to the calculated gamma-sum spectra (solid line), using the Junghans *et al.* GDR parametrization with 100% TRK sum rule. The dotted line shows the simulated remaining excitation energy.

CsI crystals in a so-called cluster, the γ-sum-energy spectra are reconstructed using the cluster mode. The energies of the individual crystals in the cluster are summed before being Doppler-shifted with the angle of the crystal presenting the highest energy. This procedure provides cleaner spectra than a simple Doppler-shifted sum of all crystals. However, the photon background of atomic origin can be easily subtracted only for the sum of all 144 CsI crystals, since precise knowledge of the angular distribution of the background is required for its event-wise subtraction in the cluster method. The energy

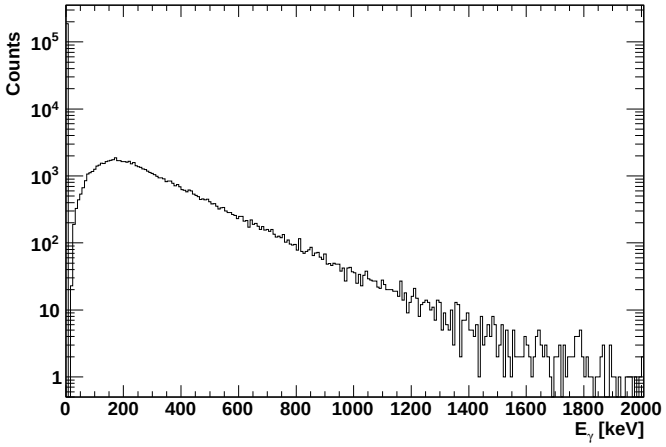

Figure 6.8: γ-sum-energy spectrum for photons of atomic origin. The distribution has been obtained in coincidence with the minimum-bias trigger only.

distribution of the background is shown in figure 6.8, which peaks at 200 keV and decreases exponentially up to 2 MeV. This atomic background has been measured with non-reacting beam (*i.e.*, Tpat=1) and without using the clustering method. For 75% of the events, no background is measured, since a threshold of 50 keV in the laboratory frame has been applied to each crystal before building the energy sum. With a bin width of 200 keV for the γ-sum-energy spectra, the background can be neglected as a first-order approximation. An energy of a few hundred keV (mean value of the background spectrum in figure 6.8) will be subtracted only from every fourth event, therefore mainly smearing the spectrum to slightly lower energies. In all reaction channels, the experimental data is compared to a convoluted GDR distribution from the systematics of Junghans *et al.* [24] with 100% TRK sum rule (solid line).

^{65}Ni

Since ^{65}Ni is an even-odd nucleus with a large level density, a large number of gamma transitions with relatively small energies is expected. Due to the partial inefficiency of the gamma detector, there is a large probability of missing one or more transitions,

removing the structures of an already very broad spectrum.

^{66}Ni

The level structure of ^{66}Ni predicts a very strong transition at 1.42 MeV ($2^+ \rightarrow 0^+$) that should be observed in all gamma cascades. This transition is contained in a very broad structure in the ^{67}Ni(γ,n)^{66}Ni channel – however well described by the folded GDR distribution –, while in the ^{68}Ni(γ,2n)^{66}Ni channel a peak is seen at the expected transition energy.

^{67}Ni

The ^{67}Ni case is somewhat similar to ^{65}Ni, since no clear structures are to be seen. Even though the nucleus is even-odd, the number of known levels is fairly small. Also, the two lowest excited levels are isomeric states, the first one at 694 keV with a half-life of 150 ps and the second one at 1007 keV with a half-life of 13.3 μs. While the latter level is clearly too long-lived to be observed in-flight, the former is more complicated to treat. With a beam energy of approximately 514 AMeV, the fragment travels 3.4 cm in one half-life, meaning that the probability for this state to decay inside the gamma detector is nearly 100%. If the gamma photon does not originate from inside the target, which is quite likely with the given half-life, the rest-frame energy will not be reconstructed correctly, since false angles will be provided for the Doppler shift. The event generator does not take the half-life of this level into account, creating a discrepancy between the data and the simulation for this particular level, as well as the levels in the subsequent gamma cascade. The difference will, however, be hardly visible, due to the limited resolution and efficiency of the detector.

^{68}Ni

Similar to ^{66}Ni, ^{68}Ni has a 2^+ state at 2.03 MeV. Most gamma cascades contain this $2^+ \rightarrow 0^+$ transition, creating a peak in the experimental data around 2 MeV. A minor amount of cascades will fall into an isomeric 0^+ state at 1.77 MeV with a half-life of 276 ns.

6.2.3 Excitation-energy Distributions

One of the main goals of the nickel experiment is the measurement of the excitation function, especially in order to draw conclusions on the presence or absence of low-lying dipole strength. The excitation-energy distributions for $^{67-69}$Ni are calculated using equation 5.19, using both the 1n and 2n channels. In most cases, the 3n channel is negligible, since the threshold is high compared to the energies obtained in the virtual

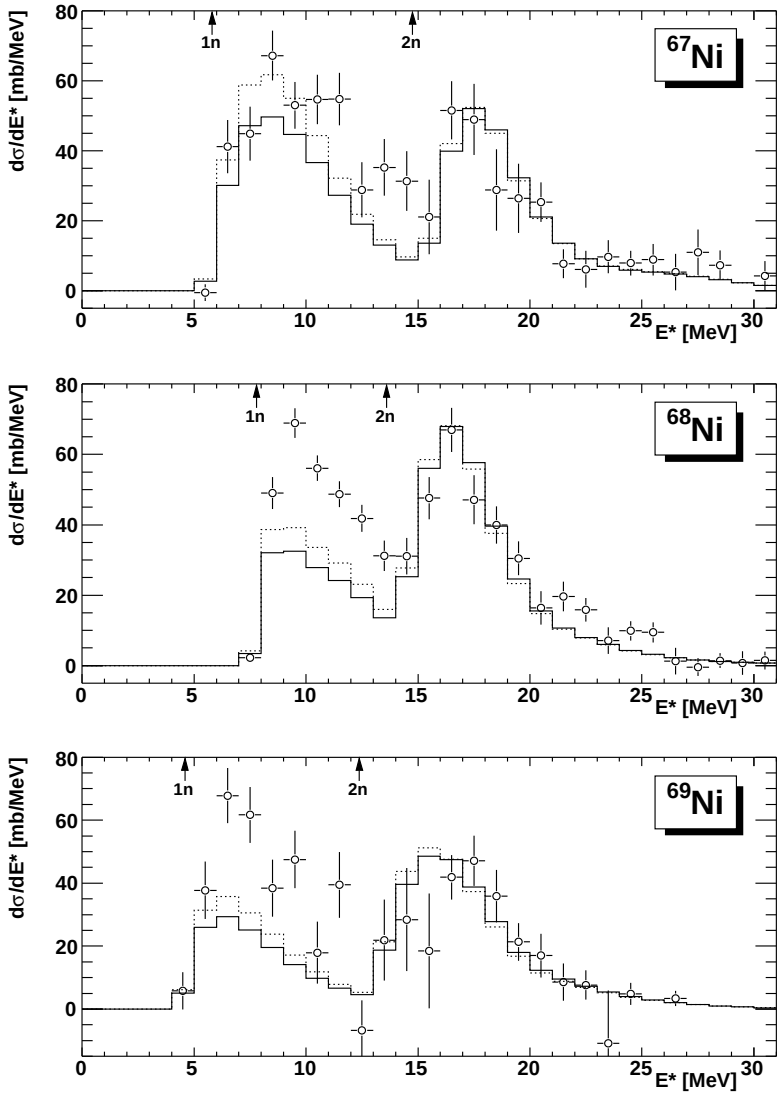

Figure 6.9: Coulomb excitation functions for $^{67-69}$Ni. The histograms with the solid and dotted black lines represent the GDR convoluted with the experimental response using GDR parameters from Junghans *et al.* [24] and from systematics [1], respectively. The maxima and widths of the GDR distributions have been fixed according to the previously cited models, while the strength has been adjusted with a χ^2 minimization.

photon spectrum. Figure 6.9 presents the experimental Coulomb excitation-energy distributions for ^{67}Ni, ^{68}Ni and ^{69}Ni. The double-peak structure partly arises from the detector response: due to the inefficiencies of the gamma detector (*cf.* subsection 4.5.3), the observed invariant mass is smaller than expected. Excitation energies of an xn decay channel near the (x+1)n threshold are particularly sensitive to the gamma detection efficiency, since a significant amount of energy of the de-excitation process will be conveyed by photon emission. As the level density increases with excitation energy, the upper portion of the gamma cascade will be dominated by statistical transitions for large total gamma energies. Statistical gamma transitions have a continuous probability distribution, which normally peaks at 1-2 MeV, meaning that the cascade will possibly contain several gamma transitions. If the gamma detection efficiency is significantly lower than unity, the probability of missing at least one transition is large, therefore shifting the invariant mass to lower values. The excitation-energy distribution peaks at the neutron thresholds for this reason. This shift can be observed in the γ-sum-energy spectra in figure 6.7: the remaining excitation energy is uniformly distributed over the entire energy range, whereas the measured gamma sum is strongly shifted to low values. The double-peak feature makes the quantitative evaluation of low-lying strength more difficult, since the GDR and Pygmy Dipole Resonance (PDR) distributions overlap even more.

^{A}Z	σ_{1n} [mb]	σ_{2n} [mb]	S_n [MeV]	S_{2n} [MeV]
^{67}Ni	467(31)	224(21)	5.808	14.76
^{68}Ni	386(16)	263(14)	7.792	13.60
^{69}Ni	287(39)	267(25)	4.586	12.38

Table 6.3: Measured Coulomb excitation cross sections for $^{67-69}$Ni on Pb at approximately 500 AMeV. The indicated errors are purely statistical. The neutron thresholds are provided by the atomic mass table [77].

Table 6.3 presents the measured Coulomb excitation cross sections for the 1n and 2n decay channels of $^{67-69}$Ni at approximately 500 AMeV and on a Pb target, with their respective statistical errors. In order to compare these results with model calculations, several assumptions are required, such as the model strength distribution, the branching ratios of the various decay channels and the amount of contamination in each channel. This information is processed in the fitting stage of the analysis, the results of which will be presented later in this section.

Statistical-decay calculations can generate branching ratios for the various decay channels. In figure 6.10, the statistical decay of the LAND event generator (LEG) has been adapted to the more accurate model of the ABRABLA code [83,84]. The LEG and

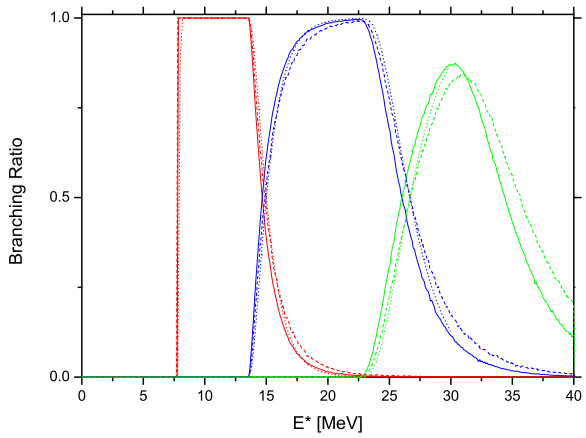

Figure 6.10: Branching ratios for 1n (red lines), 2n (blue lines) and 3n (green lines) channels of ^{68}Ni. Solid lines: branching ratios generated by the statistical decay model of the LAND event generator (LEG). Dotted lines: branching ratios generated by the statistical decay model of the ABRABLA code. Dashed lines: branching ratios generated by a GDR code using level densities as input. The LEG information stops at 30 MeV.

ABRABLA data sets do not describe the branching near the 1n threshold properly due to the fact that only the neutron decay mode is considered. At small excitation energy values above the 1n threshold, de-excitation by photon emission remains a major decay channel due to the small phase space accessible to the neutron. The 1n branching ratio must therefore be modified to describe this behavior. The LEG branching ratio has been modified manually up to the excitation energy of S_n+2 MeV to match the experimental data in this region.

In order to extract the eventual PDR strength of $^{67-69}$Ni, the GDR portion of the distribution must be identified first. Since the giant resonances of the considered nickel isotopes have not been measured before, two methods can be applied to extract the desired information: fitting the data with an appropriate distribution describing the GDR and the PDR, or calculating the GDR parameters using existing models. The first approach requires a fairly simple detector response and experimental data with reasonably small statistical errors. These requirements are necessary to reduce the number of local minima accessible during the minimization stage of the fitting. If the detector response is too complex, the fit results will not converge properly. In the present case, the detector deficiencies of LAND and the ring efficiencies of the CsI gamma detector yield a strongly hampered response. Also, due to the limited amount of experimental data available, the statistical error is relatively large. Due to these reasons, the second approach will be used.

	Junghans *et al.* [24]				Systematics			
^{A}Z	E_m [MeV]	Γ [MeV]	% of S_{TRK} [-]	χ^2_ν [-]	E_m [MeV]	Γ [MeV]	% of S_{TRK} [-]	χ^2_ν [-]
^{67}Ni	18.20	5.19	92(9)	1.56	17.90	5.71	98(9)	1.39
^{68}Ni	18.17	5.17	91(5)	2.12	17.84	5.69	93(5)	2.29
^{69}Ni	18.14	5.16	78(8)	0.83	17.78	5.66	79(8)	1.10

Table 6.4: Giant dipole resonance fit parameters for $^{67-69}$Ni. The fit range was chosen to cover only the 2n decay channel to exclude any influence of low-lying strength.

Table 6.4 presents the results of the fits of the GDR in figure 6.9. The GDR fit is performed above the 2n-threshold only, since the GDR and the low-lying-strength distributions are entangled in the 1n-channel. The S_{2n} threshold is high enough to exclude PDR contributions in the 2n-decay channel. The GDR is therefore fixed with the 2n-decay data, while being also plotted in the 1n-decay region. The Junghans *et al.* parametrization uses equations (2.27), (2.28) and (2.29) to calculate the peak energy, width and strength of the GDR distribution, respectively. For the systematics, equations (2.20), (2.23) and (2.24) were used. It should be noted that the GDR strength value corresponds to the full integral of the photoabsorption cross section. The former parameterization is based on the Finite Range Droplet Model and is able to take the nuclear deformation into account, while the latter is based on the Jensen-Steinwedel and Goldhaber-Teller hydrodynamical models. Since the nuclei in the vicinity of ^{68}Ni are not expected to present a large deformation, the GDR is described by only one Breit-Wigner distribution. Although the GDR parameter differences between the two models are small, the first model systematically generates narrower GDR widths at higher peak energies than the second.

The large statistical error on the data does not allow precise values for the amount of exhausted sum-rule strength. In contrast to the ^{67}Ni and ^{68}Ni cases, the cross section for ^{69}Ni is significantly lower than predicted by the TRK sum rule. There is no apparent reason for this behavior, since 100% sum-rule strength is expected for nuclei in this mass region [1]. Detector acceptance effects can be ruled out due to the fact that all three nuclei originate from the same cocktail beam. Also, no significant cuts in the position distributions for the selected reaction channel are observed in the tracking detectors. The relatively small amount of data for this channel, however, yields a large statistical error. The χ^2_ν value for the GDR strength fit is also very small, pointing out either that the fitting function contains too many free parameters, or that the statistical error on the data is too large [89].

In order to evaluate the pertinence of the various parameter sets, a χ^2_ν mapping of

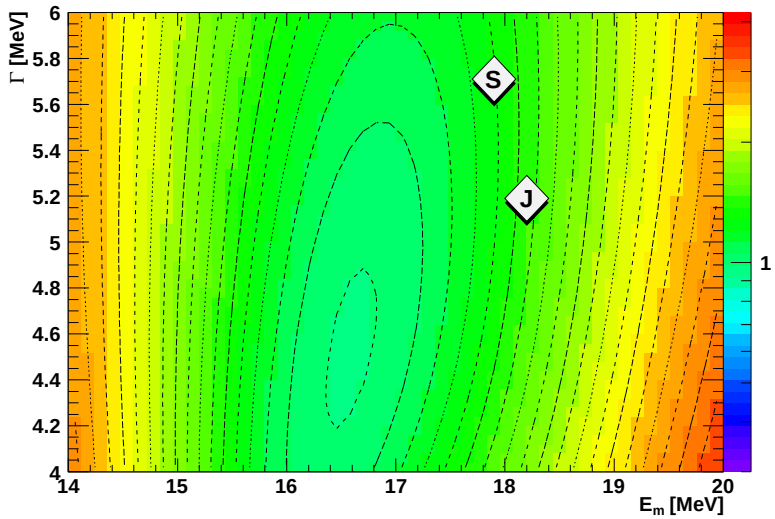

Figure 6.11: ^{67}Ni χ^2_ν mapping of GDR variables. The color scale represents the χ^2_ν value for a given parameter set. The GDR strength for this plot is set to 94%, which is close to the optimum value obtained by minimization (*cf.* table 6.4). The data sets of the Junghans *et al.* and systematics parametrizations are labelled by J and S, respectively, and lie within $\Delta\chi^2_\nu \leq 1$ around the minimum.

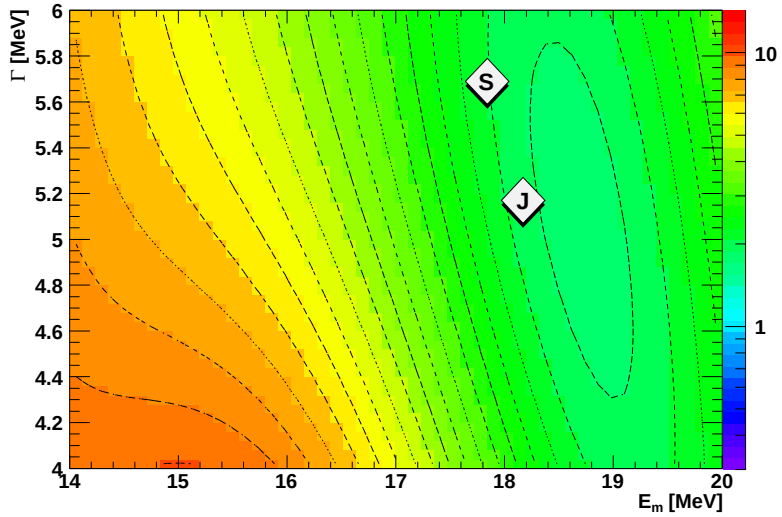

Figure 6.12: Same as fig. 6.11, but for ^{68}Ni and a GDR strength of 91% TRK sum rule strength.

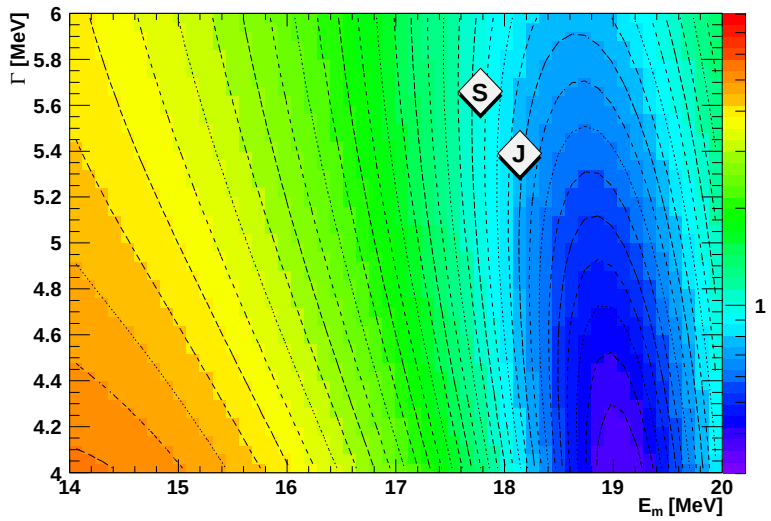

Figure 6.13: Same as fig. 6.11, but for ^{69}Ni and a GDR strength of 79% TRK sum rule strength.

the GDR parameter space can be performed. By varying systematically all three GDR parameters one-by-one, the χ^2_ν values for each parameter set are calculated and inserted into a three-dimensional histogram, which, in the end, is presented as an array of two-dimensional contour plots. The maps for $^{67-69}$Ni are shown completely in appendix A. In all three cases, a fairly wide minimum is observed. Depending on the GDR strength, this minimum can shift considerably in peak energy and width: all three parameters are therefore strongly correlated. Figures 6.11, 6.12 and 6.13 show the parameter maps for the GDR strength values closest to the value obtained from minimization to the experimental data. The two GDR parameter sets are labeled on these figures by J and S for the Junghans *et al.* and systematical parameterizations, respectively. These two parameter sets lie within one sigma of the minima in all three isotopes. In all three cases, the region of minimum χ^2_ν extends over very wide peak energy, width and strength ranges, which illustrates the difficulty to extract a GDR parameter set with sufficient precision from the measured data. This confirms the necessity of using GDR models to calculate some of the parameters.

6.2.4 Excess E1 Strength

The excess dipole cross section in the 1n-decay channel can be extracted from the experimental data by subtraction of the GDR distribution (subsection 6.2.3) as determined by the fit to the 2n-decay cross section. The subtraction is best performed on the excitation-energy distributions, although some information can also be obtained from the integral values. The remaining distribution can be integrated to a Coulomb excitation cross

section, listed in table 6.5. The distribution of excess cross section, however, allows in principle the extraction of the distribution parameters, such as peak energy, width and strength after conversion to photoabsorption units. Since the Coulomb cross-section distribution is convoluted with the detector response, the expected photoabsorption distribution must be passed through the experimental filter, as has also been done for the GDR distributions. Figure 6.14 shows the remaining Coulomb strength after subtraction of the giant dipole resonance. The GDR parameters of the Junghans *et al.* parametrization in table 6.4 have been used. The cross-section excess is attributed to the pygmy dipole resonance (PDR) and a Gaussian distribution will be used for its description, as performed for the Sn case [6, 7, 90, 91]. The solid line in figure 6.14 represents the fit result of the PDR distribution, for which no parameter set has been fixed *a priori*. The observed PDR distributions are extremely wide, which enhances the overlap with the GDR distributions. Again, the limited gamma-detection efficiency pushes the distribution towards the 1n threshold. Taking these effects into account while convoluting the input distribution with the detector response, the excess strength is fairly well described by a realistic set of Gaussian parameters for the ^{68}Ni and ^{69}Ni cases. The minimization of the parameters of ^{67}Ni does not converge towards realistic values, and therefore the fit result will not be discussed here. The Gaussian peak energy E_m, width σ_{Gaus} and strength are summarized in table 6.6. As for the GDR results, the PDR strength represents the full integral of the photoabsorption cross section. The pygmy dipole resonance of ^{68}Ni has been observed near 11 MeV with a width of less than 1 MeV in another experiment [8]. This is, however, not observed with the Gaussian fit of the excess cross section (table 6.6). As for the GDR, the PDR parameter space has been mapped for $^{67-69}$Ni. The complete maps are shown in figures A.4, A.5 and A.6 in appendix A. Four χ^2_ν maps near the expected PDR strength values have been chosen for each nickel isotope in figures 6.15, 6.16 and 6.17. In the case of ^{67}Ni, the mapping in figure 6.15 illustrates the lack of a minimum in a realistic parameter region. Already at low PDR strength values, the minimum of the peak energy lies outside the chosen range. If the strength is increased, the peak energy shifts to higher values, which explains the failure of the fit algorithm to find an appropriate parameter set. The mapping of the PDR of ^{68}Ni shows

^{A}Z	σ_{excess} with Junghans *et al.* GDR [mb]	σ_{excess} with systematics GDR [mb]
^{67}Ni	146(44)	83(45)
^{68}Ni	168(31)	139(31)
^{69}Ni	127(51)	94(52)

Table 6.5: Excess Coulomb-excitation cross sections for $^{67-69}$Ni after subtraction of the GDR with parameters of table 6.4. The indicated errors are purely statistical.

^{A}Z	PDR with Junghans *et al.* [24] GDR				PDR with systematics GDR			
	E_m [MeV]	σ_{Gaus} [MeV]	% of S_{TRK} [-]	χ^2_ν [-]	E_m [MeV]	σ_{Gaus} [MeV]	% of S_{TRK} [-]	χ^2_ν [-]
^{68}Ni	13.0(3)	1.3(3)	9.6(1.3)	2.26	13.0(4)	1.1(3)	7.5(1.1)	2.40
^{69}Ni	11.9(1.0)	0.4(2.2)	9(17)	1.22	11.96(19)	0.3(2)	15(32)	1.35

Table 6.6: Pygmy Dipole Resonance strength for GDR parameter sets of table 6.4. The error values are purely statistical and are given by the minimization routine.

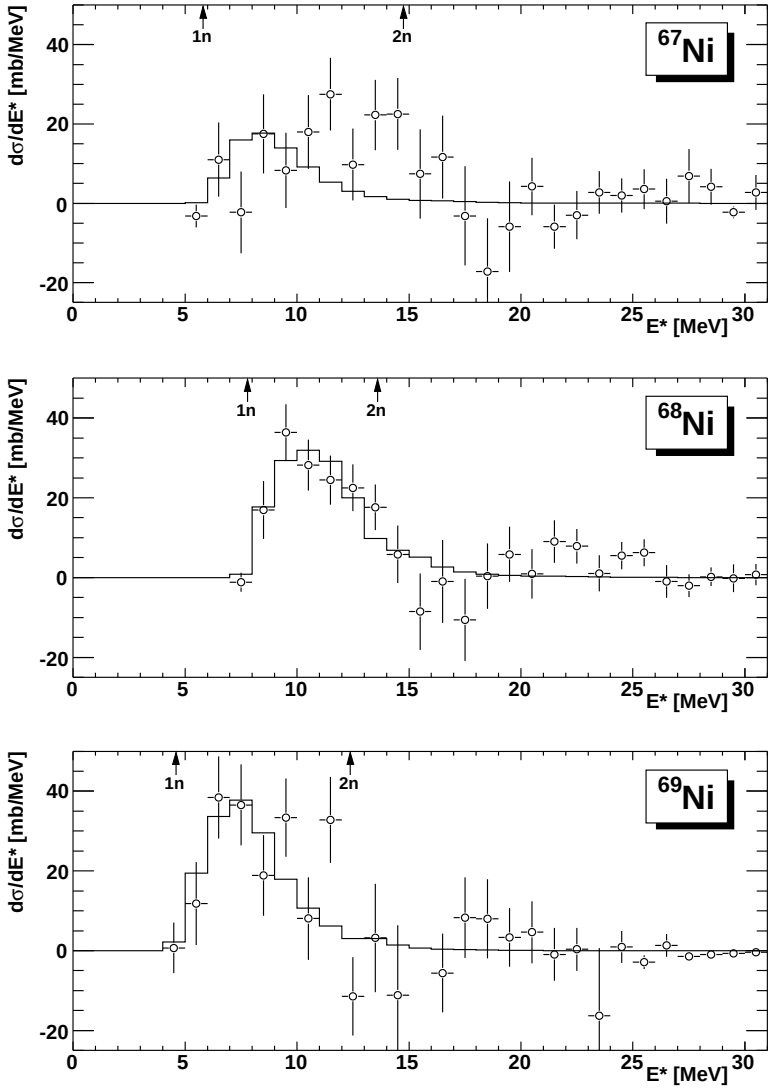

Figure 6.14: $^{67-69}$Ni Coulomb-excitation cross-section excess after subtraction of GDR. A Gaussian distribution for the pygmy dipole resonance has be adjusted by χ^2 minimization to the distribution.

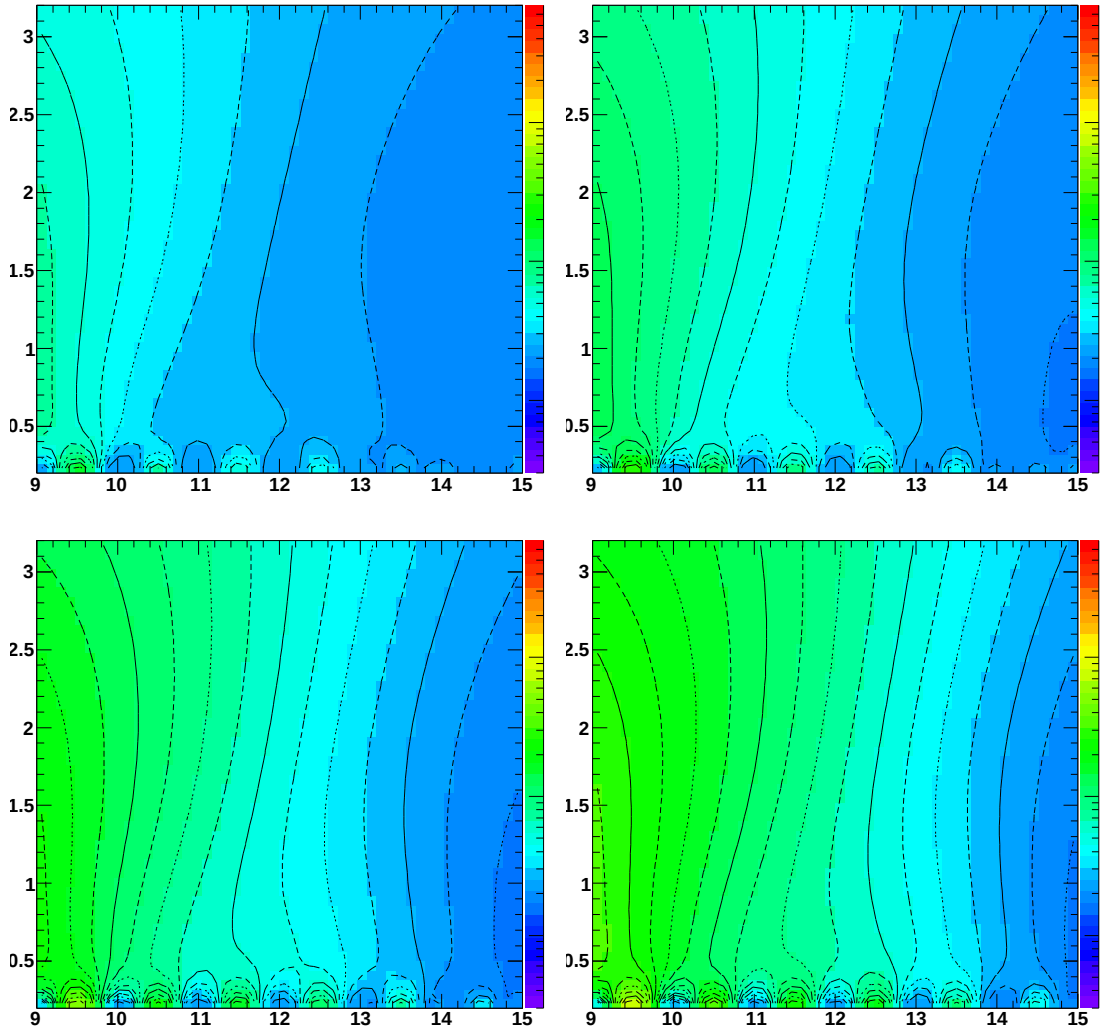

Figure 6.15: χ^2_ν mapping of PDR variables for ^{67}Ni. The color scale represents the χ^2_ν value for a given parameter set. The GDR has been fixed to the parameter set of table 6.4. The four contour plots represent, from top left to bottom right, 5%, 7%, 9% and 11% TRK sum-rule strength, respectively. The PDR peak energy and width are represented on the horizontal and vertical axes, respectively. The χ^2_ν scale ranges from 0.3 (violet) to 600 (red).

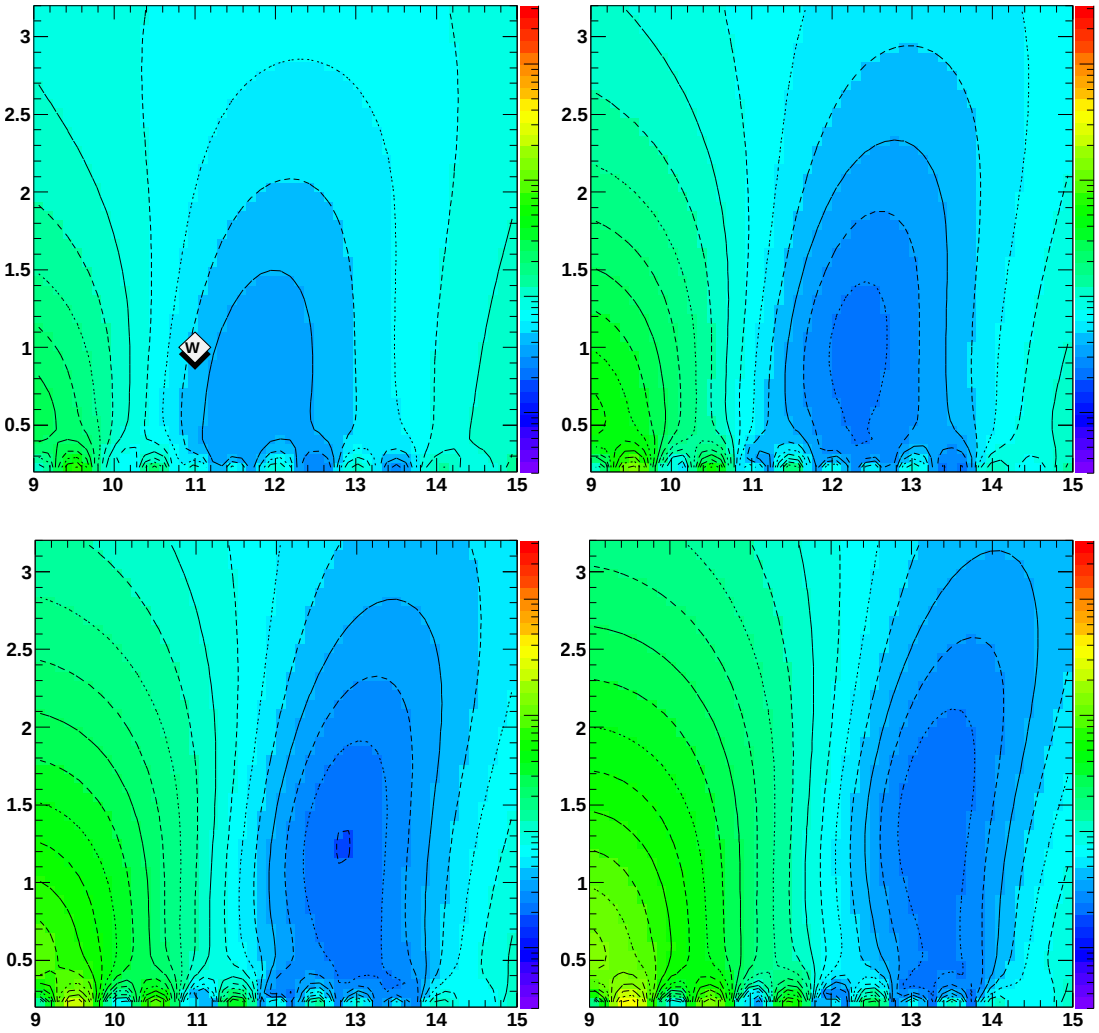

Figure 6.16: χ^2_ν mapping of PDR variables for ^{68}Ni. The color scale represents the χ^2_ν value for a given parameter set. The GDR has been fixed to the parameter set of table 6.4. The four contour plots represent, from top left to bottom right, 5%, 7%, 9% and 11% TRK sum-rule strength, respectively. The PDR peak energy and width are represented on the horizontal and vertical axes, respectively. The χ^2_ν scale ranges from 0.4 (violet) to 3000 (red). The label in the 5% map indicates the PDR parameter set measured by Wieland *et al.* [8], which lies well within the $\Delta\chi^2_\nu \leq 1$ region around the minimum.

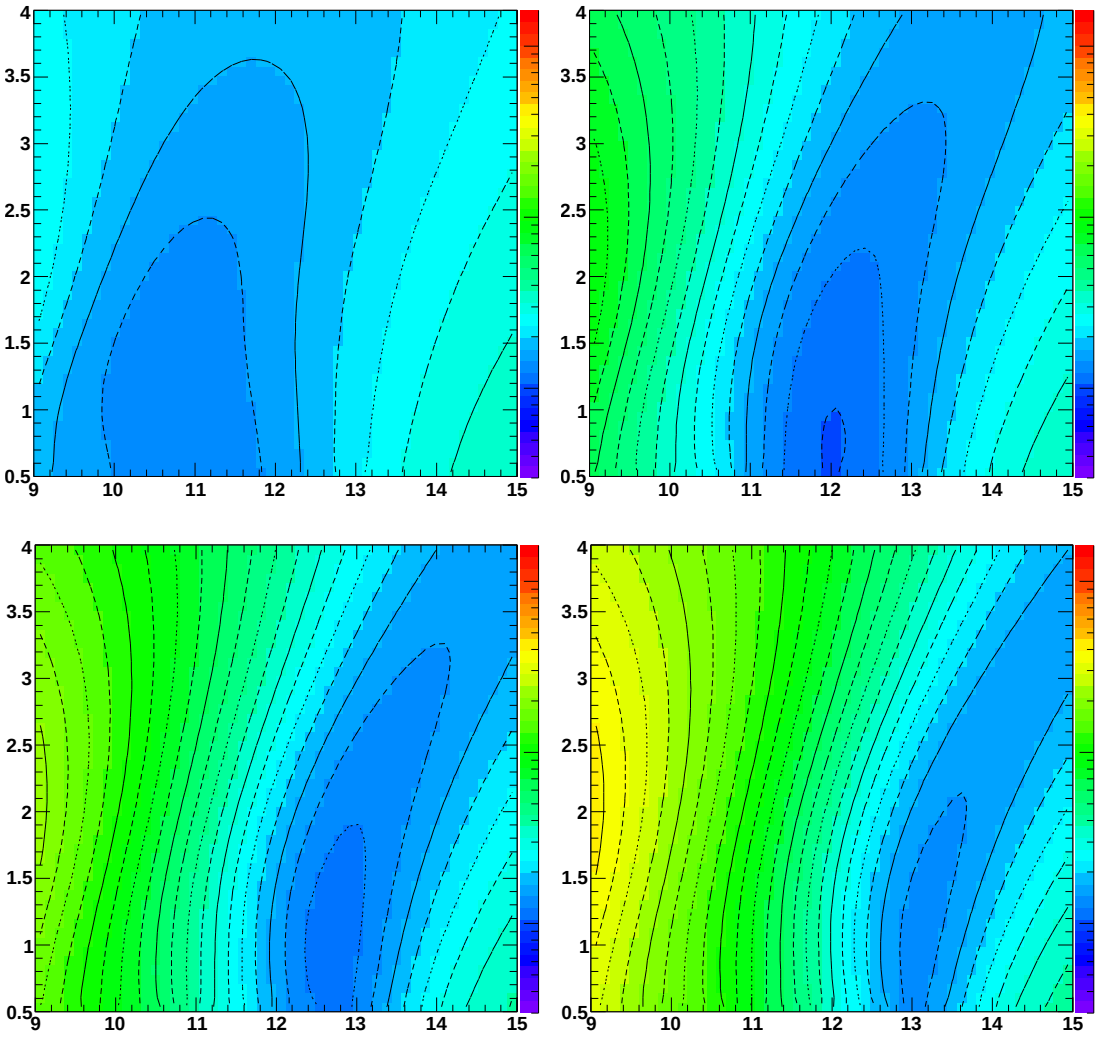

Figure 6.17: χ^2_ν mapping of PDR variables for ^{69}Ni. The color scale represents the χ^2_ν value for a given parameter set. The GDR has been fixed to the parameter set of table 6.4. The four contour plots represent, from top left to bottom right, 5%, 9%, 13% and 17% TRK sum-rule strength, respectively. The PDR peak energy and width are represented on the horizontal and vertical axes, respectively. The χ^2_ν scale ranges from 0.3 (violet) to 100 (red).

a clear minimum in the 9% TRK sum rule plot of figure 6.16, which corresponds to the optimum value obtained by minimization. The PDR result reported by Wieland *et al.* [8] is also shown and lies well within one sigma of the obtained minimum. However, since the results are provided without error estimates, a quantitative comparison of both findings is difficult. The minimization result for ^{69}Ni is also well illustrated by the 9% map of figure 6.17. The strength value should, however, be considered critically, since the observed GDR strength strongly deviates from the 100% TRK sum rule value.

6.3 Discussion

In section 6.1, the measurement of the integral cross sections of ^{58}Ni has been used to confirm the accuracy of the analysis method of the present experiment. As shown by the results of ^{58}Ni, the obtained cross section agrees well with the previous measurement of Fultz *et al.* [2, 78] within the respective errors. Large systematic deviations of the results for the $^{67-69}$Ni isotopes can therefore be considered as unlikely. However, the measurement of the E1 strength distribution of ^{58}Ni is not conclusive. Although this nickel isotope does not present any low-lying E1 strength due to its small isospin, the excitation function measured by neutron decay in the cited references is very wide and strongly asymmetric, and cannot be described correctly by a Lorentzian distribution. The main reason is the low proton emission threshold at $S_p = 8.17$ MeV, which is well below the neutron threshold of $S_n = 12.22$ MeV [77]. Although proton emission is hindered by the Coulomb barrier when compared to neutron emission, the entire E1 strength up to the neutron threshold is carried by the proton channel alone. This explains the small percentage of sum-rule strength observed in the neutron data. The width of the excitation-energy distribution measured by Fultz *et al.* is influenced by the contamination of the (γ,np) decay channel, which could not be distinguished from the neutron-decay channel due to the experimental conditions. The np channel opens at $S_{np} = 19.55$ MeV [77], which indicates that the data of Fultz *et al.* [78] is exclusive only between the n and np thresholds. In the present experiment, the integrated cross section carried by the (γ,np) channel is obtained by measuring the charge and mass of the participating species. In conclusion, the goal for the ^{58}Ni measurement was reached, since the cross-section values of this experiment overlap well with the previously measured data.

For the case of the $^{67-69}$Ni isotopes, the proton channel can be safely neglected. The GDR of these isotopes has not been measured before, and therefore one must rely either on the present data or on calculations. The presence of low-lying E1 strength can be observed due to the sensitivity of the experimental method. Although only a small portion of the Thomas-Reiche-Kuhn sum rule is exhausted, the high flux of virtual photons at low energies increases dramatically the observed Coulex cross section.

Since the detector response shifts systematically the strength towards lower energies, the GDR and PDR distributions are strongly entangled in the 1n channel. This effect also distorts the distribution in the 2n channel, hindering the extraction of all three GDR distribution parameters (peak energy, width and strength) from the measured data. Various systematical models have therefore been used to define the peak energy and width of the GDR, while the strength has been extracted from the data by χ^2 minimization. The position of the GDR is close to the 2n threshold for these nickel isotopes: depending on the branching ratios for the one- and two-neutron-decay channels, more or less cross section in the one-neutron channel can be attributed to the GDR. This strength cannot be distinguished from the PDR strength, since it is automatically shifted to much lower energies due to the detector response.

	Experimental data		Junghans *et al.*			Systematics		
^{A}Z	σ_{1n} [mb]	σ_{2n} [mb]	σ_{1n} [mb]	σ_{2n} [mb]	S_{TRK} [%]	σ_{1n} [mb]	σ_{2n} [mb]	S_{TRK} [%]
^{67}Ni	467(31)	224(21)	296.8	238.3	92(9)	358.1	238.6	98(9)
^{68}Ni	386(16)	263(14)	178.0	298.1	91(5)	210.2	293.7	93(5)
^{69}Ni	287(39)	267(25)	147.2	256.5	78(8)	208.6	292.0	79(8)

Table 6.7: Comparison of the measured total cross sections with the calculated GDR Coulex cross sections for $^{67-69}$Ni. Only the statistical error on the data is given. The cross section values of the two systematical models correspond to the cross sections in the individual neutron-decay channels for the TRK strength obtained by fit to the experimental data.

Table 6.7 provides an overview of the integrated Coulex cross sections. The experimental data is taken from table 6.3, while the calculated values are given by the strength distributions shown in figure 6.9. The minimization routine not only provides the total strength distribution, but also the contributions of the individual neutron-decay channels. The excess of measured Coulex cross section in the one-neutron channel can be clearly seen from the comparison to both GDR models. The observed GDR cross sections are smaller than the value predicted by the TRK sum rule. Even if the GDR strength of the fit function is set to the full sum-rule value, the entire cross section of the one-neutron-decay channel cannot be described completely. The excess Coulex cross section values given in table 6.5 show that the remaining cross section is significant. However, the fraction of sum-rule strength carried by the PDR can only be determined with the excitation-energy distribution.

Up to now, only the isovector giant and pygmy dipole resonances have been taken into account. Due to the large E2 component of the virtual photon field (fig. 2.11), the

quadrupole modes should be considered as well. Although the electromagnetic excitation process excites preferably isovector modes, the ISGQR and the IVGQR are coupled [17]. The IVGQR is located at higher energies than its isoscalar counterpart, since the symmetry energy must be overcome in the former mode, and will therefore be neglected. The first case considered uses the ISGQR parameters from the systematical trend [1]:

$$\begin{aligned} E_m &= 64\, A^{-1/3}\ \text{MeV} \\ \Gamma &= 16\, A^{-1/3}\ \text{MeV} \end{aligned} \tag{6.1}$$

which yields $E_m = 15.7$ MeV and $\Gamma = 3.9$ MeV for ^{68}Ni. Monrozeau *et al.* have measured the GMR and GQR in ^{56}Ni by (d, d') [92] and report a cross section corresponding to 76(13)% sum-rule strength for the ISGQR. Other ISGQR measurements on ^{58}Ni present 82(10)% [93] and 73(3)% [94] sum-rule strength. Considering these results, a sum-rule strength of 80% for the ISGQR of ^{68}Ni will be considered. With this strength value and by using expression (6.1) for the peak energy and width of the ISGQR, an integral cross section of 24.1 mb is obtained for the 1n decay channel and 20.4 mb for the 2n channel, yielding a total of 44.5 mb. The GQR cross section covers at most 10% of the GDR cross section, while the energy range is similar. By comparing the GQR cross sections with the excess cross section in table 6.5, it can be excluded that the entire additional cross section must be attributed to the quadrupole mode. Also, since the IVGDR and ISGQR modes overlap in energy, a portion of the GQR has already been effectively subtracted in the subtraction of the GDR, since the quadrupole resonance has been neglected at that stage.

While the quantification of the Coulex cross section of the low-lying strength is straightforward, the extraction of peak energy, width and photoabsorption strength is not. The χ^2 maps for ^{68}Ni (fig. 6.16) and for ^{69}Ni (fig. 6.17) clearly show that minima exist, with, however, relatively large distribution-width values, such that the PDR parameters cannot be defined precisely enough. It should be reminded here that the low-lying strength is not necessarily of resonant character, which most likely cannot be described by a smooth function such as a Gaussian distribution. Data for ^{68}Ni has been measured by the RISING collaboration at GSI [8], which shows the PDR at 11 MeV with a width of less than 1 MeV. The parameter map for the data of the present experiment shows the χ^2 minimum at 13.0(3) MeV and a width of 1.3(3) MeV. In order to compare the two results, a PDR delta distribution peaking at 11 MeV has been compared to the measured data, which is shown in figure 6.18. The fit yields a PDR strength of 4.9(6)% TRK sum-rule strength, with $\chi^2_\nu = 2.17$. The data near the one-neutron threshold is well described by the delta function at 11 MeV, while the higher energies are not. The region above 15 MeV could host a non-statistical component of the neutron decay, which can be seen around 8-9 MeV in the kinetic energy distribution of the 1n decay channel of ^{68}Ni (fig. 6.2). A neutron kinetic energy of 8 MeV corresponds to an excitation energy of

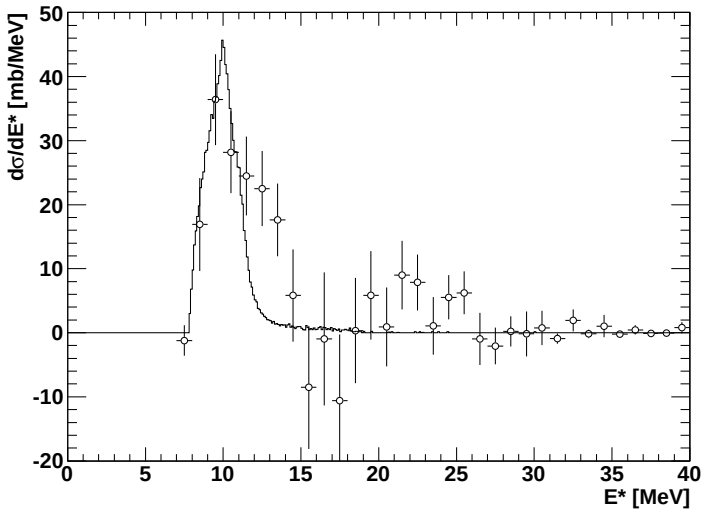

Figure 6.18: PDR distribution fit to excess ^{68}Ni Coulex cross section. The data points are the measured values after subtraction of the GDR distribution.

at least 15.8 MeV, since the neutron threshold of ^{68}Ni is located at $S_n = 7.8$ MeV [77]. Such an energy is clearly above the PDR region, and should therefore be subtracted from the excess cross section when the statistical component of the GDR is removed. Since this requires a correct understanding and modelling of the non-statistical decay, this procedure will be applied at a later stage of the analysis. The interpretation of the PDR of ^{68}Ni reported by Wieland *et al.* relies on a calculation of the branching ratio of the gamma decay. Considering figure 6.18, the PDR could present a structure with a small gamma-branching ratio, which could therefore not be measured in the RISING experiment.

The current status of the data analysis does not allow definite assertions on the shape and strength of the pygmy dipole resonance in neutron-rich nickel isotopes. However, it does allow the conclusion that low-lying dipole strength has been observed in the present experiment, and that the PDR strength of ^{68}Ni is of the order of 5 to 10% of the TRK sum-rule strength. A considerable effort is still required to improve the understanding of the excitation functions of ^{67}Ni and ^{69}Ni, which suffer from the small amount of useable data available, as well as from the severe detector deficiencies.

Chapter 7

Conclusions and Outlook

The analysis of the experiment presented in this work has revealed the presence of low-lying dipole strength in neutron-rich nickel isotopes. Since the reaction cross sections are of major interest, the first intermediate goal of the present experiment was to test the reproducibility of previously measured data. The measured cross sections of ^{58}Ni are consistent with the Fultz *et al.* measurement, which allows us to gain confidence in the analysis results. However, due to the fact that the proton threshold is lower than the neutron threshold, and that the (γ,np) channel opens near the peak energy of the GDR, the excitation-energy distribution is severely distorted, and only one third of the expected dipole strength is observed in the visible channels, mainly due to the low S_p threshold. The excitation function for the one-neutron-decay channel can be reconstructed, but cannot be compared with the old measurement. To prevent this complication, a measurement with nickel mass $A = 62$ and upwards would have been necessary. The natural abundance is small, resulting in the lack of previously measured data, for which an isotopically pure target of the cited nuclide is required.

Due to the complex response of several detectors, the GDR and PDR distributions could not be distinguished quantitatively in a model-independent manner. Considering only the two-neutron-decay channel, it was shown that the GDR distributions can be reasonably well described by systematical relationships for the peak energies and widths of the giant dipole resonances, obtained exclusively with stable nuclei. These two GDR variables were fixed while the strength was determined by χ^2 minimization with respect to the experimental data and expressed as a fraction of Thomas-Reiche-Kuhn sum-rule strength. The low-lying dipole strength was then obtained by subtracting the complete GDR from the measured strength distribution. The remaining excitation energy distribution is extremely wide for a PDR, which yields unrealistic resonance parameters when a free fit is performed. The systematic parameter mapping of the PDR region generates a better view of the possible fit minima. While the distribution parameters are generally not well defined in the χ^2 parameter maps, the strength appears to be

constrained to approximately 10% TRK sum rule strength for ^{68}Ni and ^{69}Ni. A very narrow distribution at 11 MeV, as observed in the RISING results for ^{68}Ni, provides a reasonable agreement with the data, although the high-energy portion of the PDR strength distribution cannot be described.

The second main topic presented in this thesis is the test experiment of Resistive Plate Chambers for use in NeuLAND carried out at KVI in Groningen. Based on the calculated proton spectrum resulting from the hadronic interaction of a relativistic neutron with a slab of Fe, the time resolution of two RPC prototypes was measured with various low-energy proton beams. The test experiment shows that the time resolution remains within the required limit of a sigma value of 100 ps even for the lowest proton energies. These results allowed the conclusion that the RPC concept for NeuLAND should be viable, leading to the development of detector prototypes tailored to match the requirements of NeuLAND, concerning the time and position resolution, as well as the necessity to include passive iron converter material into its structure in order to enhance the homogeneity of the final detector.

* * *

The analysis of the nickel experiment is still in progress. The next required steps will include the better understanding of the shape of the excess dipole strength, in particular the reason for the spreading to higher energies. The direct back-decay of the E1 resonance to the ground state could be included in the analysis, leading to high-energy components in the kinetic-energy distributions of the neutrons. The E2 resonance modes should also be taken into account, such that they can also be subtracted. An important issue is the dramatically low strength value of ^{69}Ni, which does not match the results of the neighboring isotopes. Detector effects cannot be fully excluded yet and require a more thorough investigation. Once these issues have been solved, the $^{70-72}$Ni still must be analyzed, although the total amount of statistics has not been confirmed to be sufficient yet.

Appendix A

GDR and PDR Parameter Mapping for $^{67-69}$Ni

Figures A.1, A.2 and A.3 present the parameter mapping of the strength, peak energy and width on the GDR region of ^{67}Ni, ^{68}Ni and ^{69}Ni, respectively. The χ^2_ν scale (color scale) is identical to all strength plots in a given figure, such that these plots can be compared with each other. Since only the GDR is investigated, the fit range has been chosen to exclude any influence of low-lying strength. In order to prevent the definition of an arbitrary limit, the 2n threshold of the various isotopes has been chosen as lower limit for the fit procedure.

Figures A.4, A.5 and A.6 present the parameter mapping of the strength, peak energy and width on the PDR region of ^{67}Ni, ^{68}Ni and ^{69}Ni, respectively. The GDR peak energy and width have been fixed to the values of Junghans *et al.* and the GDR strength has been set to the optimum value of the GDR fit. All three GDR parameters are listed in table 6.4 for the three nickel isotopes. The χ^2_ν value is calculated over the entire excitation energy range.

These data sets are discussed in subsections 6.2.3 and 6.2.4.

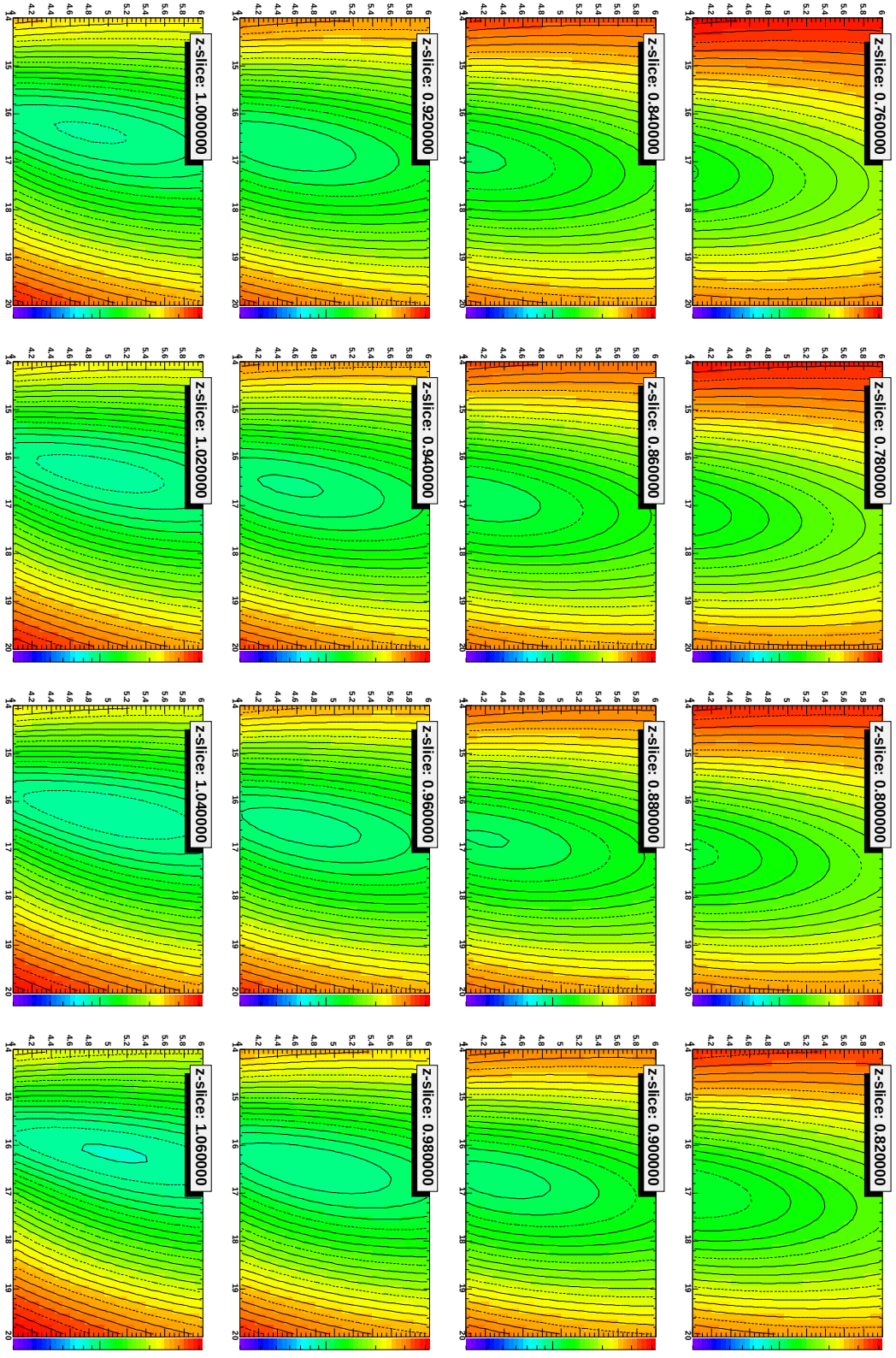

Figure A.1: Complete GDR parameter mapping for ^{67}Ni. The various contour plots represent different GDR strengths as a fraction of the TRK sum-rule strength. The GDR peak energy and width are represented on the horizontal and vertical axes, respectively. The $\chi^2_\nu = 1$ value is drawn in light green.

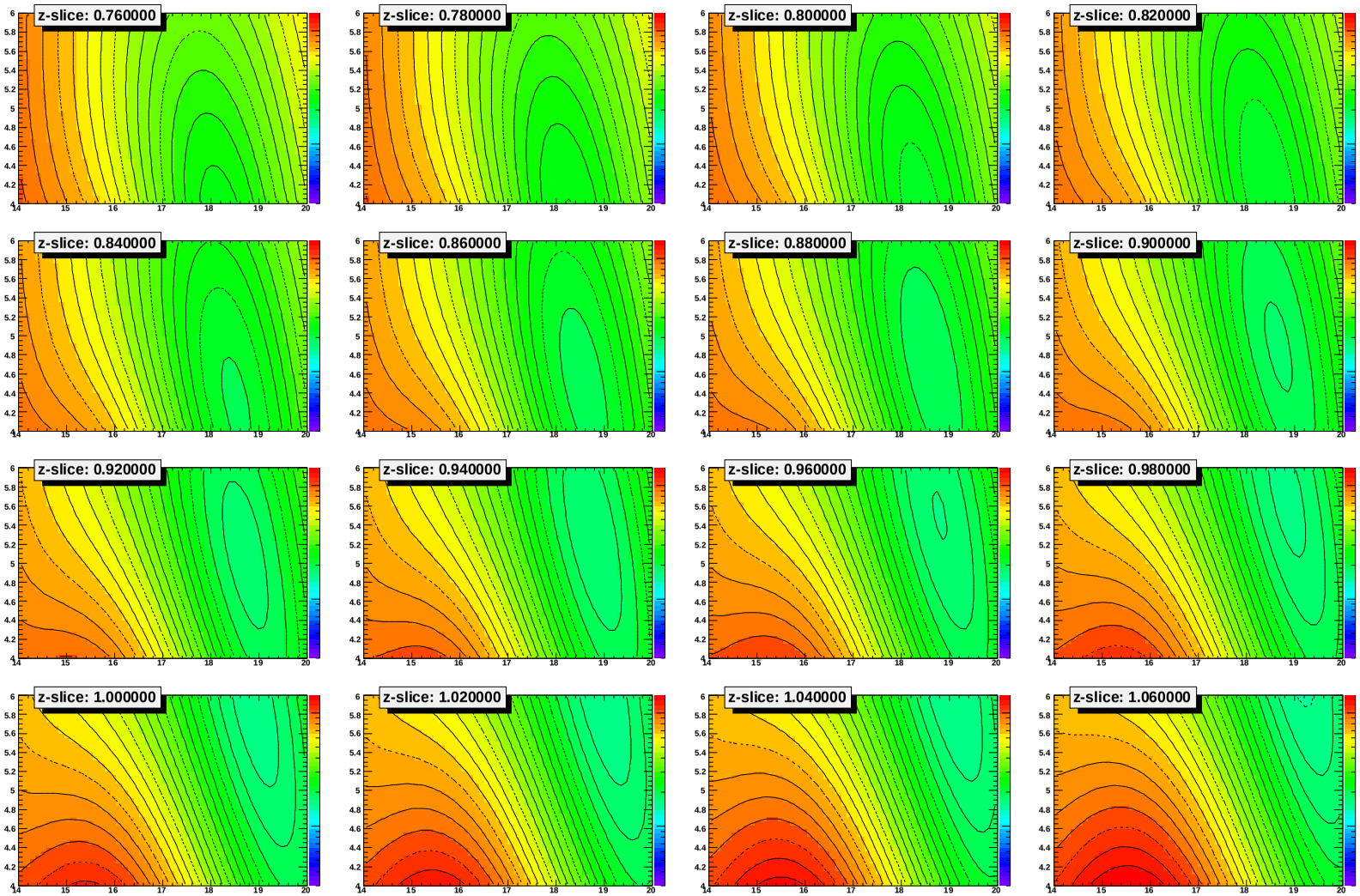

Figure A.2: Complete GDR parameter mapping for ^{68}Ni. The various contour plots represent different GDR strengths as a fraction of the TRK sum-rule strength. The GDR peak energy and width are represented on the horizontal and vertical axes, respectively. The $\chi^2_\nu = 1$ value is drawn in turquoise.

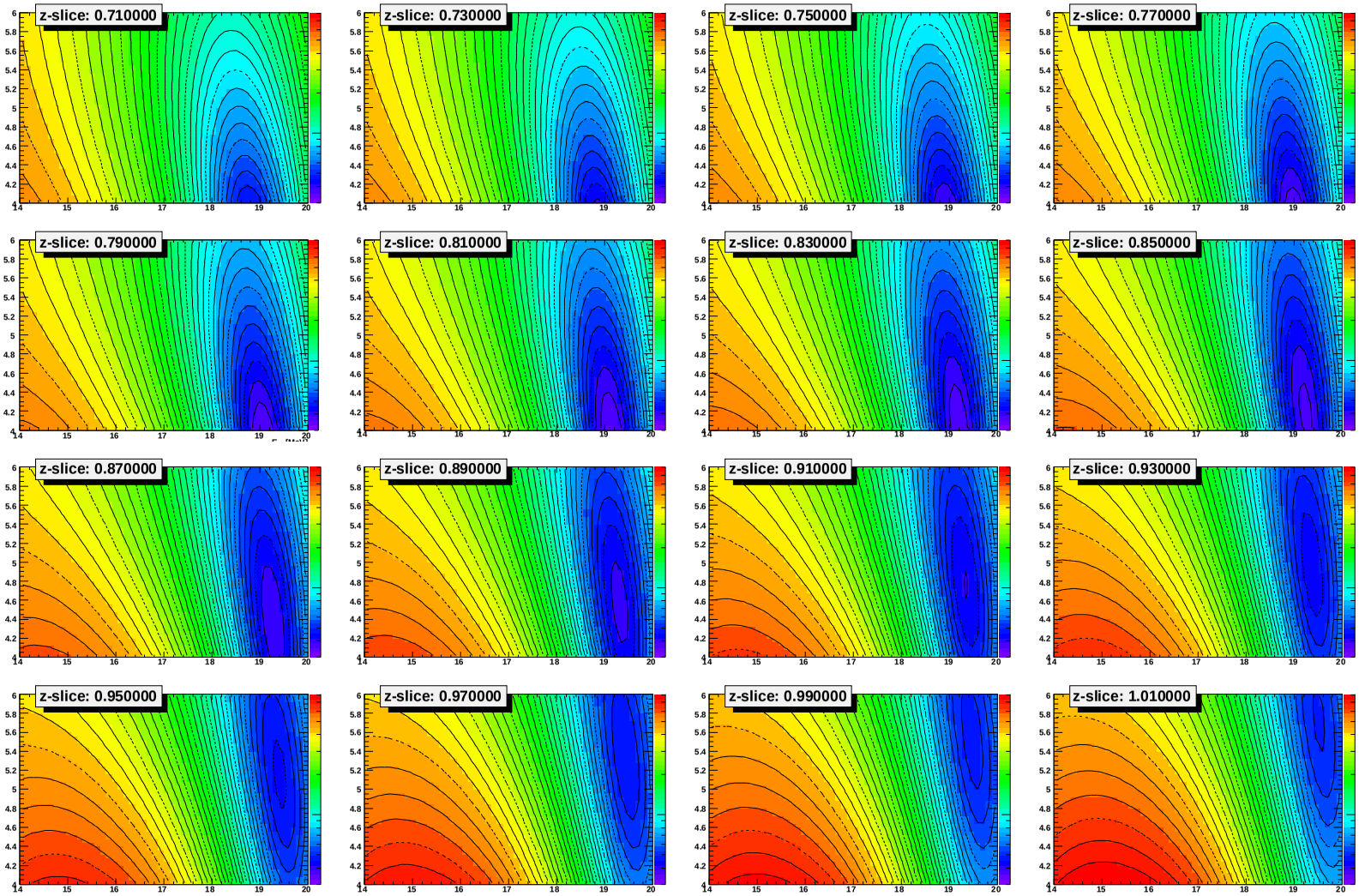

Figure A.3: Complete GDR parameter mapping for ^{69}Ni. The various contour plots represent different GDR strengths as a fraction of the TRK sum-rule strength. The GDR peak energy and width are represented on the horizontal and vertical axes, respectively. The $\chi^2_\nu = 1$ value is drawn in turquoise.

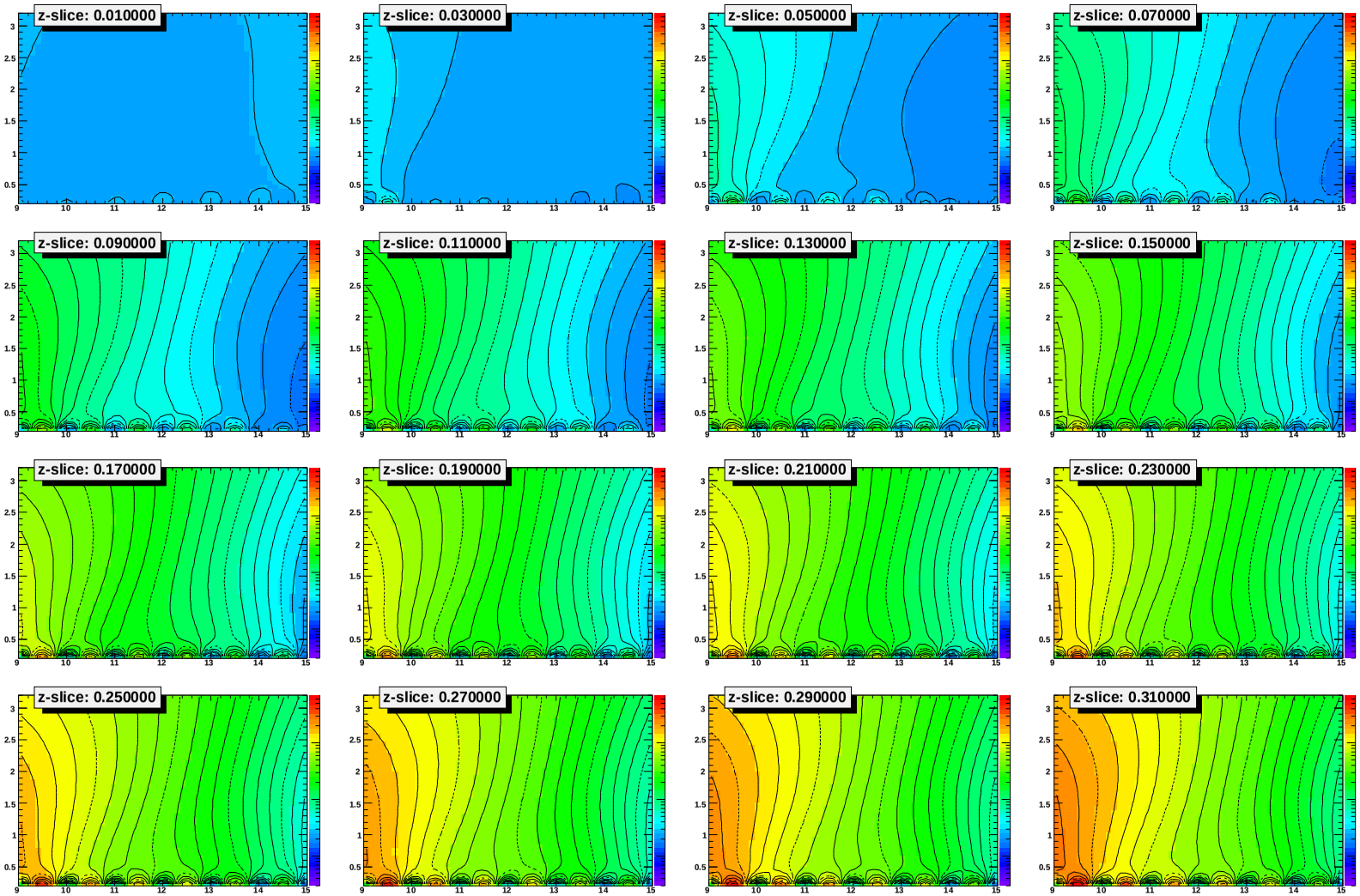

Figure A.4: Complete PDR parameter mapping for ^{67}Ni. The various contour plots represent different PDR strengths as a fraction of the TRK sum-rule strength. The PDR peak energy and width are represented on the horizontal and vertical axes, respectively. The $\chi^2_\nu = 1$ value is drawn in blue.

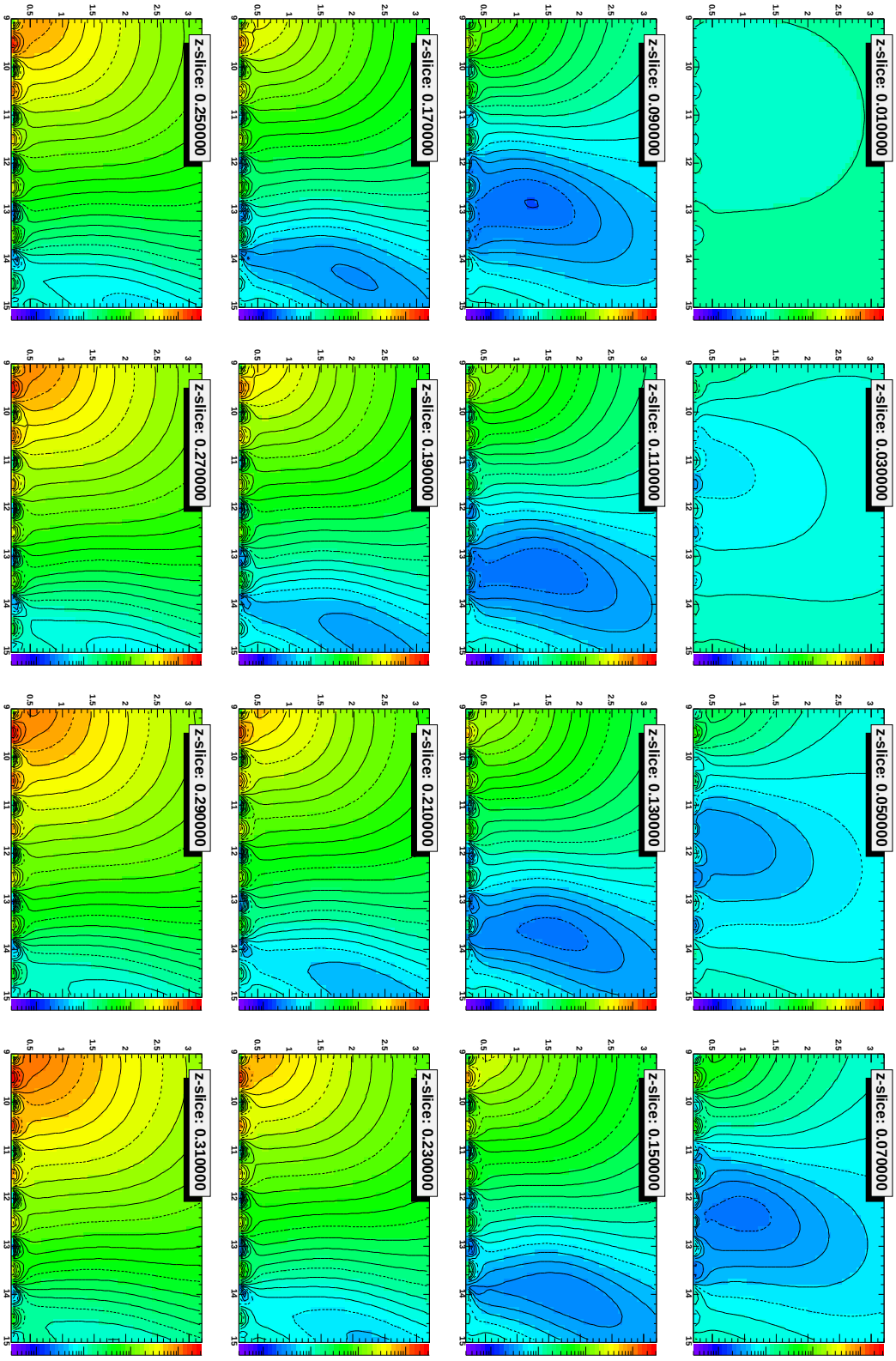

Figure A.5: Same as figure A.4, but for ^{68}Ni.

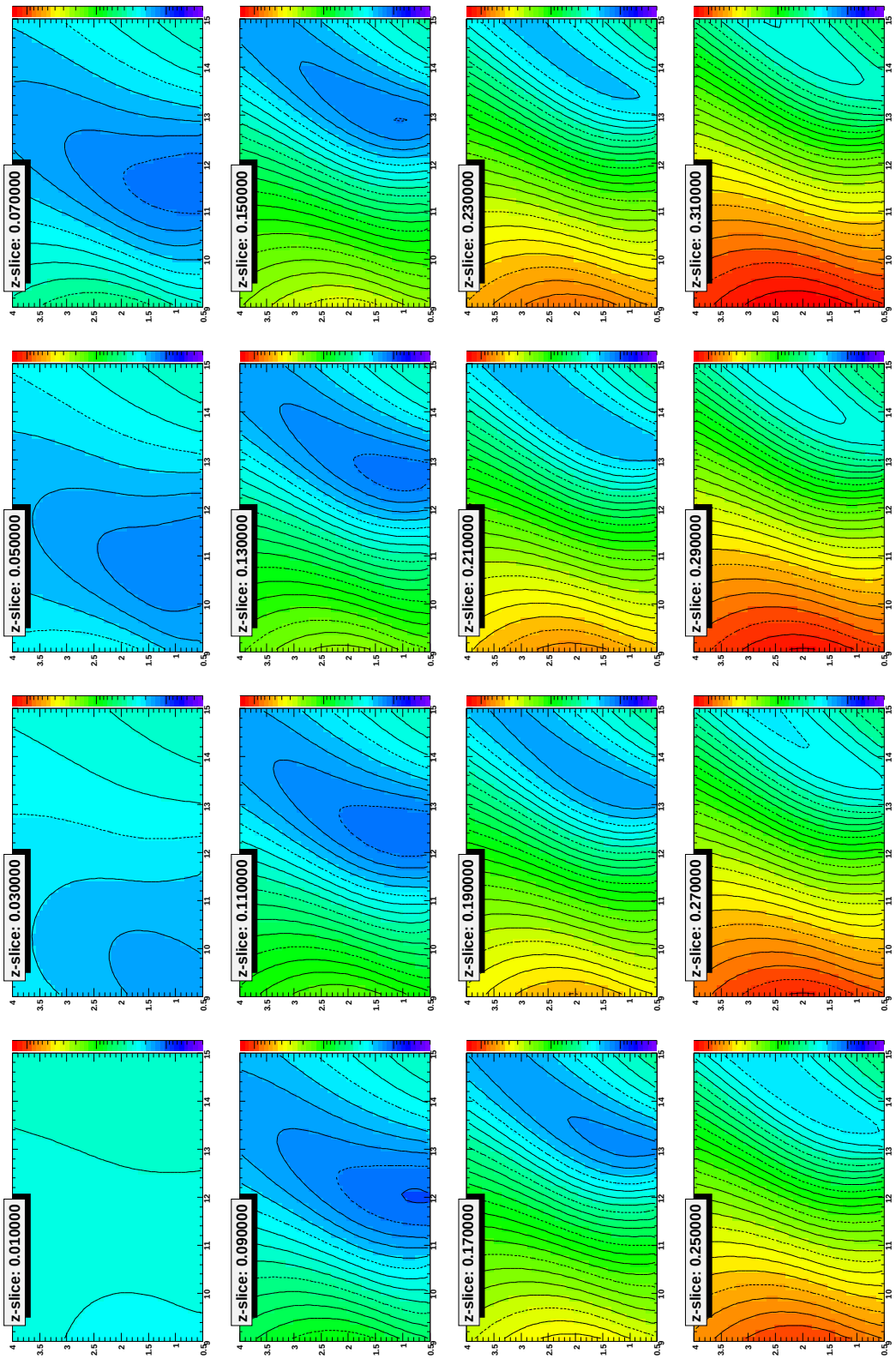

Figure A.6: Same as figure A.4, but for ^{69}Ni.

Appendix B

KVI RPC Test Results

The NeuLAND detector for R^3B will replace the existing LAND detector and will be based on Resistive Plate Chambers (RPC). RPC detectors are used in various high-energy-physics experiments, and are commonly used to detect minimum-ionizing particles. As described in section 3.4, the high-energy neutrons generate various secondary particles, which are in most cases not minimum-ionizing. The response of RPC detectors was therefore investigated in a test experiment, in which two RPC detectors were exposed to protons with energies ranging from 190 MeV down to 26 MeV. The RPC must present a time resolution of less than 100 ps in order to meet the requirements of R^3B. The results of this test experiment are presented in subsection 3.4.4. The following sections will describe how these results are obtained.

B.1 Data Selection

The selection of good events is based on the energy signal of the second scintillator detector (S2). Figure B.1 presents the QDC spectrum of 120 MeV protons in this detector, as well as the boundaries of the energy cut (dashed red lines). The energy values are given by the geometrical mean of the QDC values for the two PM tubes. Due to the fact that the data acquisition is triggered by the coincidence of overlapping time signals of the PM tubes of the first scintillator (S1), the above condition constrains the angle of the trajectory, rejecting protons scattered at large angles. Since the FOPI RPC anode pitch is smaller than the diameter of the collimator, the strip with the largest number of direct hits should be determined. If a strip off the beam axis is chosen, mainly scattered protons will be observed, for which the angle and energy are not defined. The 120 MeV proton-beam profile on the FOPI RPC is shown in figure B.2. The fifth strip of the RPC was clearly the closest to the beam axis, and will therefore be used to determine the time resolution.

The condition on the S2 energy must be removed for the proton beams at the lowest

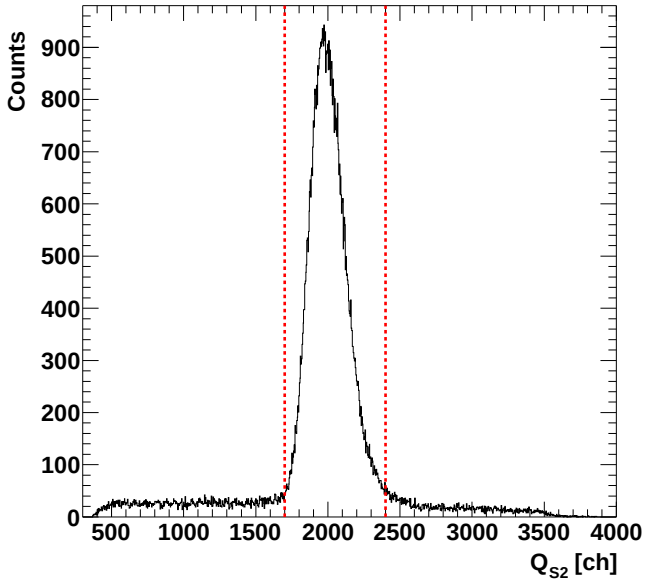

Figure B.1: QDC spectrum of 120 MeV protons in scintillator 2. The dashed red lines indicate the energy-cut boundaries.

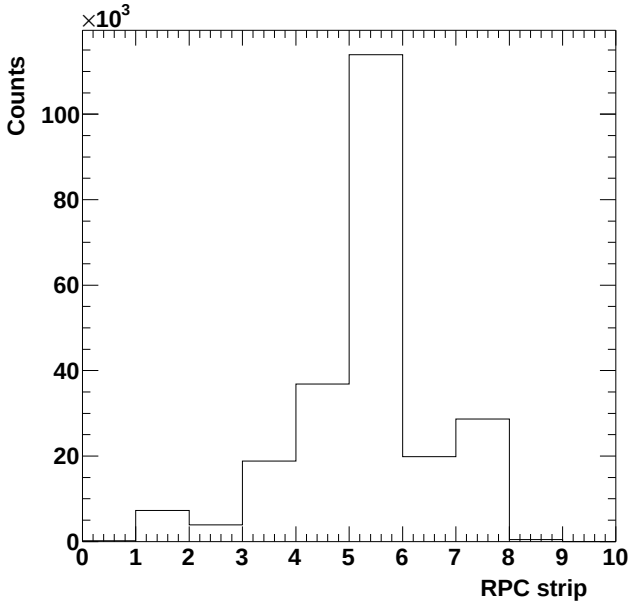

Figure B.2: 120 MeV proton beam profile on the FOPI RPC.

energies, since they do not pass through the entire RPC detector, which widens the time distribution. Also, the protons are stopped at various locations inside the RPC, which can influence the timing information. For NeuLAND, this could be a serious problem, since the proton yield for high-energy neutrons on passive Fe converter peaks at these low energies. This calls for a high layer granularity, such that the low-energy protons pass at least one entire RPC submodule before being stopped in the following converter layer.

B.2 Trigger-detector Time Resolution

The measurement of the RPC time resolution requires the quadratic subtraction of the intrinsic trigger-detector resolution, as described by equation (3.4). The mean time distribution of the S1 detector is shown in figure B.3 for 120 and 38 MeV protons with $\sigma_{S1} = 0.93$ and $\sigma_{S1} = 1.04$ channels, respectively. The values for the other energies are listed in table 3.1 in chapter 3.

B.3 RPC Time Resolution

The extraction of the RPC time resolution is achieved by fitting a Gaussian to the time-of-flight distribution between the S1 trigger detector and the RPC. With the FOPI RPC, an additional complication is introduced by the multiple anode strips. The cross-talk level is quite high, meaning that a given RPC strip will also register hits on neighboring strips. The charge of a given electron avalanche will, however, only be observed in the strip actually hit. A two-dimensional plot with the time-of-flight and measured charge allows the separation of real hits and cross-talk. If all strips have the same amplification, the strip with highest charge in a given event can also be used. Figures B.4 and B.5 present in their respective left panels such plots, showing predominantly one charge distribution corresponding to the strip hits. This type of plot also shows a dependence of the time-of-flight on the QDC energy value - the so-called walk effect - which can then be corrected. A small linear walk correction has already been applied to the distributions in figures B.4 and B.5. The time resolution can now be obtained by projecting the corrected 2D plots onto the time axis, which is shown in the right panels of figures B.4 and B.5. A Gaussian distribution helps the extraction of the time resolution: the values for the various energies are listed in table 3.1.

The procedure is very similar for the LIP RPC, with the only difference that no cross-talk is observed in the present setup. The result with 48 MeV protons is shown in figure B.6. The LIP RPC time-resolution values are also listed in table 3.1. The values for the LIP RPC should be treated carefully, since the detector read-out was performed using non-matching FOPI pre-amplifiers.

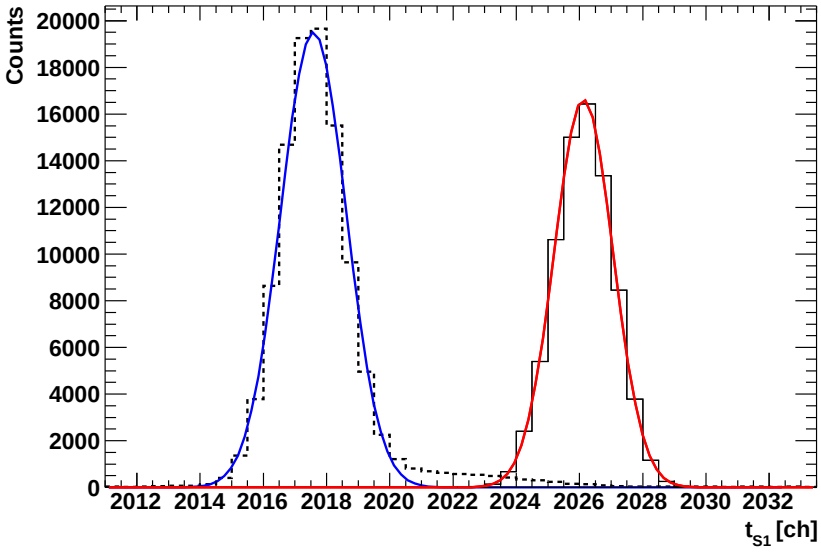

Figure B.3: Trigger scintillator S1 time resolution. Full line with red Gaussian: 120 MeV protons. Dashed line with blue Gaussian: 38 MeV protons.

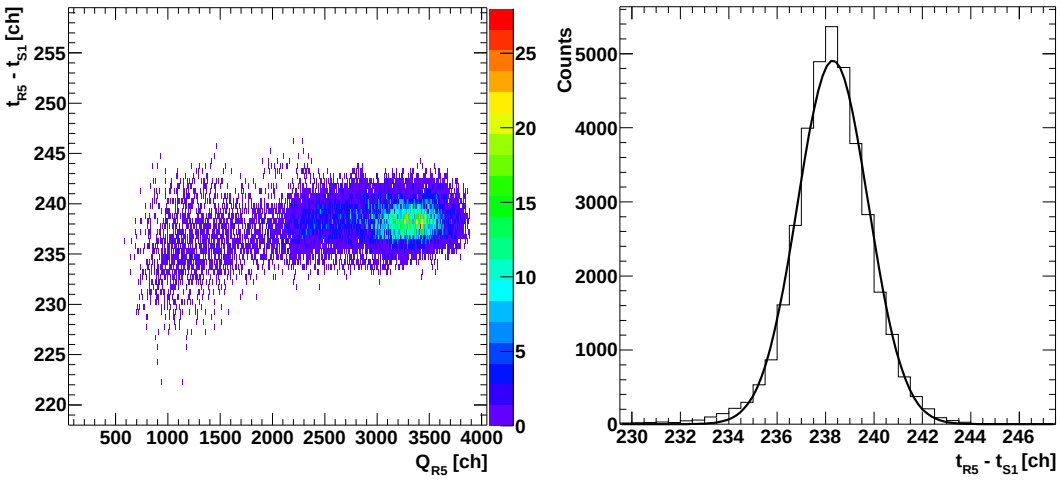

Figure B.4: Time resolution of FOPI RPC strip 5 with 120 MeV protons. Left part: TOF vs. charge distribution. Right part: TOF distribution with Gaussian fit.

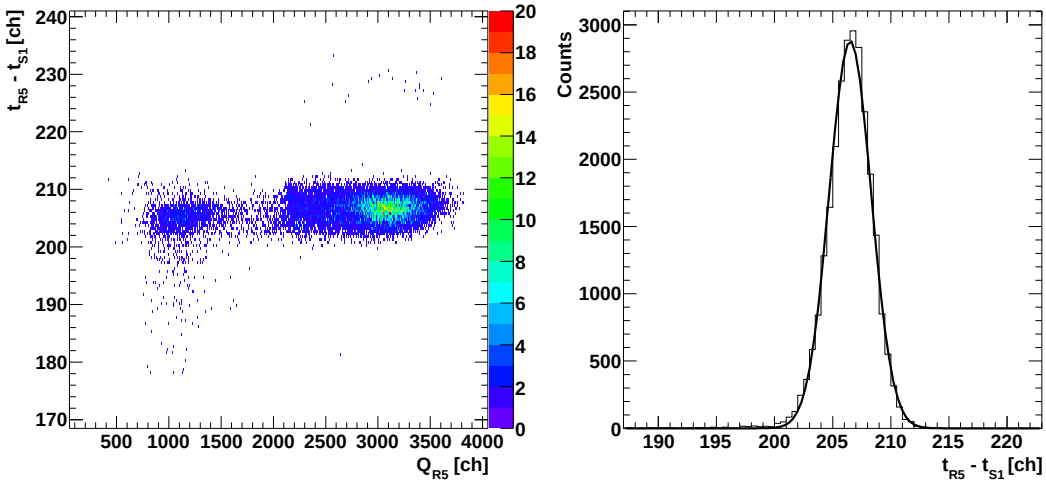

Figure B.5: Same as figure B.4, but for 38 MeV protons.

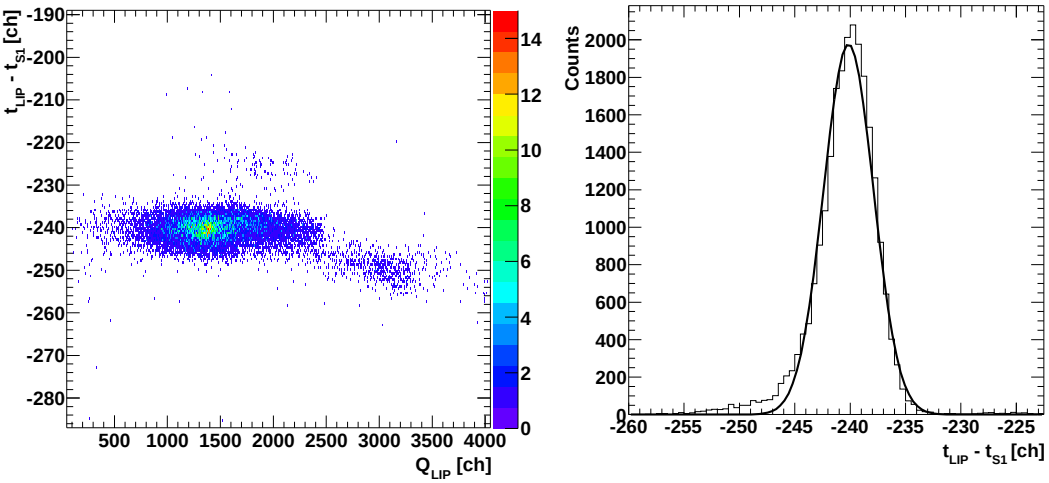

Figure B.6: Time resolution of LIP RPC with 48 MeV protons. Left part: TOF vs. charge distribution. Right part: TOF distribution with Gaussian fit.

Appendix C

RPC Gas Recycling

C.1 RPC Gas Mixture

Current RPC detectors mostly use a common gas mixture, composed of 85% Reclin-134a (1,1,1,2-tetrafluoroethane), 10% SF_6, and 5% isobutane, which allows the operation of the detector under optimal conditions. Each gas has a series of advantages and disadvantages, which are listed below.

C.1.1 Reclin-134a

Reclin-134a is a medium-density gas which has been chosen as the main ionization medium for RPCs. In order to be eligible as counter gas, the atoms or molecules must present a low electron-attachment coefficient [58], since the electron multiplication depends more strongly on the electrons than on the much slower ions. The ideal gas would have a low ionization energy and a high fragmentation threshold. In the case of Reclin-134a, the threshold of ionization through electron loss is located at 12.64 eV [95]. Even though the first dissociation channel $CH_2F^+ + CF_3 + e^-$ opens at 12.99 eV, its relative yield is significant only above 17.5 eV. For comparison, Ar counter gas requires 26.2 eV to form an electron-ion pair [58].

Using Reclin-134a as counter gas has several advantages: it is non-toxic, practically inert and relatively inexpensive since it is commonly used in refrigeration systems. In contrast to chlorofluorocarbon (CFC) compounds, which are major actors in the depletion of the ozone layer, hydrofluorocarbon (HFC) species, such as Reclin-134a, are harmless in this respect. However, Reclin-134a has a significant Global Warming Potential (GWP) of 3300 for a time horizon of 20 years, 1300 for 100 years and 400 for 500 years [96]. The GWP of a gas x is usually given relative to CO_2 and is defined as:

$$\mathrm{GWP}\,(x, TH) = \frac{\int_0^{TH} a_x p_x\,(t)\,dt}{\int_0^{TH} a_r p_r\,(t)\,dt} \tag{C.1}$$

where TH is the considered time horizon, a is the radiative efficiency of the gas species (in W/(m$^2\cdot$ kg)), $p(t)$ is the abundance as a function of time, and r labels all quantities related to the reference gas. Reclin-134a has a strong radiative efficiency of 150 W/(m$^2\cdot$ppmv) and a lifetime of 13.8 years.

C.1.2 SF_6

Sulfur hexafluoride is an inert non-toxic gas used in great quantities in the electrical industry due to its large dielectric strength. As a component of the RPC detector gas, its main responsibility is to capture thermal electrons, which could lead to a spurious avalanche. As seen in figure C.1, the electron-attachment cross section peaks at lowest energies. However, higher electron energies cause fragmentation of the molecule, producing various charged and neutral species, as shown by figure C.2 [97]. The presence of SF_6 in the RPC gas gap therefore will lead to a contamination through fragments and, mainly, F^- ions.

SF_6 has one of the highest GWP values due to its high radiative efficiency (520 W/(m$^2\cdot$ppmv)) and long lifetime (3200 years) [96]. This gives a GWP of 15100 for a time horizon of 20 years, 22200 for 100 years and 32400 for 500 years.

C.1.3 Isobutane

The purpose of adding a small amount of isobutane is to absorb UV photons emitted by the counter gas. Collisions of electrons with gas molecules, which do not lead to an electron-ion pair but to an excitation of the molecule, will emit one or several photons [58]. UV photons can ionize other molecules with a lower ionization potential, or expel electrons from a metal surface *via* the photoelectric effect. The electrons created with this mechanism will lead to an avalanche in the RPC and will be detected as any other normal hit. This can cause dead-time effects, or rate-dependent efficiency losses. Polyatomic molecules such as isobutane are efficient UV quenchers, since they possess a high number of vibrational and rotational degrees of freedom. The only disadvantage of isobutane is its flammability, but since it is placed in a non-oxidizing environment, it will not pose a threat if not exposed to air.

C.2 RPC Gas Recirculation System

The previous section has showed that Reclin-134a and SF_6 are very potent greenhouse gases. A once-through gas circuit for NeuLAND is not an option, since legal requirements will at one point prohibit the deliberate release of greenhouse gases into the atmosphere. A closed-circuit RPC gas system therefore seems the most reasonable solution, which will also present a financial benefit through the limited need for fresh gas. The system also

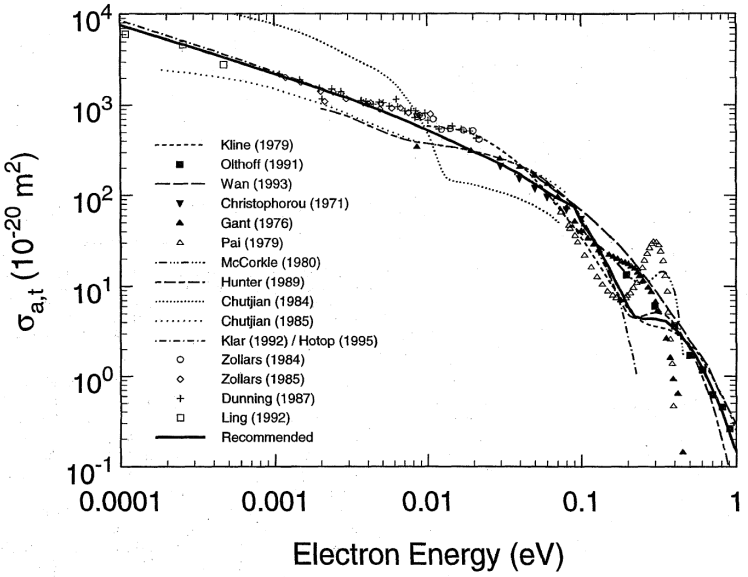

Figure C.1: Electron-attachment cross section on SF_6 as a function of electron energy. From Christophorou and Olthoff [97].

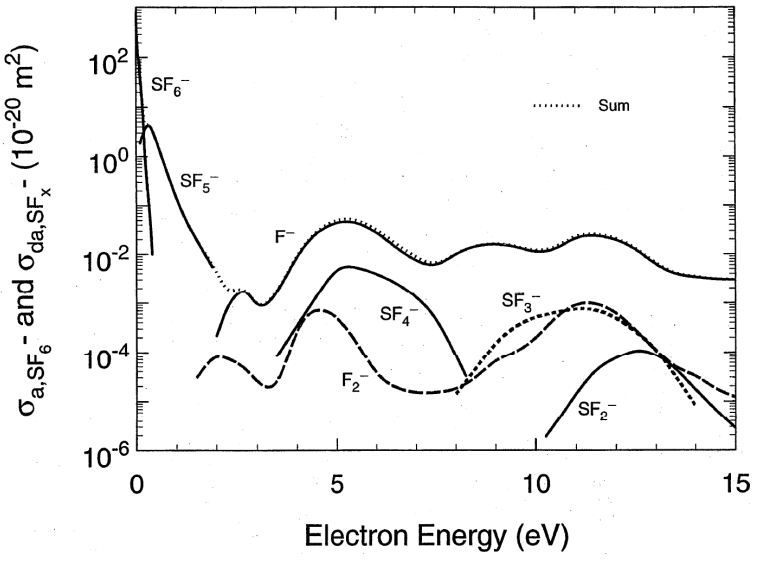

Figure C.2: Electron-impact-dissociation cross sections of SF_6 as a function of electron energy. From Christophorou and Olthoff [97].

provides an intrinsic quality control of the gas composition, allowing the early detection of eventual impurities. The proposed recirculation system is presented in figure C.3, and consists of a main circuit, a condenser circuit, an injection circuit and an on-line gas-analysis system. These subsystems will be described in the following subsections. The NeuLAND detector will be located in the R^3B cave. The recirculation system will be connected to the detector *via* long pipes, which will allow the circuit to be located in a zone freely accessible even during beam time.

C.2.1 Main Circuit

The main recirculation circuit (path ABCDEF in fig. C.3) is responsible of exchanging and cleaning the NeuLAND gas volume under normal working conditions. The first element of the loop is the circulation pump (*e.g.*, peristaltic pump) capable of generating a gas flux of up to 5 l/min. With this flux, the entire 4 m^3 of NeuLAND would be exchanged twice per day. Knowing that only a portion of this volume will be accessed by the gas, this flux allows a large enough tolerance on the gas exchange frequency until the final detector design is chosen.

The central piece of the recycling system is the gas scrubber located between points C and D. The RPC gas is dominated by fluorinated compounds, which will eventually produce hydrofluoric acid (HF), light and heavy fragments by electron impact. The gas filter will be responsible of removing these species from the gas volume. Soda lime, which is a mixture of approximately 75% $Ca(OH)_2$, 20% H_2O, 3% NaOH and 1% KOH, will be responsible of capturing acidic species, such as HF. Thereafter, a column of activated charcoal will remove all non-volatile compounds as well as highly reactive fragments (*e.g.*, $F^\bullet$ radicals). The gas is then reintroduced into the detector.

The entire circuit, as well as the NeuLAND detector, should be operated at a gas pressure slightly above atmospheric pressure (1 to 1.5 bar), such that air and other impurities cannot enter the system through leaks, at the expense of loosing a small amount of counter gas.

C.2.2 Condenser Circuit

When large amounts of impurities are present in the gas volume, *e.g.*, air during the filling stage of NeuLAND, the condenser circuit will be necessary. The gas flow will be redirected after the main pump (path ABG) into one of the two condensing units. Figure C.4 depicts schematically the solid and liquid phase regions of the three RPC gases. Two possible temperature ranges are possible for the freeze-out of the gas. Either the temperature is lower than 140 K, which will convert all three gases to the solid phase, or the temperature is kept between 140 K and 209 K, in which case only SF_6 will be solid. Liquid nitrogen can be used in the former case, while a cryostat is required for

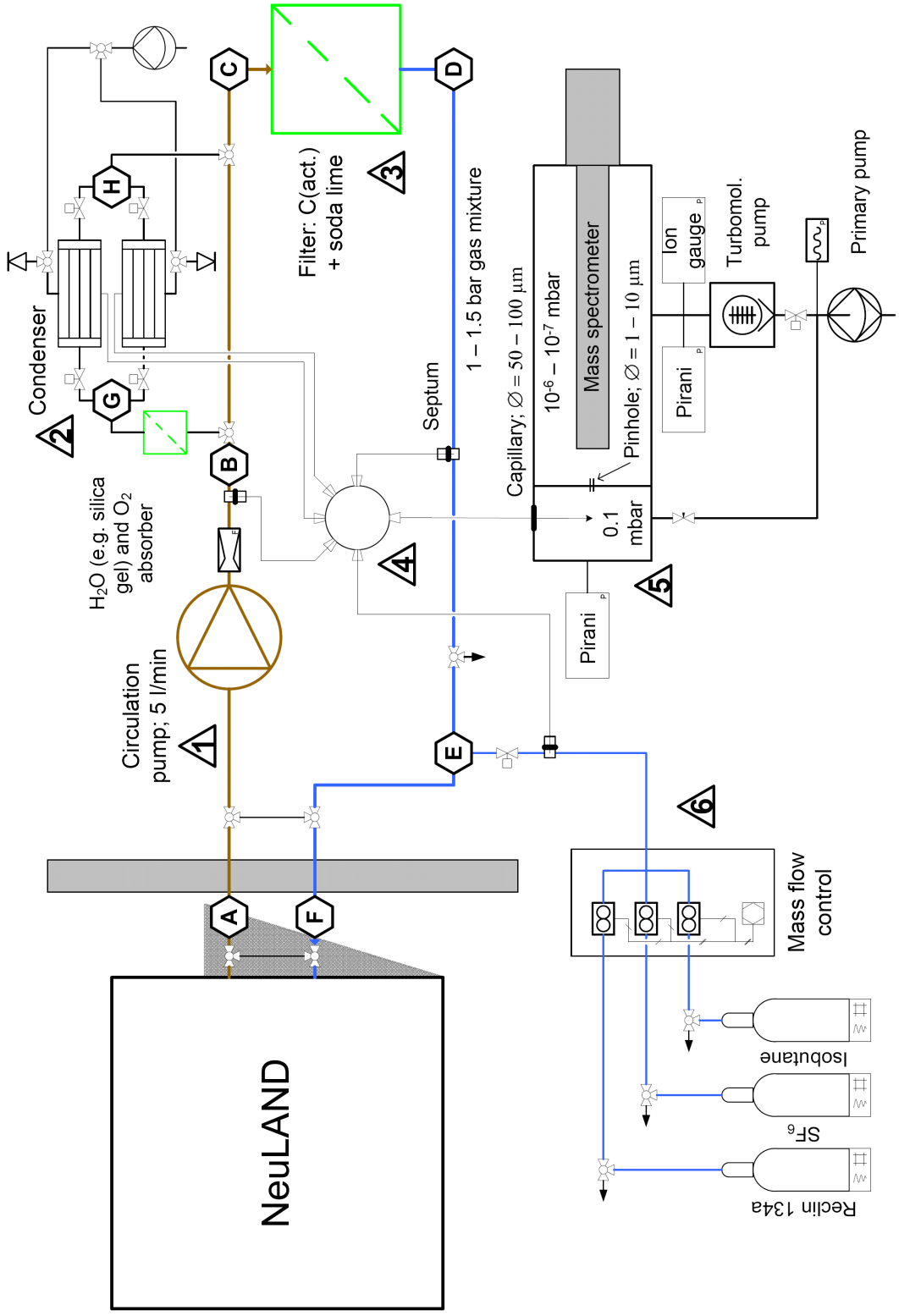

Figure C.3: Proposed RPC gas recirculation system.

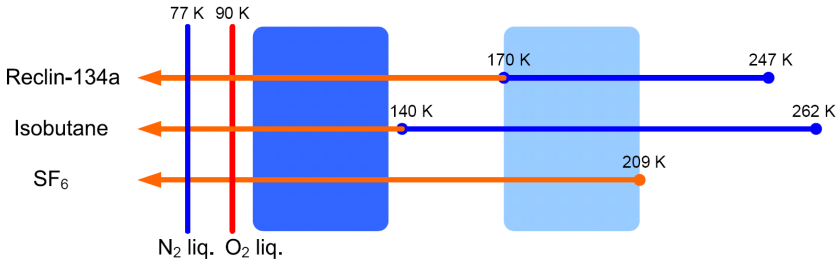

Figure C.4: Schematic phase diagram for RPC gas species at atmospheric pressure. The blue lines represent the liquid phase and orange lines the solid phase. The potential operation temperature domains are highlighted by the blue shaded regions. The boiling points of N_2 and O_2 are also indicated.

the latter.

The gas condenser can be cooled with liquid N_2 if no oxygen is present. Otherwise, a small pump must be used to lower the pressure: since the O_2 vapor pressure is sufficiently high even at 77 K, the oxygen will be expelled. While the gas is collected in the condenser, fresh gas can be injected to flush the NeuLAND detector. As soon as the gas freezer is full, the second unit is cooled down while the first one warms up and injects its contents into the main circuit again (*via* HCDEF). Repeating the alternating cooling/thawing cycle, air and other impurities can be removed from the gas mixture without releasing the entire volume. Since this procedure introduces more gas than necessary into the total circuit, the surplus can be stored in one of the freezing units for later use. Overpressure valves must be mounted on the gas condensers in order to avoid an explosion if the cooling fails on a closed gas tank.

C.2.3 Gas Injection Circuit

The RPC gas injection circuit consists of a gas mixing unit composed of mass-flow-meters calibrated for the individual gases. Here the pure gases are mixed and injected *via* path EF. This branch is currently used for supplying the RPC prototypes with counter gas. The gas bottles will be placed on scales, such that the amount of remaining gas can be estimated at all times. Once the gas is being recirculated, the need for fresh gas will be small. Due to inevitable leaks in the system, this branch cannot, however, be simply deactivated.

C.2.4 On-line Gas Analysis System

Knowledge of the exact gas composition is a very important aspect in such a system, and therefore the on-line analysis tool is of major importance. A quadrupole mass

spectrometer is proposed, since this allows the quantification of the three RPC gases, as well as possible contaminants. A multi-port valve (*e.g.*, HPLC valve) will be used to withdraw samples from various locations in the circuit. A network of capillaries will be installed towards carefully selected points, such that the gas quality and composition can be monitored in all operation phases. Using a simple septum, the capillary can be introduced directly into the gas flow.

The gas samples will be led into a sample chamber at 0.1 mbar in front of the mass spectrometer. A pinhole with an aperture of 1 to 10 μm will allow a fraction of the gas sample to pass into the spectrometer chamber at 10^{-6}-10^{-7} mbar for analysis. The information obtained with the mass spectrometer will be collected by a central slow-control system, which will monitor continuously the gas composition. All valves, pumps, mass-flow-meters, pressure gauges, etc. will be controlled by this central system, such that the entire recirculation process can run automatically.

Bibliography

[1] Harakeh, M. N. and van der Woude, A. *Giant Resonances; Fundamental High-Frequency Modes of Nuclear Excitation.* Clarendon Press, Oxford, (2001).

[2] Dietrich, S. S. and Berman, B. L. *Atomic Data and Nuclear Data Tables* **38**(2), 199 – 338 (1988).

[3] Paar, N., Vretenar, D., Khan, E., and Colo, G. *Reports on Progress in Physics* **70**(5), 691–793 (2007).

[4] Leistenschneider, A., Aumann, T., Boretzky, K., Cortina, D., Cub, J., Pramanik, U. D., Dostal, W., Elze, T. W., Emling, H., Geissel, H., Grünschloß, A., Hellström, M., Holzmann, R., Ilievski, S., Iwasa, N., Kaspar, M., Kleinböhl, A., Kratz, J. V., Kulessa, R., Leifels, Y., Lubkiewicz, E., Münzenberg, G., Reiter, P., Rejmund, M., Scheidenberger, C., Schlegel, C., and Simon, H. *Phys. Rev. Lett.* **86**(24), 5442–5445 Jun (2001).

[5] Lane, A. M. *Annals of Physics* **63**(1), 171 – 218 (1971).

[6] Adrich, P., Klimkiewicz, A., Fallot, M., Boretzky, K., Aumann, T., Cortina-Gil, D., Pramanik, U. D., Elze, T. W., Emling, H., Geissel, H., Hellström, M., Jones, K. L., Kratz, J. V., Kulessa, R., Leifels, Y., Nociforo, C., Palit, R., Simon, H., Surówka, G., Sümmerer, K., and Waluś, W. *Phys. Rev. Lett.* **95**(13), 132501 Sep (2005).

[7] Klimkiewicz, A., Paar, N., Adrich, P., Fallot, M., Boretzky, K., Aumann, T., Cortina-Gil, D., Datta Pramanik, U., Elze, T. W., Emling, H., Geissel, H., Hellström, M., Jones, K. L., Kratz, J. V., Kulessa, R., Nociforo, C., Palit, R., Simon, H., Surówka, G., Sümmerer, K., Vretenar, D., and Waluś, W. *Physical Review C (Nuclear Physics)* **76**(5), 051603 (2007).

[8] Wieland, O., Bracco, A., Camera, F., Benzoni, G., Blasi, N., Brambilla, S., Crespi, F. C. L., Leoni, S., Million, B., Nicolini, R., Maj, A., Bednarczyk, P., Grebosz, J., Kmiecik, M., Meczynski, W., Styczen, J., Aumann, T., Banu, A., Beck, T., Becker, F., Caceres, L., Doornenbal, P., Emling, H., Gerl, J., Geissel, H., Gorska, M., Kavatsyuk, O., Kavatsyuk, M., Kojouharov, I., Kurz, N., Lozeva, R., Saito, N.,

Saito, T., Schaffner, H., Wollersheim, H. J., Jolie, J., Reiter, P., Warr, N., deAngelis, G., Gadea, A., Napoli, D., Lenzi, S., Lunardi, S., Balabanski, D., LoBianco, G., Petrache, C., Saltarelli, A., Castoldi, M., Zucchiatti, A., Walker, J., and Buerger, A. *Phys. Rev. Lett.* **102**(9) MAR 6 (2009).

[9] Litvinova, E., Ring, P., Tselyaev, V., and Langanke, K. *Physical Review C (Nuclear Physics)* **79**(5), 054312 (2009).

[10] Vretenar, D., Paar, N., Ring, P., and Lalazissis, G. A. *Nuclear Physics A* **692**(3-4), 496 – 517 (2001).

[11] Paar, N., Niksic, T., Vretenar, D., and Ring, P. *Physics Letters B* **606**(3-4), 288 – 294 (2005).

[12] Tryggestad, E., Aumann, T., Baumann, T., Bazin, D., Beene, J. R., Blumenfeld, Y., Brown, B. A., Chartier, M., Halbert, M. L., Heckman, P., Liang, J. F., Radford, D. C., Shapira, D., Thoennessen, M., and Varner, R. L. *Physics Letters B* **541**(1-2), 52 – 58 (2002).

[13] A. Bohr, B. R. Mottelson. *Nuclear Structure*, volume 1. W. A. Benjamin, New York, (1969).

[14] C. Cohen-Tannoudji, B. Diu and F. Laloë. *Mécanique quantique*. Hermann, Paris, (2000).

[15] Bass, R. *Nuclear Reactions with Heavy Ions*. Springer Verlag, Berlin, Heidelberg, (1980).

[16] Hussein, M. S., Lichtenthäler, R., Nunes, F. M., and Thompson, I. J. *Physics Letters B* **640**(3), 91 – 95 (2006).

[17] A. Bohr, B. R. Mottelson. *Nuclear Structure*, volume 2. W. A. Benjamin, Reading, Massachusetts, (1975).

[18] Bothe, W. and Gentner, W. *Zeitschrift für Physik* **71**, 236–248 (1937).

[19] Migdal, A. *J. Phys. (USSR)* **8** (1944).

[20] G. F. Bertsch and R. A. Broglia. *Oscillations in Finite Quantum Systems*. Cambridge Monographs on Mathematical Physics, Cambridge, (1994).

[21] Berman, B. L. and Fultz, S. C. *Rev. Mod. Phys.* **47**(3) (1975).

[22] Auerbach, N. and Yeverechyahu, A. *Annals of Physics* **95**(1), 35 – 52 (1975).

[23] Bush, B. and Alhassid, Y. *Nuclear Physics A* **531**(1), 27 – 38 (1991).

[24] Junghans, A. R., Rusev, G., Schwengner, R., Wagner, A., and Grosse, E. *Phys. Lett. B* **670**(3), 200–204 DEC 18 (2008).

[25] Möller, P., Bengtsson, R., Carlsson, B. G., Olivius, P., Ichikawa, T., Sagawa, H., and Iwamoto, A. *Atomic Data and Nuclear Data Tables* **94**(5), 758 – 780 (2008).

[26] Möller, P., Nix, J. R., Myers, W. D., and Swiatecki, W. J. *Atomic Data and Nuclear Data Tables* **59**(2), 185 – 381 (1995).

[27] Myers, W. D., Swiatecki, W. J., Kodama, T., El-Jaick, L. J., and Hilf, E. R. *Phys. Rev. C* **15**(6), 2032–2043 Jun (1977).

[28] Hill, D. L. and Wheeler, J. A. *Phys. Rev.* **89**(5), 1102–1145 Mar (1953).

[29] G. Musiol, J. Ranft, R. Reif and D. Seeliger. *Kern- und Elementarteilchenphysik*. Verlag Harri Deutsch, Frankfurt am Main, (1995).

[30] Weisskopf, V. *Phys. Rev.* **52**(4), 295–303 Aug (1937).

[31] Le Couteur, K. J. and Lang, D. W. *Nuclear Physics* **13**(1), 32 – 52 (1959).

[32] Liang, J., Cao, L.-G., and Ma, Z.-Y. *Physical Review C (Nuclear Physics)* **75**(5), 054320 (2007).

[33] Goriely, S. *Physics Letters B* **436**(1-2), 10 – 18 (1998).

[34] Rauscher, T. *Physical Review C (Nuclear Physics)* **78**(3), 032801 (2008).

[35] Kneissl, U., Pietralla, N., and Zilges, A. *Journal of Physics G: Nuclear and Particle Physics* **32**(8), R217–R252 (2006).

[36] Jackson, J. D. *Classical Electrodynamics*. John Wiley & Sons Inc., 3^{rd} edition, (1999).

[37] Benesh, C. J., Cook, B. C., and Vary, J. P. *Phys. Rev. C* **40**(3), 1198–1206 Sep (1989).

[38] Fermi, E. *Nuovo Cimento* **2**, 143–158 (1925). arXiv:hep-th/0205086v1.

[39] Bertulani, C. A. and Baur, G. *Nuclear Physics A* **458**(4), 725 – 744 (1986).

[40] Bertulani, C. A. and Baur, G. *Nuclear Physics A* **442**(3), 739 – 752 (1985).

[41] Bertulani, C. A. and Ponomarev, V. Y. *Physics Reports* **321**(4-5), 139 – 251 (1999).

[42] Aleixo, A. N. F. and Bertulani, C. A. *Nuclear Physics A* **505**(2), 448 – 470 (1989).

[43] Winther, A. and Alder, K. *Nuclear Physics A* **319**(3), 518 – 532 (1979).

[44] Llope, W. J. and Braun-Munzinger, P. *Phys. Rev. C* **41**(6), 2644–2653 Jun (1990).

[45] http://www-inj.gsi.de. Accessed: 27.11.2009.

[46] Geissel, H., Armbruster, P., Behr, K. H., Brünle, A., Burkard, K., Chen, M., Folger, H., Franczak, B., Keller, H., Klepper, O., Langenbeck, B., Nickel, F., Pfeng, E., Pfützner, M., Roeckl, E., Rykaczewski, K., Schall, I., Schardt, D., Scheidenberger, C., Schmidt, K. H., Schröter, A., Schwab, T., Sümmerer, K., Weber, M., Münzenberg, G., Brohm, T., Clerc, H. G., Fauerbach, M., Gaimard, J. J., Grewe, A., Hanelt, E., Knödler, B., Steiner, M., Voss, B., Weckenmann, J., Ziegler, C., Magel, A., Wollnik, H., Dufour, J. P., Fujita, Y., Vieira, D. J., and Sherrill, B. *Nuclear Instruments and Methods in Physics Research Section B: Beam Interactions with Materials and Atoms* **70**(1-4), 286 – 297 (1992).

[47] Geissel, H., Münzenberg, G., and Riisager, K. *Annual Review of Nuclear and Particle Science* **45**(1), 163–203 (1995).

[48] Münzenberg, G. *Nuclear Instruments and Methods in Physics Research Section B: Beam Interactions with Materials and Atoms* **70**(1-4), 265 – 275 (1992).

[49] Paschalis, S. *Relativistic One-Nucleon Removal Reactions.* PhD thesis, University of Liverpool, UK, (2008).

[50] http://www-land.gsi.de/a_new_land/__public/documentation/detectors/csi/tlange_mirror/CsI/csi.html. Accessed: 27.11.2009.

[51] Blaich, T., Elze, T. W., Emling, H., Freiesleben, H., Grimm, K., Henning, W., Holzmann, R., Ickert, G., Keller, J. G., Klingler, H., Kneissl, W., König, R., Kulessa, R., Kratz, J. V., Lambrecht, D., Lange, J. S., Leifels, Y., Lubkiewicz, E., Proft, M., Prokopowicz, W., Schütter, C., Schmidt, R., Spies, H., Stelzer, K., Stroth, J., Walus, W., Wajda, E., Wollersheim, H. J., Zinser, M., and Zude, E. *Nuclear Instruments and Methods in Physics Research Section A: Accelerators, Spectrometers, Detectors and Associated Equipment* **314**(1), 136 – 154 (1992).

[52] Cub, J., Stengel, G., Grünschloß, A., Boretzky, K., Aumann, T., Dostal, W., Eberlein, B., Elze, T. W., Emling, H., Ickert, G., Holeczek, J., Holzmann, R., Kratz, J. V., Kulessa, R., Leifels, Y., Simon, H., Stelzer, K., Stroth, J., Surowiec, A., and Wajda, E. *Nuclear Instruments and Methods in Physics Research Section A: Accelerators, Spectrometers, Detectors and Associated Equipment* **402**(1), 67 – 74 (1998).

[53] Mahata, K., Johansson, H. T., Paschalis, S., Simon, H., and Aumann, T. *Nuclear Instruments and Methods in Physics Research Section A: Accelerators, Spectrometers, Detectors and Associated Equipment* **608**(2), 331 – 335 (2009).

[54] Gutbrod, H. H., Augustin, I., Eickhoff, H., Gross, K.-D., Henning, W. F., Krämer, D., and Walter, G. *FAIR Baseline Technical Report*, (2006).

[55] http://www.gsi.de/forschung/kp/kp2/collaborations/R3B/R3B-TP-Dec05.pdf. Accessed: 27.11.2009.

[56] Santonico, R. and Cardarelli, R. *Nuclear Instruments and Methods in Physics Research* **187**(2-3), 377 – 380 (1981).

[57] Parkhomchuck, V. V., Pestov, Y. N., and Petrovykh, N. V. *Nuclear Instruments and Methods* **93**(2), 269 – 270 (1971).

[58] Knoll, G. F. *Radiation Detection and Measurement*. John Wiley & Sons Inc., 3^{rd} edition, (2000).

[59] Battistoni, G., Campana, P., Chiarella, V., Denni, U., Iarocci, E., and Nicoletti, G. *Nuclear Instruments and Methods in Physics Research* **202**(3), 459 – 464 (1982).

[60] Schöpf, H. and Schnizer, B. *Nuclear Instruments and Methods in Physics Research Section A: Accelerators, Spectrometers, Detectors and Associated Equipment* **323**(1-2), 338 – 344 (1992).

[61] Crotty, I., Lamas Valverde, J., Laurenti, G., Williams, M. C. S., and Zichichi, A. *Nuclear Instruments and Methods in Physics Research Section A: Accelerators, Spectrometers, Detectors and Associated Equipment* **337**(2-3), 370 – 381 (1994).

[62] Cardarelli, R., Di Ciaccio, A., and Santonico, R. *Nuclear Instruments and Methods in Physics Research Section A: Accelerators, Spectrometers, Detectors and Associated Equipment* **333**(2-3), 399 – 403 (1993).

[63] Abbrescia, M., Colaleo, A., Iaselli, G., Maggi, M., Marangelli, B., Natali, S., Nuzzo, S., Ranieri, A., Romano, F., Gianini, G., Ratti, S. P., and Vitulo, P. *Nuclear Instruments and Methods in Physics Research Section A: Accelerators, Spectrometers, Detectors and Associated Equipment* **398**(2-3), 173 – 179 (1997).

[64] Fonte, P., Smirnitski, A., and Williams, M. C. S. *Nuclear Instruments and Methods in Physics Research Section A: Accelerators, Spectrometers, Detectors and Associated Equipment* **443**(1), 201 – 204 (2000).

[65] Akindinov, A. V., Alici, A., Anselmo, F., Antonioli, P., Basile, M., Cara Romeo, G., Cifarelli, L., Cindolo, F., Cosenza, F., D'Antone, I., De Caro, A., De Pasquale, S., Di Bartolomeo, A., Fusco Girard, M., Golovine, V., Guerzoni, M., Guida, M., Hatzifotiadou, D., Kaidalov, A. B., Kim, D. H., Kim, D. W., Kisselev, S. M., Laurenti, G., Lioublev, E., Lee, K., Lee, S. C., Luvisetto, M. L., Margotti, A., Martemiyanov,

A. N., Massera, F., Meneghini, S., Michinelli, R., Nania, R., Otiougova, P., Pancaldi, G., Pesci, A., Pilastrini, R., Pinazza, O., Polozov, P. A., Rizzi, M., Scapparone, E., Scioli, G., Sellitto, S. B., Semeria, F., Serra, S., Smirnitski, A. V., Tchoumakov, M. M., Ugolini, E., Usenko, E., Valenti, G., Voloshin, K. G., Williams, M. C. S., Zagreev, B. V., Zampolli, C., Zichichi, A., Zucchini, A., and Zuffa, M. *Nuclear Instruments and Methods in Physics Research Section A: Accelerators, Spectrometers, Detectors and Associated Equipment* **533**(1-2), 93 – 97 (2004). Proceedings of the Seventh International Workshop on Resistive Plate Chambers and Related Detectors.

[66] Camarri, P., Cardarelli, R., Di Ciaccio, A., and Santonico, R. *Nuclear Instruments and Methods in Physics Research Section A: Accelerators, Spectrometers, Detectors and Associated Equipment* **414**(2-3), 317 – 324 (1998).

[67] Schüttauf, A. *Nuclear Instruments and Methods in Physics Research Section A: Accelerators, Spectrometers, Detectors and Associated Equipment* **533**(1-2), 65 – 68 (2004). Proceedings of the Seventh International Workshop on Resistive Plate Chambers and Related Detectors.

[68] Schüttauf, A., Hildenbrand, K. D., Ciobanu, M., Cordier, E., Herrmann, N., Kim, Y. J., Kis, M., Koczon, P., Leifels, Y., Petrovici, M., and Simion, V. *Nuclear Physics B - Proceedings Supplements* **158**, 52 – 55 (2006). Proceedings of the 8th International Workshop on Resistive Plate Chambers and Related Detectors.

[69] Alvarez-Pol, H., Alves, R., Blanco, A., Carolino, N., Eschke, J., Ferreira-Marques, R., Fonte, P., Garzón, J. A., Díaz, D. G., Pereira, A., Pietraszko, J., Pinhão, J., Policarpo, A., and Stroth, J. *Nuclear Instruments and Methods in Physics Research Section A: Accelerators, Spectrometers, Detectors and Associated Equipment* **535**(1-2), 277 – 282 (2004). Proceedings of the 10th International Vienna Conference on Instrumentation.

[70] Johansson, H. T. Thesis for the degree of Licentiate of Engineering, Chalmers University of Technology, Göteborg, Sweden, (2006).

[71] http://www-linux.gsi.de/∼weick/atima/. Accessed: 27.11.2009.

[72] Livingood, J. J. *The Optics of Dipole Magnets*. Academic Press, (1969).

[73] Boretzky, K., Grünschloß, A., Ilievski, S., Adrich, P., Aumann, T., Bertulani, C. A., Cub, J., Dostal, W., Eberlein, B., Elze, T. W., Emling, H., Fallot, M., Holeczek, J., Holzmann, R., Kozhuharov, C., Kratz, J. V., Kulessa, R., Leifels, Y., Leistenschneider, A., Lubkiewicz, E., Mordechai, S., Ohtsuki, T., Reiter, P., Simon, H., Stelzer, K., Stroth, J., and Sümmerer, K. *Phys. Rev. C* **68**(2), 024317 Aug (2003).

[74] Boretzky, K. *Systematische Untersuchungen zur Coulombanregung der Zwei-Phononen-Dipolriesenresonanz in ^{208}Pb.* PhD thesis, Universität Frankfurt am Main, Germany, (1995).

[75] Rindler, W. *Introduction to Special Relativity.* Clarendon Press, Oxford, (1991).

[76] Leo, W. R. *Techniques for Nuclear and Particle Physics Experiments.* Springer Verlag, 2^{nd} edition, (1994).

[77] Firestone, R. B. Retrieved September 26, 2009, from http://ie.lbl.gov/toi.html.

[78] Fultz, S. C., Alvarez, R. A., Berman, B. L., and Meyer, P. *Phys. Rev. C* **10**(2), 608–619 Aug (1974).

[79] Broda, R., Fornal, B., Królas, W., Pawłat, T., Bazzacco, D., Lunardi, S., Rossi-Alvarez, C., Menegazzo, R., de Angelis, G., Bednarczyk, P., Rico, J., De Acuña, D., Daly, P. J., Mayer, R. H., Sferrazza, M., Grawe, H., Maier, K. H., and Schubart, R. *Phys. Rev. Lett.* **74**(6), 868–871 Feb (1995).

[80] Oros-Peusquens, A. M. and Mantica, P. F. *Nuclear Physics A* **669**(1-2), 81 – 100 (2000).

[81] Kanungo, R. *Physics Letters B* **649**(1), 31 – 34 (2007).

[82] Langanke, K., Terasaki, J., Nowacki, F., Dean, D. J., and Nazarewicz, W. *Phys. Rev. C* **67**(4), 044314 Apr (2003).

[83] Kelic, A., Ricciardi, M., and Schmidt, K.-H. *Proceedings of Joint ICTP-IAEA Advanced Workshop on Model Codes for Spallation Reactions, ICTP Trieste, Italy* 4-8 February (2008). arXiv:0906.4193v1.

[84] Gaimard, J.-J. and Schmidt, K.-H. *Nuclear Physics A* **531**(3-4), 709 – 745 (1991).

[85] Carlos, P., Beil, H., Bergere, R., Fagot, J., Lepretre, A., Veyssiere, A., and Solodukhov, G. V. *Nuclear Physics, Section A* **258**, 365 (1976).

[86] Raman, S., Nestor C. W. Jr., and Tikkanen, P. *Atomic Data and Nuclear Data Tables* **78**(1), 1 – 128 (2001).

[87] Sorlin, O., Leenhardt, S., Donzaud, C., Duprat, J., Azaiez, F., Nowacki, F., Grawe, H., Dombrádi, Z., Amorini, F., Astier, A., Baiborodin, D., Belleguic, M., Borcea, C., Bourgeois, C., Cullen, D. M., Dlouhy, Z., Dragulescu, E., Górska, M., Grévy, S., Guillemaud-Mueller, D., Hagemann, G., Herskind, B., Kiener, J., Lemmon, R., Lewitowicz, M., Lukyanov, S. M., and Mayet, P. *Phys. Rev. Lett.* **88**(9), 092501 Feb (2002).

[88] Rose, M. E. *Phys. Rev.* **76**(5), 678–681 Sep (1949).

[89] Bevington, P. R. and Robinson, D. K. *Data Reduction and Error Analysis for the Physical Sciences*. McGraw-Hill, New York, 3^{rd} edition, (2003).

[90] Adrich, P. *Observation of Pygmy and Giant Dipole Resonances in* ^{132}*Sn and neighboring mass isotopes*. PhD thesis, Jagiellonian University, Krakow, Poland, (2005).

[91] Klimkiewicz, A. *Systematic investigation of the dipole response in exotic neutron-rich isotopes in* ^{132}*Sn mass region*. PhD thesis, Jagiellonian University, Krakow, Poland, (2007).

[92] Monrozeau, C., Khan, E., Blumenfeld, Y., Demonchy, C. E., Mittig, W., Roussel-Chomaz, P., Beaumel, D., Caamano, M., Cortina-Gil, D., Ebran, J. P., Frascaria, N., Garg, U., Gelin, M., Gillibert, A., Gupta, D., Keeley, N., Maréchal, F., Obertelli, A., and Scarpaci, J.-A. *Physical Review Letters* **100**(4), 042501 (2008).

[93] Lui, Y.-W., Youngblood, D. H., Clark, H. L., Tokimoto, Y., and John, B. *Physical Review C (Nuclear Physics)* **73**(1), 014314 (2006).

[94] Nayak, B. K., Garg, U., Hedden, M., Koss, M., Li, T., Liu, Y., Madhusudhana Rao, P. V., Zhu, S., Itoh, M., Sakaguchi, H., Takeda, H., Uchida, M., Yasuda, Y., Yosoi, M., Fujimura, H., Fujiwara, M., Hara, K., Kawabata, T., Akimune, H., and Harakeh, M. N. *Physics Letters B* **637**(1-2), 43 – 47 (2006).

[95] Zhou, W., Seccombe, D. P., and Tuckett, R. P. *Physical Chemistry Chemical Physics* **4**(19), 4623–4633 (2002).

[96] United Nations Framework Convention on Climate Change. http://unfccc.int/resource/docs/tp/tp0403.pdf, (2004). Accessed: 27.11.2009.

[97] Christophorou, L. G. and Olthoff, J. K. *Journal of Physical and Chemical Reference Data* **29**(3), 267–330 (2000).